The fundamental role of spectral scattering in the ocean colour Phytoplankton Functional Type signal

Elisabeth (Lisl) Robertson Lain

Dissertation presented for the degree of
Doctor of Philosophy

Department of Oceanography
University of Cape Town
South Africa

September 2017

Dedication

For my parents, the Dr.s Robertson

*

"Because for whom do we do these things, if not for our parents?"

J.M. Coetzee (2003)

The fundamental role of spectral scattering in the ocean colour Phytoplankton Functional Type signal: A modelling study

Lisl Robertson Lain

Submitted for the degree of Doctor of Philosophy
September 2017

Abstract

There is increasing interdisciplinary interest in phytoplankton community dynamics as the growing environmental problems of water quality (particularly eutrophication) and climate change demand attention. This has led to a pressing need for improved biophysical and causal understanding of Phytoplankton Functional Type (PFT) optical signals, in order that satellite radiometry may be used to detect ecologically relevant phytoplankton assemblage changes. This understanding can best be achieved with biophysically and biogeochemically consistent phytoplankton Inherent Optical Property (IOP) models, as it is only via modelling that phytoplankton assemblage characteristics can be examined systematically in relation to the bulk optical water-leaving signal. Harmful Algal Bloom (HAB) conditions in the Southern Benguela and various inland waters of Southern Africa require continuous observation by satellite due to the potential for significant negative environmental impacts. Current oceanic bio-optical models do not perform well in elevated Chlorophyll *a* conditions, but the high biomass conditions of Southern African inland and coastal waters lend themselves extremely well to the development of phytoplankton IOP models as the water-leaving signal is overwhelmingly phytoplankton-dominated. An initial validation of a new model of Equivalent Algal Populations (EAP) is presented here, and comparison is made with two prominent phytoplankton IOP models. The EAP model places emphasis on explicit biophysical modelling of the phytoplankton population as a holistic determinant of IOPs. By necessity due to its origins in

highly scattering waters, a distinctive attribute of the EAP model is its comprehensive handling of the spectral and angular character of phytoplankton scattering. This emphasis is shown to have an impact on the ability to retrieve the detailed phytoplankton spectral scattering information necessary for PFT applications and to successfully simulate water-leaving reflectance across wide ranges of physical environments, biomass, and assemblage characteristics. The accurate description of a water body's Volume Scattering Function (VSF), and hence its phase functions, is critical to the determination of the constituent IOPs, the associated spectral water-leaving reflectance, and consequently the retrieval of PFT information. The EAP model offers the ability to provide phytoplankton population-specific phase functions, unveiling an opportunity to gain further insight into the causality of the PFT signal.

This is a new modelling capability, and its application in case studies and sensitivity analyses has resulted in improved understanding of the PFT/assemblage-related signal, in particular the discovery that phytoplankton spectral scattering is the primary driver of the PFT-related signal. The required thresholds of PFT detection with respect to biomass, IOP budget and assemblage effective diameter are quantified. Key findings are that the backscattering-driven signal in the 520 to 600 nm region is the critical PFT identifier at marginal biomass, and that while PFT information does appear at blue and red wavelengths, it is compromised by biomass/gelbstoff ambiguity in the blue and low signal in the red, due primarily to absorption by water. The key findings and recommendations are hoped to provide considerable insight into PFT approaches with regard to *in situ* observation, sensor development and algorithm optimisation for the next generation of PFT investigations.

Declaration

The work in this thesis is based on research carried out at the Department of Oceanography, University of Cape Town, and NRE at the CSIR, Rosebank. No part of this thesis has been submitted elsewhere for any other degree or qualification and it is all my own work unless referenced as otherwise in the text.

I confirm that I have been granted permission by the University of Cape Town's Doctoral Degrees Board to include the following publications in my PhD thesis, and where co-authorships are involved, my co-authors have agreed that I may include the publications:

Robertson Lain, L., Bernard, S., Evers-King, H. (2014). Biophysical modelling of phytoplankton communities from first principles using two-layered spheres: Equivalent Algal Populations model. *Optics Express* **22** (14) pp. 16745–16758

Robertson Lain, L., Bernard, S., Matthews, M. (2017). Understanding the contribution of phytoplankton phase functions to uncertainties in the water colour signal *Optics Express* **25** A151–A165

I hereby: (a) grant the University free license to reproduce the above thesis in whole or in part, for the purpose of research; (b) declare that: (i) the above thesis is my own unaided work, both in conception and execution, and that apart from the normal guidance of my supervisor, I have received no assistance apart from that stated below; (ii) except as stated below, neither the substance or any part of the thesis has been submitted in the past, or is being, or is to be submitted for a degree at this University or any other University. (iii) I am now presenting the thesis for examination for the Degree of PhD.

22 September 2017

Acknowledgements

The years taken to produce this work were not easy ones, and I gratefully acknowledge the support and encouragement of some extraordinary people.

I am profoundly grateful to my CSIR supervisor Dr. Stewart Bernard, upon whose own work on the EAP model this project is built. It has been a hugely enjoyable privilege to work alongside you. It is my most fervent hope to do you proud.

My thanks also to my UCT supervisor Prof. Chris Reason for his support particularly when difficult choices needed to be made. I deeply appreciate you encouraging me to prioritise myself and my family when I needed to.

Funding from the Centre for Scientific and Industrial Research (CSIR) and University of Cape Town (UCT) PhD Scholarship Programme is gratefully acknowledged, as is the support of the CSIR Strategic Research Programme. Thanks also to CSIR CHPC in Rosebank for the use of their facilities.

Specific thanks to Dr. Curtis Mobley for assistance with Hydrolight, my father Dr. GN Robertson for help with Fortran, Andy Rabagliati for his open source expertise, and Edward van Kuik for help with visualisations and JavaScript. Acknowledgement, too, to the anonymous reviewers of my published manuscripts for their valuable improvements.

I have been fantastically supported by my co-workers at both UCT and CSIR. Hayley, Sandy, Sarah, Tommy, Luke, Emma, Marie, Christo, William, Nicolette, Precious, Bjorn, Mark, Jeremy and Marjolaine - it is such a pleasure working with you all. I truly appreciate you being your brilliant, supportive and humourous selves.

On a personal note, grateful thanks to my entirely unflappable husband Nick Lain, who is so used to being last on my list of priorities that he perhaps mistakenly

believes he belongs there. Also to my quite extraordinary sisters because they don't, and do, care (in appropriate proportions); and to Melody Kanhanda, second mother to my children and someone who has shown me a thing or two about commitment and hard work.

Thanks also to my mother and mother-in-law for TLC lavished on the littles, particularly in the last few weeks of writing up. And deep gratitude to my many wonderfully supportive friends particularly Richard Keeton, who is well-versed in the language of existential crises, and Anice Lombard, for spending her precious free time helping me out, and who knows what to do when the world is caving in. The bottle says to take two and keep away from children, right?

Notation

Symbol	Definition	Units
EAP	Equivalent Algal Populations	
IOP	Inherent Optical Property	
AOP	Apparent Optical Property	
RT Model	Radiative Transfer Model	
CDOM	Coloured Dissolved Organic Matter (gelbstoff)	
PFT	Phytoplankton Functional Type	
VSF	Volume Scattering Function	
FF	Fournier Forand (phase function)	
c_i	Chlorophyll a density per cell volume	$\mathrm{kg.m^{-3}}$
$a_{gd}(\lambda)$	combined gelbstof and detrital absorption (used by EAP)	$\mathrm{m^{-1}}$
$b_{bnap}(\lambda)$	small particle backscattering (detrital and/or non-algal)	$\mathrm{m^{-1}}$
$R_{rs}(\lambda)$	Remote Sensing Reflectance	$\mathrm{sr^{-1}}$
$R_{rs}\phi$	Remote Sensing Reflectance due to phytoplankton	$\mathrm{sr^{-1}}$
$a_\phi(\lambda)$	phytoplankton absorption coefficient	$\mathrm{m^{-1}}$
$a(\lambda)$	total particulate absorption coefficient	$\mathrm{m^{-1}}$
$a_g(\lambda)$	gelbstoff absorption coefficient (used by Lee, 2006)	$\mathrm{m^{-1}}$
$b_{det}(\lambda)$	detrital (non-algal) scattering coefficient	$\mathrm{m^{-1}}$
$b_{b\phi}(\lambda)$	phytoplankton backscattering coefficient	$\mathrm{m^{-1}}$
$b(\lambda)$	total particulate scatter (phytoplankton and all non-algal)	$\mathrm{m^{-1}}$
$b_s(\lambda)$	small particle (non-algal) scattering coefficient	$\mathrm{m^{-1}}$
$a_{det}(\lambda)$	detrital (non-algal) absorption coefficient (used by Lee, 2006)	$\mathrm{m^{-1}}$
$b_\phi(\lambda)$	phytoplankton scattering coefficient	$\mathrm{m^{-1}}$
$c_\phi(\lambda)$	phytoplankton total attenuation coefficient	$\mathrm{m^{-1}}$
$a_g(\lambda)$	gelbstof absorption coefficient (used by Alvain, 2012)	$\mathrm{m^{-1}}$
$a *_\phi (\lambda)$	chlorophyll-specific absorption coefficient	$\mathrm{m^2\ mg^{-1}}$
ϕ	fluorescence quantum efficiency	dimensionless
ϕ_{sat}	fluorescence quantum efficiency from satellite	dimensionless

Contents

Chapter 1

Introduction

1.1 Motivation

Phytoplankton across the world's oceans represent about half of all primary production on our planet (Field et al., 1998; McClain, 2009). Their growth and function are fundamental to sustaining life: they constitute the foundation of the aquatic food web, and serve critical roles in the recycling of essential elements such as carbon and nitrogen, as well as in remineralisation (Swart et al., 2012; Thomalla et al., 2011; Ryan-Keogh et al., 2017). Being so dependent on nutrient availability and water temperature, these tiny organisms are key indicators of ecosystem change, and understanding their community dynamics is key to answering some of the most challenging earth science questions of our time.

The widespread distribution and integral role of phytoplankton in global systems means that these fields of study depend heavily on modelling together with satellite data for any largescale analysis. *In situ* data collection is indispensible for local scale investigations and for ground truthing of satellite and model data, but simultaneous large scale direct measurements are logistically impossible. Satellite sensors have enabled global scale studies for nearly 40 years, and continuously for 20. Broad scale biomass estimates based on Chlorophyll *a* concentrations derived from satellite radiometry are widely relied upon, but the extent and accuracy of information that can be derived from satellite imagery is still uncertain (Brewin et al., 2017; Antoine et al., 2008). Recently there has been considerable interest in more

detailed information on phytoplankton assemblage characteristics (Sathyendranath et al., 2004; Alvain et al., 2012; Kostadinov et al., 2009; Kostadinov, 2016), but it has not been widely ascertained to what degree so called Phytoplankton Functional Type (PFT) information can be gleaned from satellite data, and at what level of confidence. Descriptions of PFTs differ with context - and the potential for distinguishing their ecological roles from their optical signatures must be examined. As satellite technological capability advances and future missions are increasingly designed to address specific science questions, the importance of well-defined user needs regarding work on satellite-derived PFTs is greater than ever.

The causal effect of biophysical phytoplankton characteristics on the optical water-leaving signal is at the heart of all of these requirements. Any useable radiometric PFT signal results directly from the interaction of phytoplankton with their light environment, but the physical basis of this interaction is not well understood in terms of observed variability across the wide diversity of aquatic environments and phytoplankton assemblages (Anderson, 2005; Brown et al., 2008). Optical measurements in natural waters are challenging: they are expensive and logistically difficult, technically complex due to large dynamic ranges of the signal, and overall require delicate, rigorously calibrated instrumentation with precise knowledge of sources of error. Remote sensing and moored *in situ* instrumentation are the only feasible ways to acquire continuous data series, but these largely involve measurements of the bulk optics. Isolating the respective optical components for laboratory assessment is a significant further undertaking. *In situ* and laboratory measurements are consequently extremely valuable, and models such as the Equivalent Algal Populations (EAP) model provide essential tools for the analysis and understanding of these bulk measurements, whether above- or sub-surface.

The bulk Inherent Optical Properties (IOPs) of a water body are the combined optical characteristics of all optically active consistuents in the water, together with those of the medium itself. The Apparent Optical Properties (AOPs) are those resulting from these interactions, that is, the quantities that can be observed and measured from the water-leaving signal. To understand variability in the resulting AOPs, the IOPs of all the in-water constituents must be accommodated. A rigorous

IOP model such as the EAP can systematically vary phytoplankton biogeophysical attributes in the context of likely additional non-algal absorption and scatter, and, in combination with a Radiative Transfer (RT) model, can examine the resulting effects on the light field. A coupled IOP-RT model is an invaluable tool both in terms of understanding optical causality and also in quantifying the relative contributions of these attributes to the observable water colour signal. It is only via modelling that we can systematically investigate the effects of variability in biophysical parameters on the light field, across a wide range of water types and optical conditions.

The optical impact of a phytoplankton assemblage interacting with its aquatic environment is by no means straightforward. There is a bulk effect attributable simply to biomass, for which Chlorophyll *a* (Chl *a*) is used as a proxy [1], and which for the most part dominates the phytoplankton-related signal in Case 1 waters (Morel and Prieur, 1977). PFT characteristics generally result in second-order optical effects: accessory pigments dominate assemblage absorption characteristics (Hoepffner and Sathyendranath, 1991), and particle size is usually the primary determinant of scattering characteristics (Olson et al., 1989). Natural waters are also subject to non-algal (frequently referred to as Coloured Dissolved Organic Matter - CDOM, or gelbstoff) absorption, as well as non-algal scatter, which can include scatter by detrital matter, sediment, bacteria, and/or bubbles. These quantities absorb and scatter incident light in different spectral regions from phytoplankton, and their subsequent optical interactions and resulting effect on the bulk signal are highly complex. Understanding the interaction between cells' biophysical characteristics and the light field in the presence of these additional opticallly active consituents is central to determining which parts of the optical signal are useable for PFT diagnostics, and likewise, where signal ambiguity is prohibitive.

Ambiguities in retrievals of second-order optical characteristics via inversion al-

[1] It is acknowledged that Chl *a* concentration and biomass are not equivalent, as biomass includes non-pigmented biological matter in quantities which may not be proportional to pigmented matter. However, for the purposes of this study, biomass and Chl *a* concentration are used interchangeably, as this work is approached from a purely optical perspective and ignores non-pigmented biological matter.

gorithms from satellite data have been assessed elsewhere (Evers-King et al., 2014), but here the EAP is presented as a forward model, showcasing its strength as an investigative tool for furthering community understanding of causal phytoplankton optical relationships. It is used here in conjunction with Hydrolight-Ecolight radiative transfer software (Numerical Optics, Ltd.) to simulate interactions with the light field as expressed by the resulting remote sensing reflectance, R_{rs}. The overarching goal of this thesis is to use the EAP model to provide useful, quantifiable insight into the PFT question, to properly understand the variability observed in the water-leaving signal that is due to phytoplankton, and the uncertainties associated with that signal.

1.1.1 History and development of the EAP model

The development of the EAP model (Bernard et al., 2009) was driven by the requirement for a model capable of accurately handling very high phytoplankton biomass blooms in the Southern Benguela upwelling system, with the eventual aim of Harmful Algal Bloom detection, identification and monitoring with satellite data. The productive Benguela waters are considered 'extreme Case 1' where the optics are dominated by phytoplankton, with a strong biomass-related in-water signal distinct from the lesser contributions of Coloured Dissolved Organic Matter (CDOM, or gelbstoff) and non-algal consistuents e.g. detritrus, sediment, bacteria, and bubbles. Additionally, elevated biomass requires close attention to the spectral backscattering characteristics of phytoplankton (Whitmire et al., 2007, 2010; Vaillancourt, 2004) and so for the Benguela and other highly scattering high biomass environments, a model is required that addresses this explicitly.

From these needs arose the EAP model with its two-layered sphere particle and equivalent size-based community structure (Bernard et al., 2009) which enables the calculation of phytoplankton IOPs from first principles, presenting a valuable opportunity for furthering the understanding of causal relationships between phytoplankton physiology and their optical characteristics. Chapter 2 provides some explanation of the phytoplankton biophysical characteristics intrinsic to the model and how they are related to the resulting optics.

Phytoplankton-dominated waters with significant biomass are arguably the simplest environments in which to develop a phytoplankton IOP model, due to the overwhelming contribution of phytoplankton to the bulk optical signal. One of the advantages of working in high biomass waters - namely reduced species diversity (Bernard et al., 2007) - can be exploited to give good confidence in forward modelled phytoplankton IOPs, as Standard Normal particle size distributions with mid-range effective variance are found to be adequate to simulate phytoplankton assemblage IOPs in elevated biomass (Bernard et al., 2007). Additionally, because of the dominance of phytoplankton IOPs, the additional in-water consituents can be adequately modelled using generalised approximations (Bricaud et al., 1981; Roesler et al., 1989; Roesler and Perry, 1995). When it comes to much lower biomass waters where phytoplankton do not dominate the optics, uncertainty in the optical contribution of any of the consistuents is magnified as they are combined in more comparable proportions, and phytoplankton size distributions tend to be more variable. Models designed for lower biomass (see Chapter 2) tend to underperform in higher biomass conditions when phytoplankton IOPs dominate. It follows therefore, that the phytoplankton component of bulk water properties is not generally well represented in these models. Good information on the phytoplankton component is a prerequisite for any quantitative comment on the optical contribution of respective PFTs, or identifying changes in the bulk optical properties of seawater as dominant PFTs change. Only when representing the detailed nature of phytoplankton optics, with absorption and scattering biophysically consistent - as they are in nature - is a causal understanding of their interactive effect on the optical signal possible.

The aim of the EAP model is to understand the causality-driven impact of different phytoplankton assemblages on the water-leaving optical signal. Optical variability in phytoplankton is known to be driven by particle size (effective diameter D_{eff}) (Kostadinov et al., 2009; Bricaud et al., 2004), pigment quantity and type, cellular material, shape, and aggregation (Bricaud et al., 1988). The model focuses primarily on the D_{eff} parameter which is of fundamental importance both optically and ecologically (Kostadinov et al., 2009; Le Quéré et al., 2005). Following the EAP's conceptual intent to understand the impact of D_{eff} as the primary second-

order optical determinant, other sources of bio-optical variability are intentionally constrained. PFTs are therefore approached entirely from a size-based perspective, and the EAP model consequently lends itself extremely well to PFT sensitivity studies in terms of its ability to isolate small differences in reflectance resulting only from variability in assemblage size distribution (Evers-King et al., 2014). The model does additionally provide scope for varying other biophysical attributes within a population (such as the shape of the size distribution itself, the ratio of core to shell sphere volumes, and the cellular Chlorophyll *a* density of the cells in the distribution), as required.

The huge advantages of addressing phytoplankton assemblage optics in this way are countered somewhat by the reliance on the population effective diameter, which may not adequately reflect ecologically significant complexity within a given assemblage. Additionally, while the model is not intended as a full representation of phytoplankton optical complexities, there is certainly ecologically significant natural variability in phytoplankton IOPs e.g. dependent on their growth state (Moutier et al., 2017). Acknowledging these caveats is a reminder to emphasise that modelled phytoplankton characteristics should always be adequately contextualised to the appropriate ecological environment in order to be properly intepreted.

1.1.2 Handling second-order variability: core model attributes

At the core of the EAP model are the phytoplankton particle refractive indices, with the imaginary part of the refractive index approximately representing that portion of light which is absorbed by the cell, and the real part of the refractive index representing that portion of light which is scattered. The imaginary and real parts of the refractive index spectra are numerically linked through the Kramers-Kroning relations, and numerically linked to the specified intra-cellular Chl *a* concentration (Bernard et al., 2009). For each particle, a core sphere represents the cytoplasm (which contains approximately 80% water, and is almost colourless), while an outer sphere represents the chloroplast, where the pigmented material (generally Chl *a* in the largest part) is strongly absorbing. Refractive indices for the chloroplast spheres were derived from samples taken from actual Benguela blooms - dinoflagellate and

diatoms, as well as for a phycoerythrin-associated cryptophyte group (based on a *Mesodinium rubrum/ Myrionecta rubra* - dominated assemblage (Bernard et al., 2009).

A critical feature of the model is that a$^*\phi$ is constrained at 675 nm to reflect the theoretical maximum absorption by unpackaged phytoplankton of 0.027 mg.m^{-2} as per Johnsen et al. (1994). This is incorporated into calculation of the imaginary refractive index of the chloroplast layer n'_{chlor} (outer sphere), based on the assumption that the cytoplasm layer (inner sphere) has no signficant absorption at 675 nm:

$$n'_{chlor}(675) = \frac{675}{n_{media}} \frac{\pi c_i a^*_{sol}(675)}{4Vv} \tag{1.1.1}$$

where n$_{media}$ = 1.334 and Vv is the relative chloroplast volume, c_i is the intracellular Chl a, and $a^*_{sol}(675)$ is the Chl a-specific absorption at 675 nm of that pigment in solution, i.e. unpackaged (Bernard et al., 2009).

The effect of constraining the unpackaged absorption in this way is to establish a quantitative relationship between the intra-cellular Chl a and the cell volume; a relationship which is biophysically consistent as the cell size varies (Bernard et al., 2009). This results in an effectively decreasing Chl a-specific absorption with increasing size, observable in the resulting optics as the "package effect" (Bricaud et al., 1981).

The main light-harvesting pigments in typical diatom and dinoflagellate assemblages (fucoxanthin and peridinin respectively) - while chemotaxonomically distinct - display the typical broad, featureless absorption spectra characteristic of carotenoids, with peaks centered around 500 nm (Bricaud et al., 2004) and vary well within the natural variability of phytoplankton absorption. They consequently have similar refractive indices (Bernard et al., 2009) and so these types were combined into a generalised set of diatom/dinoflagellate set of IOPs, as no significant difference was found between the dinoflagellate and diatom groups in terms of their optics that could not be attributed to the respective particle sizes [see also (Dierssen et al., 2006), (Organelli et al., 2017)].

The model was later extended for application in eutrophic inland water systems, incorporating the optional representation of a vacuole, in order to simulate

cynaobacteria IOPs (Matthews and Bernard, 2013).

When coupled with a radiative transfer model - here, Hydrolight-Ecolight is used throughout - the interactions of phytoplankton IOPs (in combination with those of other in-water constituents) with the surrounding light field can be examined systematically. A full physics-based model such as this has the additional advantage of providing not only biophysically interrelated particle absorptions, scattering and backscattering, but IOPs for assemblages that are integrated over the entire assemblage size distribution, and which are fully angularly resolved. This presents the unique opportunity of closely examining simluated phytoplankton phase functions, which are notoriously difficult to measure, and whose behaviour in terms of variability in particle size and wavelength is poorly understood. With no decoupling of absorption and backscattering, and IOPs integrated over the entire size distribution, the model provides an unprecedented opportunity to examine the drivers of variability in phytoplankton optical signals systematically.

1.2 Thesis Objectives and Outline

The objectives of this thesis are as follows:

1. To validate the phytoplankton component of the EAP IOP model. This is done by detailed comparison with two other frequently used IOP models, those of Alvain et al. (2005) and Lee (2006). The most challenging part of the validation is in high biomass waters where the phytoplankton component of the model is required to be most accurate.

2. To test the sensitivity of the model with respect to the choice of approach to the modelling of the phase functions; to see when (i.e. under which water type conditions) phytoplankton-specific phase functions are required, and where the use of a Fournier Forand approximation is sufficient.

3. To apply the EAP model to a range of ecological scenarios to demonstrate its usefulness in terms of identifying and understanding the causal phytoplankton-driven contribution to the bulk optics.

4. To provide useful information on the magnitude and location of a size-driven

PFT signal in the R_{rs} to the design of future satellite missions with PFT retrieval as an identified science question e.g. PACE.

5. To understand the causal impact of the primary biophysical characteristics of phytoplankton assemblages on the associated optical signal.

The overarching goal of this thesis is to use the EAP model to provide useful, quantifiable insight into the PFT question, to properly understand the variability observed in the water-leaving signal that is due to phytoplankton, and the uncertainties associated with that signal.

In light of these objectives, this thesis presents, in Chapter 2, a validation of the EAP model in high biomass Benguela waters, previously published as Lain et al. (2014). This section outlines the model and draws attention to some of its specific features that distinguish it from other commonly used approaches. The sources of resulting differences in modelled R_{rs} from the IOP models of Lee (2006) and Alvain et al. (2012) are discussed, with particular reference to the handling of spectral backscatter. The spectral shift of prominent phytoplankton reflectance features in the blue and green towards the red as biomass increases is an important observation that relates to the increasing dominance of phytoplantkon backscatter to the bulk optics. The proportional contribution of phytoplankton to the bulk IOPs is discussed as a means of identifying under which conditions simple scattering models may no longer be adequate, and how these may be improved upon through the use of unique phytoplankton phase functions which are spectrally complex and vary with both phytoplankton backscatter fraction $b_{b\phi}$ and with wavelength λ.

This section concludes that the EAP model's explicit handling of phytoplankton spectral backscatter is what sets it apart in its ability to simulate high biomass reflectance, and that the incorporation of phytoplankton-appropriate phase functions is therefore central to the accurate simulation of reflectance where phytoplankton dominate the IOPs. As this is a component of radiative transfer modelling that is frequently approximated or even avoided altogether through the use of a shape factor (f/Q parameter), the EAP's handling of the phase functions is examined further in Chapter 3, previously published as Lain et al. (2017). This section shows that model

uncertainties (i.e. ambiguity due to phase function modelling choices) are significant even at moderate levels of phytoplankton scatter, and that these uncertainties contribute to ambiguity in the retrieval of assemblage effective diameter.

Chapter 4 discusses further the complexity of the bulk R_{rs} and examines the causal ambiguities inherent in the water-leaving signal with respect to the proportional contribution of phytoplankton to the total IOPs and resulting AOPs, as D_{eff} and biomass vary. The isolated phytoplankton component is then further examined for ambiguities in the frequently opposing optical effects of varying biomass and D_{eff}. Separating the effects of biomass and size is central to accessing PFT information, and this is discussed in terms of the sensitivity of different waveband ratios to these effects.

The Southern Ocean SANAE 55 cruise (Mtshali, 2016) is presented as the first case study, investigating under which observed ecological conditions an optical signal due to change in assemblage D_{eff} may be isolated from that due to a change in biomass, in the context of variability in the non-algal in-water constituents affecting the bulk optical signal. A second case study addresses assemblage shifts which additionally display pigment-driven variability: A Benguela-like *M. Rubrum* to dinoflagellate experiment examines pigment variability without a change in D_{eff}, whereafter the onset of the spring bloom in the Southern Ocean is simulated in an example combining both size and pigment effects.

The size-driven case studies are then generalised to theoretical studies of idealised low and high biomass environments, with estimated associated changes in assemblage effective diameter representing a typical oceanic bloom and a coastal diatom to dinoflagellate succession respectively. These examples pursue the question of PFT signal sensitivity and identify systematically where the size signal may be found, its spectral sensitivity, and where it may be sufficiently unaffected by variability in the non-algal optical components to be useful for PFT identification. The importance of the phytoplankton backscattering signal between 520 and 570 nm is uncovered, and this is causally examined.

Finally, some of the uncertainties around both measured and modelled R_{rs} are discussed, with reference to ambiguity in the signal contributed by all of the various

in-water constituents.

The thesis findings and conclusions are summarised in Chapter 5.

Chapter 2

Validation of the Equivalent Algal Populations model

This chapter is published as:
Robertson Lain, L., Bernard, S., Evers-King, H. (2014). Biophysical modelling of phytoplankton communities from first principles using two-layered spheres: Equivalent Algal Populations model. *Optics Express* **22** (14) pp. 16745–16758

Please note: This chapter refers to the generalised eukaryote IOPs as "dinoflagellate/diatom IOPs", however they should be more correctly referred to as "generalised Chl *a*-carotenoid eukaryote IOPs". The text below remains as it was published.

2.1 Introduction

Eutrophication is a leading cause of impairment of aquatic ecosystems worldwide, and is accelerating in rate and extent due in large part to human activities (Chislock et al., 2013). Toxic algae, tainted freshwater supplies and fisheries-threatening hypoxia can all result in health risks and substantial economic losses. The need for improved water quality monitoring in vulnerable coastal regions and of inland freshwater resources is best addressed by a combined approach: increased monitoring of biogeophysical variables in these environments (both *in situ* and by remote sensing), coupled with the development of reliable bio-optical models in pursuit of

better understanding of the biophysical relationships at play.

Existing optical modelling approaches (Alvain et al., 2012; Lee, 2006; Carder et al., 1991; Fischer and Fell, 1999) employ simple IOP models generally most suited to open-ocean (oligo- or meso-trophic) conditions and usually heavily dependent on Chlorophyll *a* (Chl *a*) specificity. Such models also typically decouple the phytoplankton absorption and backscattering terms, or use backscattering terms related only to the gross particulate: an approach that has served well in relatively low biomass oceanic waters, but is fundamentally restrictive for the analysis of the phytoplankton-specific ocean colour signal. This work has been undertaken, in part, to assess the suitability of a more holistic phytoplankton optical modelling approach for eutrophic environments, and ultimately to provide an enhanced capacity to analyse the ocean colour signal content related to the variability of phytoplankton functional types.

This EAP model represents a departure from existing modelling approaches in that it is population driven in terms of phytoplankton functional type (PFT). In other words, phytoplankton IOPs are formulated from population-specific refractive indices and so are not independent of each other. It has been established that at elevated biomass the spectral character of phytoplankton scattering becomes increasingly important (Vaillancourt, 2004; Whitmire et al., 2007). Implementation of the EAP model allows investigation into when the resulting AOPs (including remote sensing reflectance, R_{rs}) may be sensitive to this variability, through the use of spectrally variant phase functions in the radiative transfer component of the model. Also, size- and assemblage-related influences are not well parameterised in the literature (Bernard et al., 2009), and the EAP model additionally allows for investigation into these effects.

The very productive southern Benguela lends itself well to the development of optical modelling and validation activities. Inner shelf waters are typically dominated by 3 phytoplankton groups: potentially bloom-forming diatom and dinoflagellate assemblages, and nanophytes (small-celled assemblages, including some chlorophytes). These groups have distinctive optical characteristics and in any given natural assemblage there may be optically important components of all of them. For simplicity,

modelling of only the dinoflagellate group is discussed here, as representative of frequently occurring high biomass blooms.

2.1.1 Phytoplankton component

Assemblages are modelled using equivalent size distributions and a two-layered sphere cell geometry (Bernard et al., 2007, 2009), comprising a core sphere (representing the cytoplasm) and a shell sphere (chloroplast). Phytoplankton IOPs are generated from the real and imaginary parts of the cell refractive indices (Bernard et al., 2009). Where detailed refractive index data are not known at longer wavelengths (> 750 nm) and imaginary refractive indices are assumed to be very small, they are linearly interpolated from their values at 720 nm to $1\text{x}10^{-5}$ at 750 nm, and then to $1\text{x}10^{-9}$ at 900 nm, with subsequent quantified effect on the real part of the refractive index using established methods (Bernard et al., 2009). (This allows consistency between the RIs of different PFTs at long wavelengths).

The relative chloroplast volume is maintained at 20% while the effective diameter of the cell varies. The effective diameter of the modelled distribution is thus central to the IOP model, with the resulting IOPs depending heavily on particle size. The modelled IOPs have a constant Chl *a* density per cell (c_i), set at 2.5 kg.m^{-3} which was chosen as representative from the literature (Bernard et al., 2009). Recent experiments however indicate that covarying c_i with effective diameter may be more appropriate as the Chl *a* density of specific species becomes more important with the bloom's monospecificity. However, this approach is not pursued further here.

For the forward modelling of example populations, a Standard normal particle size distribution (from 1 to 100 μm at 1 μm resolution) with effective variance of 0.6 is used as a reasonable approximation to the reduced species diversity typical of blooms of elevated biomass (Bernard et al., 2007).

2.1.2 Other components

The primary intention here is to examine the modelled phytoplankton biomass and assemblage effects on ocean colour, so very simplistic scaling of other constituents

is employed to demonstrate relative model performance.

A simple exponential combined gelbstoff and detrital absorption term $a_{gd}(\lambda)$ (Bricaud et al., 1981; Roesler et al., 1989) is used as representative of commonly occurring conditions in the Benguela:

$$a_{gd}(\lambda) = a_{gd}(400)\exp[-S(\lambda - 400)] \tag{2.1.1}$$

The exponential slope factor S is given a constant value of 0.012 (Bernard et al., 1998).

An observed relationship of

$$a_{gd}(400) = 0.0904\log[Chl_a] + 0.1287 \tag{2.1.2}$$

from measurements in the Benguela is used to scale the gelbstof/detrital exponential term, and $a_{gd}(750)$ onwards is assumed to be zero.

Non-algal backscattering is modelled after Roesler and Perry (Roesler and Perry, 1995) who describe a small particle backscattering term (b_{bs}) represented by a power law relationship ($b_{bs} = \lambda^{-1.2}$) with a constant spectral shape dependent only on wavelength but variable in magnitude. In the EAP model b_{bs} is described as b_{bnap} to emphasise that this term incudes all non-algal scattering sources. Non-algal scatter b_{nap} is approximated as 50 times the b_{bnap}. This yields a non-algal particulate backscattering probability ($\tilde{b}_{bnap}$) of 0.02 (2%). This is assumed to be reasonable given that it has been shown that the total particulate backscattering probability $\tilde{b}_b$ varies in the range 1.2 to 3.2 % in coastal waters dominated by non-algal particles (i.e. Case 2) (Chami et al., 2006b), and that generally accepted values for $\tilde{b}_b$ in Case 1 waters is around 1% (Twardowski et al., 2001). Keeping the non-phytoplankton backscattering constant with Chl *a* results in a dependent but non-linear relationship, resulting in an overall $\tilde{b}_b$ that decreases as Chl *a* increases, while maintaining its significant optical contribution and increasing spectral variability as eutrophication occurs.

Ecolight radiative transfer software (Sequoia Scientific, 2008) was used to generate R_{rs} from these IOPs (given total absorption, attenuation and backscattering

data), using wavelength-specific Fournier Forand phase functions as $\tilde{b}_b$ varies across the wavelength spectrum. Fluorescence quantum efficiency ϕ was approximated as follows by Chl *a* concentration: below 10 mg.m^{-3} = 1%, 10-50 mg.m^{-3} = 0.6%, 50-100 mg.m^{-3} = 0.2% and over 100 mg.m^{-3} = 0.1%.These values are based on MODIS ϕ_{sat} climatologies (Behrenfeld et al., 2009), and measurements (Ostrowska et al., 2012) to characterise the reduction in ϕ as eutrophication increases. An annual average for solar irradiance and a solar zenith of 30 degrees was used in lieu of time and location.

2.2 A comparison of IOP models

EAP simulated R_{rs} were compared to a subset of those from models described by Alvain *et al.* (Alvain et al., 2012) and Lee *et al.* (Lee, 2006), two prominent phytoplankton IOP models both well validated for their applications, designed for Chl *a* concentrations ranging from 0.02 - 3 mg.m^{-3} (Alvain et al., 2012) and 0.03 - 30 mg.m^{-3} (Lee, 2006). The IOP approaches of both models are abbreviated in Table 2.1.

The models of both Alvain and Lee use Chl *a* specific absorption spectra $a^*_\phi(\lambda)$ as described by Bricaud (Bricaud et al., 1988). The approaches taken to gelbstof absorption are similar to the EAP model. The Alvain model neglects a separate detrital absorption term (representing all non-algal particles) on the basis that the spectral shape is similar to that of $a_{gd}(\lambda)$ and that absorption by non-algal particles represents just 10% of gelbstoff absorption (as determined by Siegel *et al.*, 2002, in (Alvain et al., 2012)). Neither model includes a fluorescence term.

A significant difference between these two approaches is the determination of the backscatter. The Alvain model uses a spectrally invariant Petzold phase function for the total particulate backscatter $\tilde{b}_b$. This results in a constant total backscatter fraction of 0.0189. The Lee model separates the backscatter into its two components, calculating $b_{b\phi}$ from b_ϕ with a 1% Fournier Forand phase function, and b_{bdet} from b_{bdet} with a Petzold phase function.

Both models have included dynamic ranges of IOP values in order to account

for the variability observed in natural waters. For clarity when making the comparison to the EAP model, IOP values were selected from within these dynamic ranges which most closely approximate those of the EAP model. For the $a_g(\lambda)$ and $a_{gd}(\lambda)$ contributions this selection was based on the EAP value of $a_{gd}(400)$. Likewise, a constant detrital scattering function approximating that of the EAP was selected from the ranges offered by the Lee and Alvain models. This ensures that the comparison between models is made under consistent (i.e. Benguela-like) water type conditions. Furthermore, the Alvain and Lee models were constrained for the purposes of this comparison to use the same Chl *a* specific phytoplankton absorption spectra (Bricaud et al., 1988). A subset of phytoplankton scattering functions was selected by comparing the coefficients at 550 nm to those of the EAP model.

While these constraints inevitably reduce the range of resulting R_{rs} values, these subsets should be acceptable for the purpose of commenting primarily on the different approaches to modelling the backscattering and the significance of these approaches as phytoplankton biomass increases to eutrophic concentrations.

The Alvain IOPs were processed to R_{rs} using Ecolight's two component model for Chl *a* concentrations of 1, 2, 5, 10, 15 and 30 mg.m^{-3} , using total a and b and a Petzold phase function for all particulate matter. This results in a total particulate backscatter fraction of up to 1.9% which is considered too high for Chl *a* concentrations over about 1 mg.m^{-3} (Morel and Maritorena, 2001).

The Lee IOPs were also processed to R_{rs} using Ecolight's two component model for Chl *a* concentrations of 1, 2, 5, 10, 15 and 30 mg.m^{-3} using the total absorption and scattering coefficients. A combined backscattering phase function was calculated for each wavelength using the 1% Fournier Forand phase function to retrieve the $b_{b\phi}$ from the b_ϕ, and the Petzold to retrieve the b_{bdet} from the b_{det}. The sum of these, i.e. the total b_b, was then used as input for Ecolight's wavelength-specific variable $\tilde{b}_b$ Fournier Forand phase function selection option.

Table 2.1: IOP parameterisations of the models of Alvain (Alvain et al., 2012) and Lee (Lee, 2006)

IOP	Alvain (2012)	Lee (2006)
$a_\phi(\lambda)$	$a *_\phi (\lambda)[Chl_a]^{[E]}$	$a *_\phi (\lambda)[Chl_a]^{[E]}$
$a_g(\lambda)$	$0.065[Chl_a]^{0.75}exp(-0.014(\lambda - 443))$	$a_g(440)exp(-S_g(\lambda - 440))$
$a_{det}(\lambda)$	neglected	$a_{det}(440)exp(-S_{dm}(\lambda - 440))$
$a_{gd}(\lambda)$	$a_g(\lambda)$	$a_g(\lambda) + a_{det}(\lambda)$
$b_\phi(\lambda)$		$c_\phi(\lambda) = c_\phi(550)(550/\lambda)^{n1}$ where $c_\phi(550) = p3 * [Chl_a]^{0.57}$ then $b_\phi(\lambda) = c_\phi(\lambda) - a_\phi(\lambda)$ (see (Lee, 2006) for $n1$ and $p3$ values)
$b_{det}(\lambda)$		$b_{det}(\lambda) = b_{det}(550) * (550/\lambda)^{n2}$ where $b_{det}(550) = p4 * [Chl_a]^{0.766}$ (see (Lee, 2006) for $n2$ and $p4$ values)
$b_{tot}(\lambda)$	$0.3 * [Chl_a]^{0.62}(\lambda/660)^{-y}$ where $y = -0.55\log[Chl_a] + 1.6$	$b_{det}(\lambda) + b_\phi(\lambda)$
$bb_\phi(\lambda)$		determined by 1% Fournier Forand $\tilde{\beta}$ i.e. $\tilde{b}_{bphy}$ is 0.01
$bb_{det}(\lambda)$		determined by Petzold $\tilde{\beta}$ i.e. $\tilde{b}_{bdet}$ is 0.0189
$bb_{tot}(\lambda)$	determined by Petzold $\tilde{\beta}$ i.e. $\tilde{b}_{bdet}$ is 0.0189	

2.3 Results and Discussion

2.3.1 Comparison of the constrained Alvain, Lee and EAP models

The R_{rs} generated are beyond the expected performance of the Alvain model (i.e. Chl a concentrations up to 3 mg.m^{-3}) and up to the very limit of the Lee model (up to 30 mg.m^{-3}) in order to examine the impacts of the different approaches to the backscattering terms as biomass increases. R_{rs} from the 3 models agree well for the Chl $a = 1$ and 2 mg.m^{-3} experiments (Fig. 2.1). Divergence is observed after Chl $a = 5$ mg.m^{-3}.

Most notable perhaps at first glance are the comparatively large differences in magnitude of R_{rs} between EAP Chl $a = 1$ and 2 mg.m^{-3} with respect to the other models'. It should be emphasised that the EAP model, in this its simplest implementation, describes a homogenous dinoflagellate population with an idealised size distribution. At these low phytoplankton concentrations, natural populations would likely be variable both in species and in particle size.

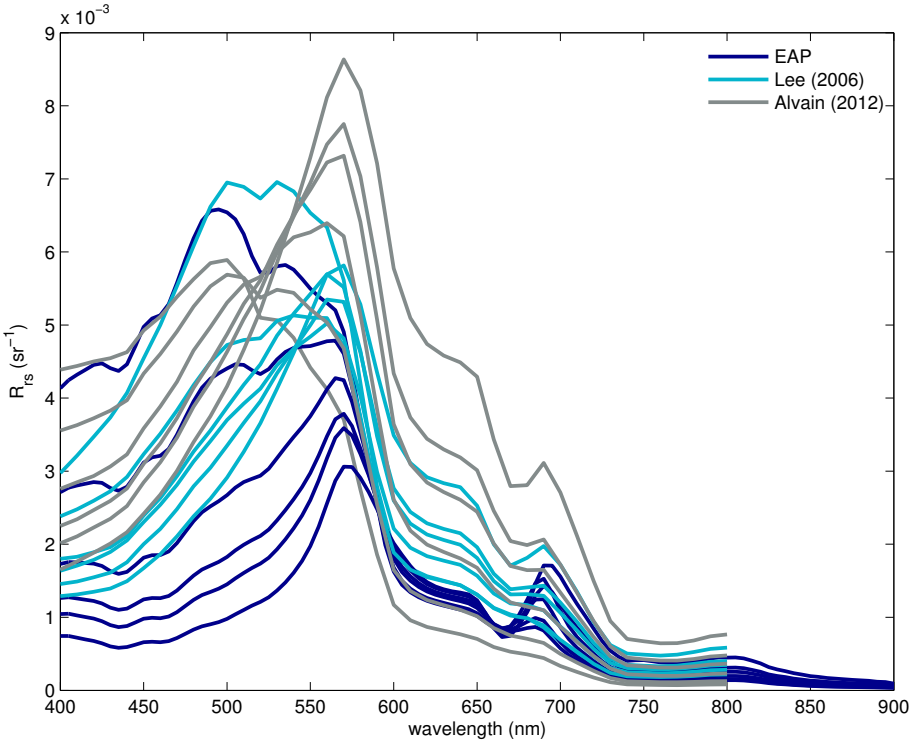

Figure 2.1: Comparison of Ecolight modelled R_{rs} from 3 IOP models: EAP, Alvain (Alvain et al., 2012) and Lee (Lee, 2006). Chl a values are 1, 2, 5, 10, 15 and 30 mg.m^{-3} in each case.

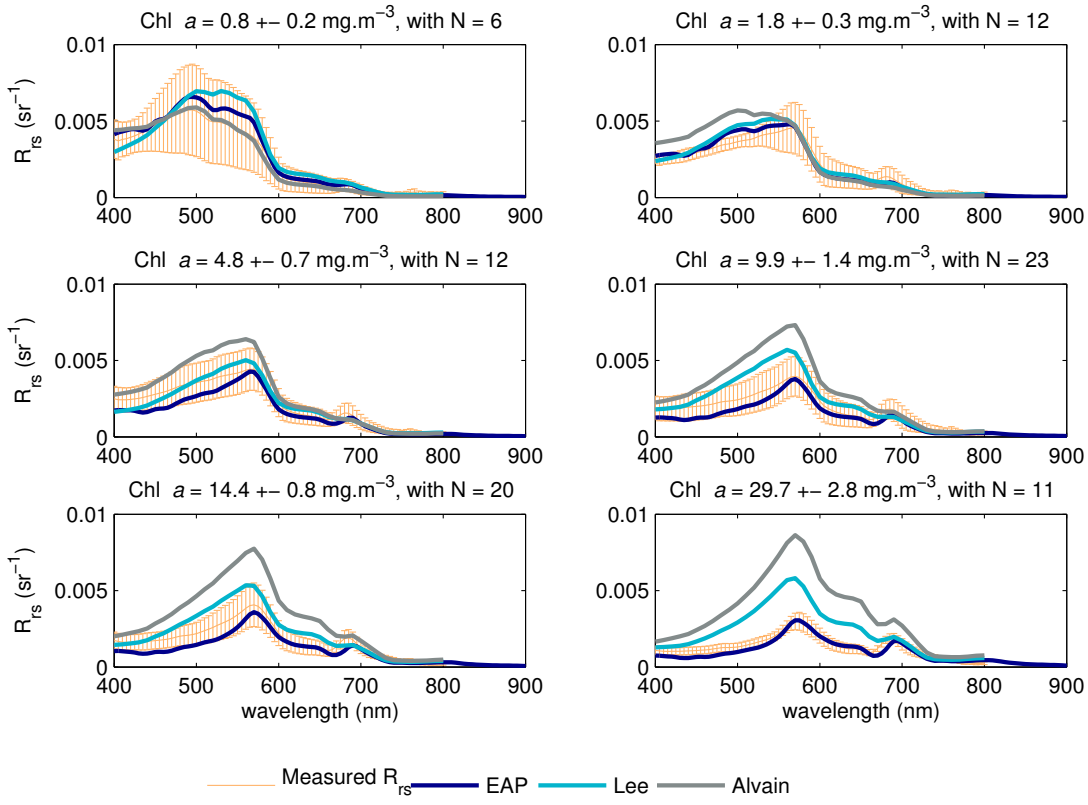

Figure 2.2: Preliminary validation of the 3 models with measured R_{rs}, for Chl a classes of 1, 2, 5, 10, 15 and 30 mg.m^{-3}. The mean measured spectrum in each class is presented with 1 standard deviation as an indication of natural variability. The mean measured Chl a for each set of measurements is presented at the top of each example with the standard deviation and the number of measurements, N.

2.3.2 Preliminary validation of R_{rs}

A preliminary validation exercise was carried out using measured Tethered Surface Radiometer Buoy (TSRB) data from 2002 - 2008 in the Benguela, processed to R_{rs} using ProSoft proprietary software (Satlantic). Measurements were selected for each chosen Chl *a* class, and the mean spectrum is presented using one standard deviation as an indication of variability in the optical measurements of natural populations (Fig. 2.2).

In the lower biomass classes (up to 5 mg.m^{-3}) the models all perform reasonably well considering the simplifications and constraints placed on them. As biomass increases past Chl *a* of 10 mg.m^{-3} however, the effect on the R_{rs} of the differences in the models' approaches to backscattering becomes evident. The notably reduced brightness of R_{rs} in the measurements is most accurately modelled using the EAP model's spectrally variant total backscattering probability which varies in magnitude with both Chl *a* concentration and wavelength.

It should be noted here that the use of the Bricaud a^*_ϕ by both Lee and Alvain implies a heavy dependence on size with increasing Chl *a* concentrations that make them unsuitable for use over very wide ranges of biomass. The Bricaud measurements were mostly performed in ocean basin areas with Chl *a* concentrations of around 0.05 to 8 mg.m^{-3} (Bricaud et al., 1995), with one sampling station going up to 24 mg.m^{-3} in the St. Lawrence estuary. These a^*_ϕ are appropriate for oligo/mesotrophic waters where a relationship of increasing cell size effects with increasing Chl *a* is generally observed. In highly eutrophic waters this relationship does not necessarily hold (Crichton et al., 2013). Figure 2.3 shows how the EAP model is forced to choose implausibly large sizes at high Chl *a* concentrations to maintain consistency with the Bricaud absorption spectra. The absorption profiles modelled above fit EAP size classes with effective diameters of between 6 and 16 μm, which were chosen according to observed dominant phytoplankton species' effective diameters rather than Bricaud-equivalent spectra (which would force the EAP model to go up to a D_{eff} of 45 μm at Chl *a* of 30 mg.m^{-3}, representing an unusually large cell).

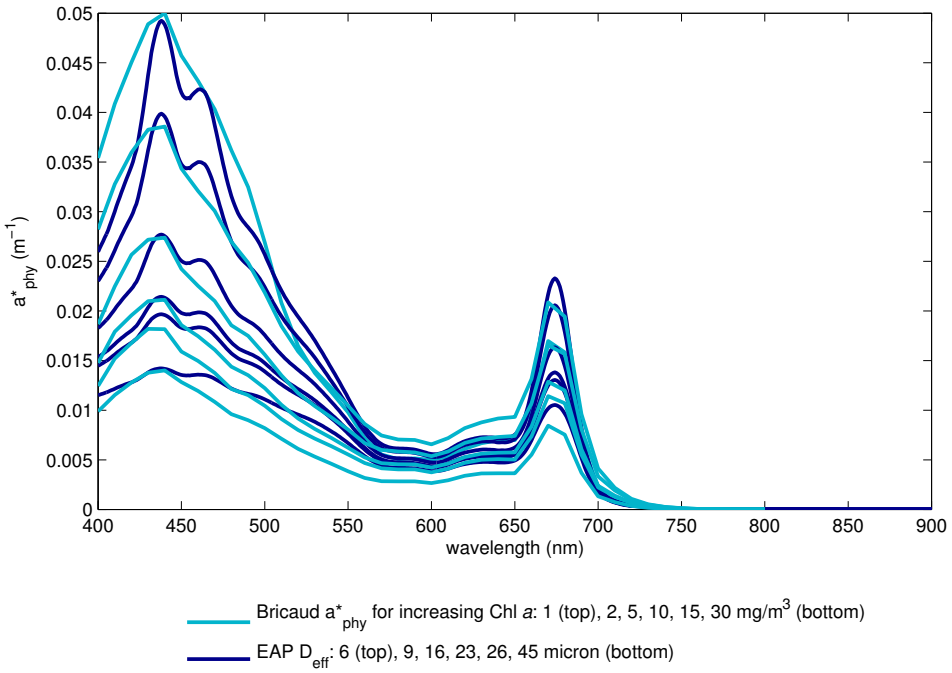

Figure 2.3: Bricaud a^*_ϕ for Chl $a = 1$, 2, 5, 10, 15 and 30 mg.m^{-3} matched to EAP a^*_ϕ by effective diameter (D_{eff}), implying EAP assemblage D_{eff} of 6, 9, 16, 23, 26 and 45 μm respectively.

2.3.3 Employing equivalent total absorption coefficients

To account for the differences in absorption, avoid the problem of an inherent dependency on large sizes at very high biomass, and in order to be able to comment more fully on the backscattering which is central to the EAP model and performing accurate IOP modelling in eutrophic waters, the comparative models were re-created, all using the EAP phytoplankton absorption spectra for each Chl a class. Also, the EAP fluorescence term was neglected to match the other models. The Lee model's detrital absorption term $a_{det}(\lambda)$ was also neglected as it is not explicitly included in the other models, and as Lee $a_g(\lambda)$ values were selected for this comparison to most closely match the EAP combined $a_{gd}(\lambda)$, that term can be considered to include detrital absorption.

Immediately noticeable in the resulting R_{rs} (Fig. 2.4) is the well constrained 600 to 650 nm region in the EAP model with respect to the Alvain model.

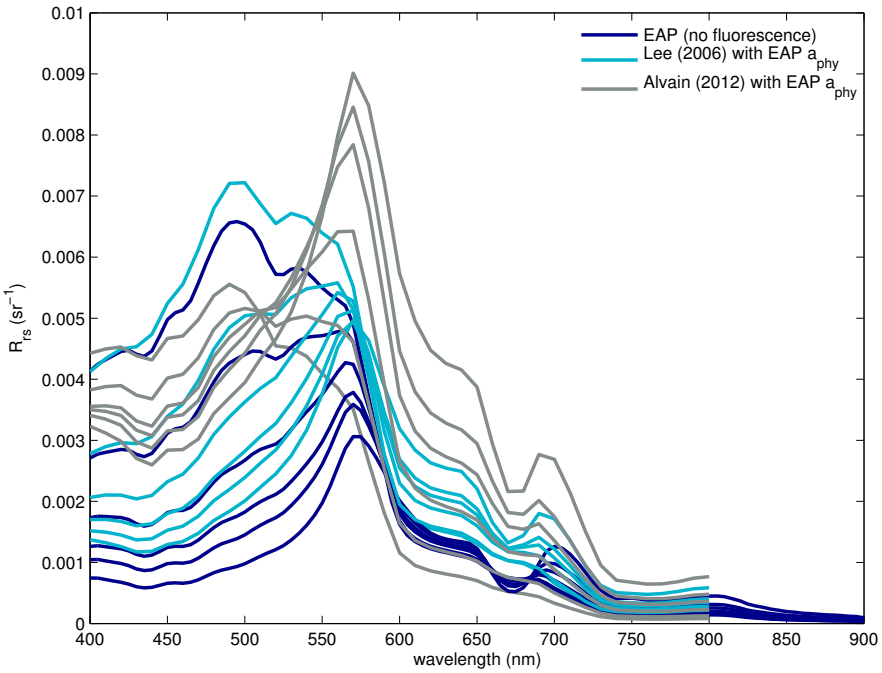

Figure 2.4: Comparison of Ecolight modelled R_{rs} from the 3 IOP models: EAP, Alvain (Alvain et al., 2012) and Lee (Lee, 2006). Chl a values are 1, 2, 5, 10, 15 and 30 mg.m^{-3} in each case. This comparison uses identical (EAP) a^*_ϕs in order to examine the effect of the different approaches to phytoplankton backscattering.

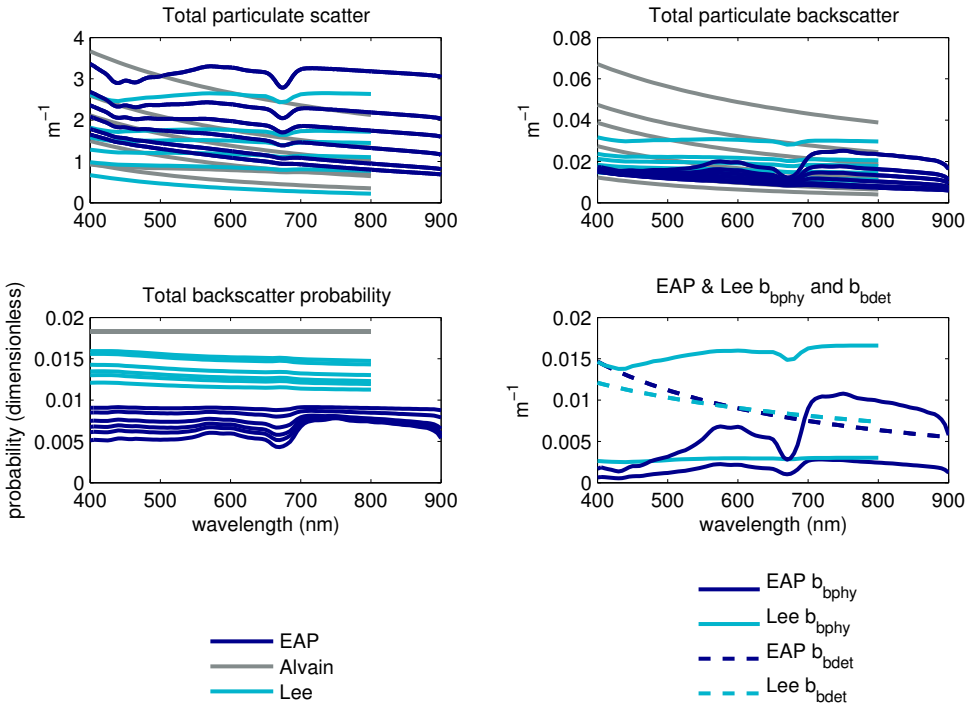

Figure 2.5: Scattering and backscattering characteristics of EAP, Alvain (Alvain et al., 2012) and Lee (Lee, 2006) at Chl *a* concentrations 1, 2, 5, 10, 15 and 30 mg.m^{-3}. Phytoplankton and detrital backscatter (bottom right) are shown for Chl *a* of 1 (lower line) and 30 mg.m^{-3} (upper line). The increased spectral detail of the EAP model's phytoplankton scatter and backscatter becomes increasingly important with increasing biomass as is evident in the spectral variation in the resulting total backscattering probability (bottom left).

The Alvain model's total scattering compares well with EAP $b(\lambda)$ in magnitude (Fig. 2.5, top left) but the choice of one spectrally invariant phase function for both phytoplankton and non-algal particles (Petzold) results in an unrealistically high backscatter fraction which is constant over varying biomass (Fig. 2.5, bottom left). In turn this results in greatly magnified backscattering at high Chl *a* concentrations.

The spectrally less variant total particulate scatter of the Lee model, and choice of spectrally flat phase functions (Fournier Forand 1% and Petzold) for both the phytoplankton and non-algal components results in total backscattering profiles with more or less indistinct spectral features, although the average magnitudes compare well to EAP in the mid biomass classes. The increased spectral variability of EAP backscattering is translated into the R_{rs} as a shift of the 680 nm peak towards 709 as biomass increases - a phenomenom also caused by the increase in the red Chl *a* absorption band and the rapidly increasing water absorption with increasing wavelength. This is an important observed feature at the "red edge" of eutrophic water reflectances (Dierssen et al., 2006).

Modelling backscattering as flattened spectra with reduced spectral variability may enable adequate R_{rs} modelling at low biomass but as Chl *a* concentration and the importance of non-algal scattering increases, such simple b_b models are unable to reproduce the spectral shape and magnitude variations in the R_{rs} successfully. The EAP model reflects an approach to backscatter derived from phytoplankton community optics rather than a calculation based on attenuation and/or the assumption of spectrally invariant particle scattering characteristics.

2.3.4 Characterising eutrophic water R_{rs}

Having shown the validity of the EAP model R_{rs} with respect to measurements made in the Benguela, the model can now be used to examine the characteristics of much more eutrophic water conditions. Figure 2.6 shows Ecolight modelled R_{rs} using IOPs generated using the EAP model, for biomass increasing from 1 to 200 mg.m^{-3}. A Standard normal particle size distribution from 1 to 100 μm with effective diameter 16 μm is used here, representing a homogenous assemblage displaying the typical optical characteristics of a dinoflagellate population. This simulation

(again using Ecolight) includes contributions from the combined gelbstoff/detrital absorption term $a_{gd}(\lambda)$ and small particle backscattering $b_{bnap}(\lambda)$ as described earlier, and uses a choice of Fournier Forand phase function with a variable $\tilde{b}_b$ at each output wavelength.

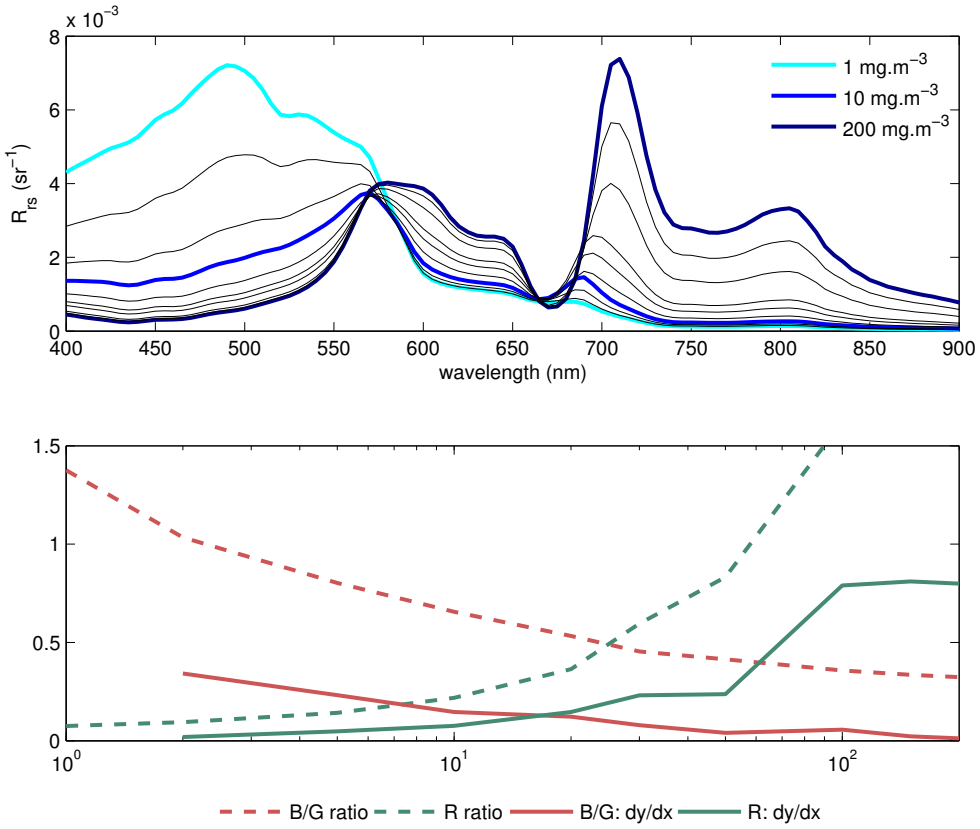

Figure 2.6: Modelled EAP R_{rs} (above) for typical dinoflagellate assemblage with effective diameter of 16 μm. Chl *a* concentrations are 1, 2, 5, 10, 20, 30, 50, 100, 150, 200 mg.m^{-3}. Below the shift from maximum peak reflectance height in the blue/green to the red is shown (dotted lines), for increasing Chl *a*. The first derivatives of these slopes (solid lines) cross at a Chl *a* of around 15 mg.m^{-3}, the point at which the red features of high biomass reflectance spectra start to dominate.

As biomass increases, the modelled R_{rs} show most distinctly a shift in the fluorescence peak at around 680 nm (in low biomass) towards 710 nm at Chl *a* concentrations of above 100 mg.m^{-3}. This is caused by the combined effects of a decrease in the fluorescence quantum efficiency (Dierssen et al., 2006) and increased phytoplankton absorption as this region becomes the dominant identifier of high concentrations of Chl *a*. Water is also strongly absorbing in this region which magnifies this effect. The switch in dominance of the 443:555 to the 709:555 band ratio (Fig. 2.6, as

per the SeaWiFs OC4 Chl *a* retrieval algorithm (O'Reilly et al., 1998)) shows the importance of signal in the red for Chl *a* estimation in waters with concentrations over about 25 mg.m^{-3}.

Other notable features of R_{rs} with increasing eutrophication are convergence at around 660 nm, as well as around 560 nm, and the well constrained region between these points. The decrease in R_{rs} in the blue is indicative of decreased influence of gelbstoff absorption with respect to Chl *a* absorption as the latter becomes more dominant spectrally.

2.3.5 EAP R_{rs} validation at very high biomass

Some very high biomass TSRB measured R_{rs} are presented here. The measurements (N=4, 6 and 5 respectively) represent a range of assemblage types and size distributions, which the EAP forward modelled R_{rs} do not consider here. This brief validation exercise shows that a chosen effective diameter of 12 μm most accurately matches all three high biomass blooms (for Chl *a* of 110, 150 and 180 mg.m^{-3} respectively). Most of the R_{rs} measurements were from a *Prorocentrum triestinum*-dominated bloom in 2005, with varying lesser proportions of *Dinophysis acuminata*, *D. fortii* and *P. reticulatum* (Fawcett et al., 2007). *P. triestinum* is a small dinoflagellate approximately 18-22 μm in length and 6-11 μm in width. The variability in resulting R_{rs} from size effects is clearly seen.

As biomass increases, the need for the employment of wavelength-dependent phase functions for at very least the phytoplankton component is evident. Figure 2.7 (bottom right) shows the increasingly variable values of the backscatter fraction as Chl *a* increases (for consistent assemblage D_{eff} and phytoplankton type). These range from an essentially spectrally constant backscatter fraction at low Chl *a* (1 mg.m^{-3}) to variability across the wavelength spectrum from 0.002 (i.e. 0.2%) to 0.006 (i.e. 0.6%) in eutrophic water conditions.

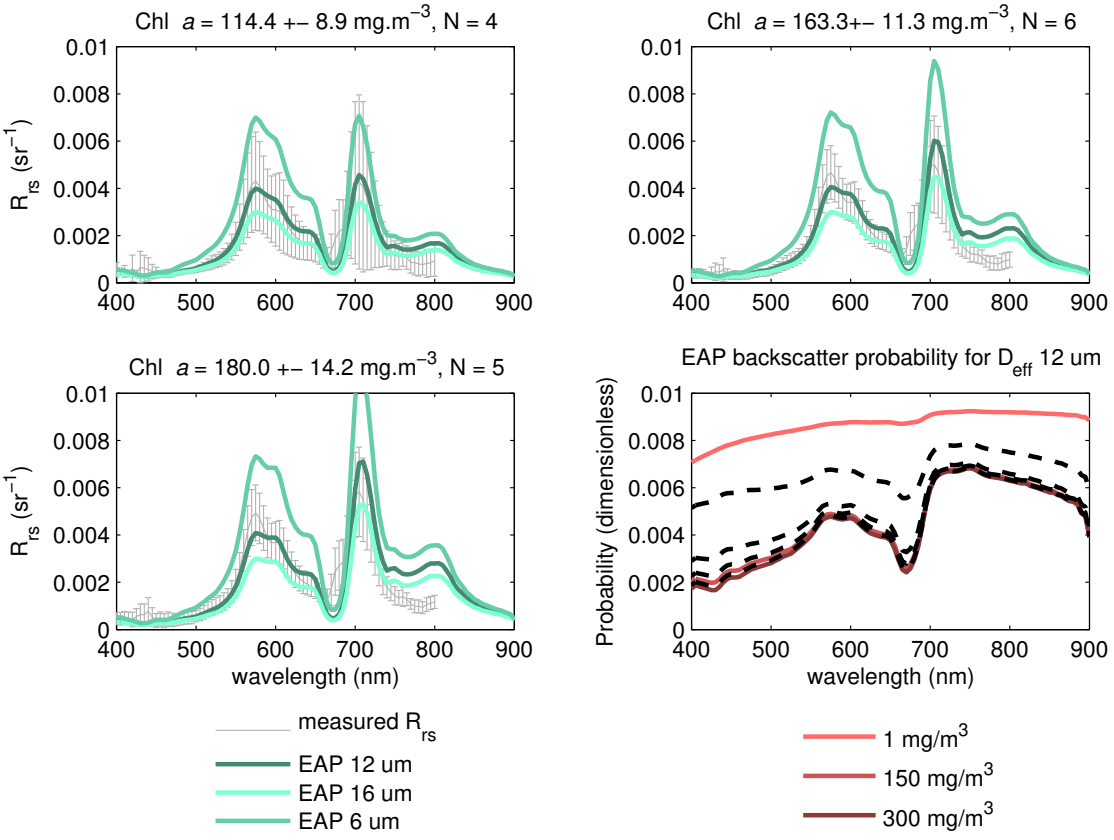

Figure 2.7: High Biomass Validation of EAP R_{rs}, with EAP total backscatter probability shown for Chl a 1, 10, 50, 100, 150, 200 and 300 mg.m^{-3}.

2.3.6 Proportional contribution of phytoplankton to total R_{rs}

From EAP modelled data, the proportional (percentage) contributions of Chl *a* to the total absorption, total scatter and backscatter are shown in Fig. 2.8 for Chl a = 2 mg.m^{-3} and 150 mg.m^{-3}, keeping the effective diameter constant at 16 μm (representing a dinoflagellate assemblage). It can be concluded that at lower biomass, gelbstoff and detrital/small particles are optically significant, while at high biomass the signal is almost exclusively due to phytoplankton pigment. That being said, however, the relative contribution of detritus and small particles to backscatter remains important even at Chl *a* of 150 mg.m^{-3} and this is translated into the R_{rs} signal especially between 550 and 680 nm.

[Note: These proportions include absorption and scatter of the medium itself (water). Phytoplankton $R_{rs}\phi$ is calculated with only water + phytoplankton specific IOPs. Other contributions are total R_{rs} - $R_{rs}\phi$. Any optical interactions between phytoplankton and other components are therefore neglected here.]

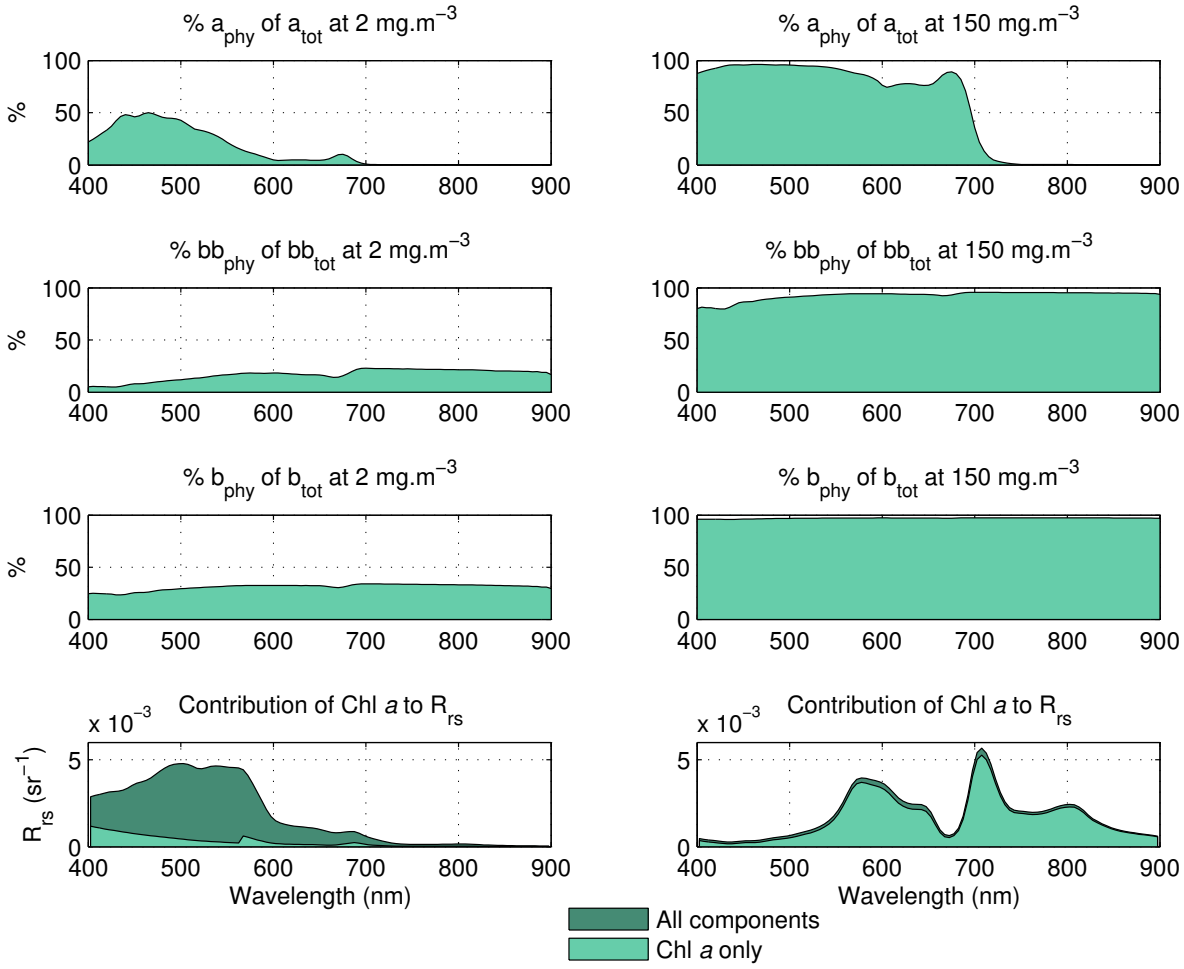

Figure 2.8: Contribution of Phytoplankton to total IOPs and R_{rs} signal, for Chl a values of 2 and 150 mg.m^{-3}, for an idealised dinoflagellate assemblage with effective diameter of 16 μm.

2.4 Conclusion

The EAP model is shown to be appropriate for IOP and R_{rs} modelling in high biomass Case 1 waters. Here it is presented in its simplest, forward form but there is much scope for added complexity and sensitivity. The modelling of mixed assemblages (mixed phytoplankton types of varying c_i and pigment concentrations, and different population size distributions) can be replicated as required. Cells containing vacuoles and other anomalous scattering characteristics can be considered too. The importance of detailed spectral backscattering is emphasised here. A full investigation into the sensitivity of the model to the use of discretised phase functions is presented in Chapter 3 to determine the extent of reliance on the detailed spectral backscattering component.

Chapter 3

Understanding the role of the phase function

This chapter is based on the work published as:
Robertson Lain, L., Bernard, S., Matthews, M. (2017). Understanding the contribution of phytoplankton phase functions to uncertainties in the water colour signal *Optics Express* **25** A151–A165

Please note: This chapter refers to the generalised eukaryote IOPs as "dinoflagellate/diatom IOPs", however they should be more correctly referred to as "generalised Chl *a*-carotenoid eukaryote IOPs". The text below remains as it was published.

3.1 Introduction

The recent focus on Phytoplankton Functional Types (PFTs) in ocean colour applications and optical signals (Sathyendranath et al., 2014) has exposed the need to better understand the relative contributions of a water body's various optical properties to the water-leaving signal, and where IOP and radiative transfer approximations may be used appropriately. The scattering phase function is central to the radiative transfer calculation but frequently approximated due to the lack of quantitative knowledge about systematic variability, and also for ease of computation. The impact of choice of phase function in the radiative transfer calculation

has been found to be significant (Tuchow et al., 2016), and determining the errors associated with the use of approximated or estimated phase functions is crucial to obtaining closure between radiometric and IOP measurements (Lefering et al., 2016). Modelling has an important role to play in providing appropriate tools to do so, and hence in understanding and quantifying second order assemblage effects on water colour across a range of water types.

A water body's whole suite of total IOPs and the entire angular structure of the light field can be completely determined from just the absorption coefficient $a(\lambda)$ and the Volume Scattering Function (VSF) $\beta(\lambda)$ (Mobley et al., 2002) [1]. The variability in intensity of scattered light over all angles in a water body is therefore fundamental to the determination of all the other Inherent Optical Properties (IOPs). The VSF describes the angular variation of scattered light intensities (Freda and Piskozub, 2007); the integrated VSF therefore gives the total scattering coefficient $b(\lambda)$. Normalising the VSF to the scattering coefficient $b(\lambda)$, gives the scattering phase function $\tilde{\beta}(\lambda)$ (Freda and Piskozub, 2007). Precise knowledge of the VSF and hence $\tilde{\beta}(\lambda)$ is critical to the accurate description of radiative transfer in the aquatic environment. Spectral measurements of $\beta(\lambda)$ or $\tilde{\beta}(\lambda)$ are extremely challenging, and furthermore when transforming individual-angle VSF measurements into estimates of the phase functions, assumptions must be made about the spectral shape of angular particular scatter (i.e. the chi factor), which results in additional uncertainties (Tuchow et al., 2016; Lefering et al., 2016; McKee and Cunningham, 2005). Modelling-based analyses of the water-leaving signal are the only practical way in which to examine the impact of the inherent angular variability systematically.

For ease of use in radiative transfer models, three approaches to approximating phase functions are generally employed (Mobley et al., 2002). Firstly, a phase function can be derived from a measured VSF by integrating and normalising as described above (e.g. Petzold, 1972). As all the IOPs can be calculated from $\tilde{\beta}(\lambda)$ and the absorption coefficient $a(\lambda)$ (and it is known that IOPs are unique to varying water body types), it follows that even if $a(\lambda)$ is well known, the use of a phase

[1] Fluoresced light is not described by these terms however, and should certainly be addressed in natural waters.

function measured in another water body will likely result in considerable errors.

In the second approach, a simple functional form of the phase function (e.g. Henyey-Greenstein in (Mobley et al., 2002)) can be used, and is attractive due to its mathematical simplicity. However, these approximations do not adequately describe scattering at the small (close to 0°) and large (close to 180°) scattering angles (Mobley et al., 2002). The simple functional forms have also been shown to be particle- and water-type specific, and are not suitable for generalised use in the radiative transfer problem (Mobley et al., 2002). It is expected that due to biophysical differences observable in species ultrastructure and hence spectrally in absorption and backscattering, PFTs will display distinct optical behaviour under different water type conditions.

In the third instance, a particle modelling approach such as Mie or Aden-Kerker theory can be used to calculate the phase function numerically. This method requires information about the complex refractive index n and the size distribution parameter μ (Mobley et al., 2002), quantities which are not frequently exactly known. A commonly used example of such an approach is the Fournier Forand formulation (Fournier and Forand, 1994). The phase functions of the Equivalent Algal Populations (EAP) model (Lain et al., 2014) are presented here as representative of an alternative particle modelling approach: an assemblage-based simulation of phytoplankton IOPs accounting for differences in cell size and assemblage size distribution, dominant pigments, cell composition and ultrastructure (Bernard et al., 2009). With the ability to vary these parameters systematically, better understanding of the contribution of the consituent IOPs to the phase function form can be gained. While it is appreciated that increasingly complex non-spherical models may represent the scattering properties of particle populations more accurately, this simplified model adequately simulates the optical properties of phytoplankton while allowing a quantitative relationship with cellular Chlorophyll a and refractive indices.

When the EAP model is coupled to a radiative transfer model, the effects on reflectance of systematically varying the IOPs can be assessed. This study is primarily designed as a validation of the EAP two-layered phase functions, with the secondary aim of isolating the magnitude of the contribution of the phase function

to uncertainty in R_{rs} calculated numerically.

3.2 Methods

3.2.1 Modelling outline

The modelled assemblages for this study are a first order representation of two broad functional types: a generalised eukaryotic group (e.g. diatoms, dinoflagellates) made up of chloroplast-containing cells with pigment-related spectral characteristics (carotenoid, Chl *a*, Chl *c*) (Bernard et al., 2009), and a generalised prokaryotic group (e.g. cyanobacteria) comprising cells dominated by a vacuole (Matthews and Bernard, 2013). Phytoplankton IOPs are generated from the real and imaginary parts of the refractive index (Bernard et al., 2009) for each PFT. The populations are modelled with a Standard normal size distribution and other parameters consistent with those described in (Lain et al., 2014).

First, the EAP phytoplankton phase functions of these two generalised groups are presented here with their respective population effective diameter and phytoplankton backscatter fraction, at each wavelength. Eukaryote and prokaryote are distinguished in terms of their IOPs and their respective phase functions are compared with their corresponding Fournier Forand equivalents (chosen for the same backscatter fraction). Then, these phytoplankton IOPs are combined with non-algal particle scatter and gelbstof and detrital absorption in a 4-component Hydrolight 5.2 model to simulate naturally occuring water types, and an exercise in radiometric closure using modelled and measured reflectance data (Lain et al., 2014) is presented.

The modelled data are then explored further with a simulation of the contribution to reflectance due only to the phytoplankton component of each of the two PFT groups, as biomass increases. The study concludes with an analysis of the sensitivity of modelled R_{rs} to the choice of phase function and a discussion of the causal variability in the phase functions themselves.

As the EAP model is run primarily in conjunction with Hydrolight 5.2 to solve the radiative transfer equation, R_{rs} resulting from the use of the two-layered EAP phase functions (hereafter $\tilde{\beta}_{EAP}$) are compared with the most comprehensive Hydrolight

option of a backscatter fraction $\tilde{b}_b(\lambda)$-specific Mobley-parameterised Fournier Forand phase function (hereafter $\tilde{\beta}_{FF}$). A description of the derivation of each of these functions follows.

3.2.2 Fournier Forand parameterisation used in Hydrolight 5.2

Mobley et al. (2002) determined that the use of a parameterised $\tilde{\beta}_{FF}$ for known particulate $\tilde{b}_b$ can provide a satisfactory substitute for a measured $\tilde{\beta}$. The necessity of using a $\tilde{\beta}$ for the correct backscatter fraction is clearly emphasised, as is the significance of the shape of the phase function (especially at intermediate angles). This is important because there are theoretically an infinite number of functions for an individual $\tilde{b}_b$, and not all of them will be appropriate for marine particles.

A fully analytical particle modelling approach is most desirable in terms of accuracy for individual water types. It is likely the only way of systematically producing phase functions across a wide range of particle and water types, and examining the variability in the dependent IOPs. The Fournier-Forand approach (Fournier and Forand, 1994) is an approximate formulation of the computationally-intensive full Mie calculation, using a Jungian particle distribution, with each particle scattering according to the anomalous diffraction approximation of the exact Mie theory. This formulation still requires knowledge of the real refractive index n and the Junge size parameter μ (slope of the hyperbolic function). If this formulation is integrated (Freda and Piskozub, 2007), it results in a relationship between n, μ and particulate backscatter fraction $\tilde{b}_b$. Because the n and μ are infrequently known for individual samples, Mobley proposed a further parameterisation of this formulation in order that a phase function dependent only on a known particulate $\tilde{b}_b$ could be calculated (Mobley et al., 2002). That $\tilde{b}_b$ is combined with a simple linear relationship between n and μ, determined from the measured Petzold phase functions, to produce a $\tilde{b}_b$-specific $\tilde{\beta}_{FF}$.

It should be noted that the $\tilde{b}_b$ backscatter fraction parameter describes the probability of scattering into the backward direction during a single scattering process and does not consider the additional effects of multiple scattering. So the choice of a sin-

gle phase function according to this parameter is likely limiting in highly scattering waters, where multiple scattering has an increased optical influence. The Fournier Forand approach (with its origins in Mie modelling) describes angular scattering for homogenous, non-absorbing, spherical particles in populations with a Junge size distribution. This is rarely the case in natural waters, e.g. phytoplankton are strongly absorbing particles, and problems associated with simulating their optical properties in this way are described in Whitmire et al. (2010) and Zhou et al. (2012).

3.2.3 Calculation of EAP phase functions

The EAP model simulates the total IOPs of a chosen algal population as described by its overall effective diameter (representing a full size distribution (Bernard et al., 2007)) as well as its component PFTs: that is, characteristics of particle ultrastructure in terms of distinguishing diatom, dinoflagellate, cryptophyte etc. Particles are modelled as two-layered spheres, where both the real and imaginary parts of the spectral refractive indices of both core and shell spheres (Lain et al., 2014) are specified, together with the chlorophyll density of cells, proportion of core to shell sphere volume, and the optional representation of a vacuole (Matthews and Bernard, 2013). This approach allows for the mathematical derivation of the full set of wavelength-dependent, spectrally variable phase functions at 0.1° resolution. The full mathematical description is available in (Bernard et al., 2009).

$\tilde{\beta}_{EAP}$ are generated at 0° to 180° at 0.1° resolution from the individual $\beta(\theta)$ functions for discrete particle sizes as described in (Bernard et al., 2009) and then integrated across the whole size distribution:

$$\beta(\theta, \alpha_M, m) = (1/\pi)\frac{\int i(\theta, \alpha, m)\ F(\alpha)\ \mathrm{d}\alpha}{\int Q_b(\alpha, m)\ F(\alpha)\ \alpha^2\ \mathrm{d}\alpha} \tag{3.2.1}$$

In this equation, the pre-computed $\beta(\theta)$ functions for each discrete size (as functions of the intensity parameter i and scattering efficiency parameter Q_b) are weighted according to the selected size distribution, written as function F of α, the relative size i.e. the geometric size relative to the wavelength of the surrounding medium (water). α_M is the modal value corresponding to the maximum frequency

in the distribution and m is the relative index of refraction. Please refer to Equation 20 in (Morel and Bricaud, 1986) for further details on notation and derivation of these quantities.

The importance of the contribution of the spectral shape of backscatter to the R_{rs} in the EAP model was established in the previous chapter (published as (Lain et al., 2014)). It has been determined elsewhere that there is a relationship between the spectral shape of particulate backscatter $\tilde{b}_b$ and the shape of the phase function $\tilde{\beta}$, and that the shape of $\tilde{\beta}$ is important (Freda, 2012; Chami et al., 2006a; Boss and Pegau, 2001; McKee and Cunningham, 2005). Due to the highly spectrally variable nature of EAP particulate (especially phytoplankton) backscatter, it is expected that the simple phase function forms may not be adequate as biomass increases and therefore the contribution of phytoplankton to the bulk IOPs increases (Tuchow et al., 2016).

The EAP model provides an additional dimension of complexity with respect to the Fournier Forand method, as the resulting phase functions are independently related to both the $\tilde{b}_b$ (through the population effective diameter, D_{eff}) and wavelength λ, as well as to the PFT-related parameters. They are unconstrained in shape (i.e. angular distribution of scattering) as they are not inherently dependent on the assumption of a Jungian size distribution, which may not be appropriate in highly productive waters where reduced species diversity is generally observed with increasing biomass (Bernard et al., 2007). Mobley et al. (2002) acknowledge the need for λ-dependent phase functions as particulate $\tilde{b}_b$ varies with wavelength. However due to the parameterised Fournier Forand formulation which constrains the relationship between the size distribution parameter and the particle refractive index, the phase function used at different wavelengths but for the same $\tilde{b}_b$ will be identical. In the EAP model this is not the case.

3.3 Results

3.3.1 Comparing the Fournier Forand and EAP phase functions: eukaryote group

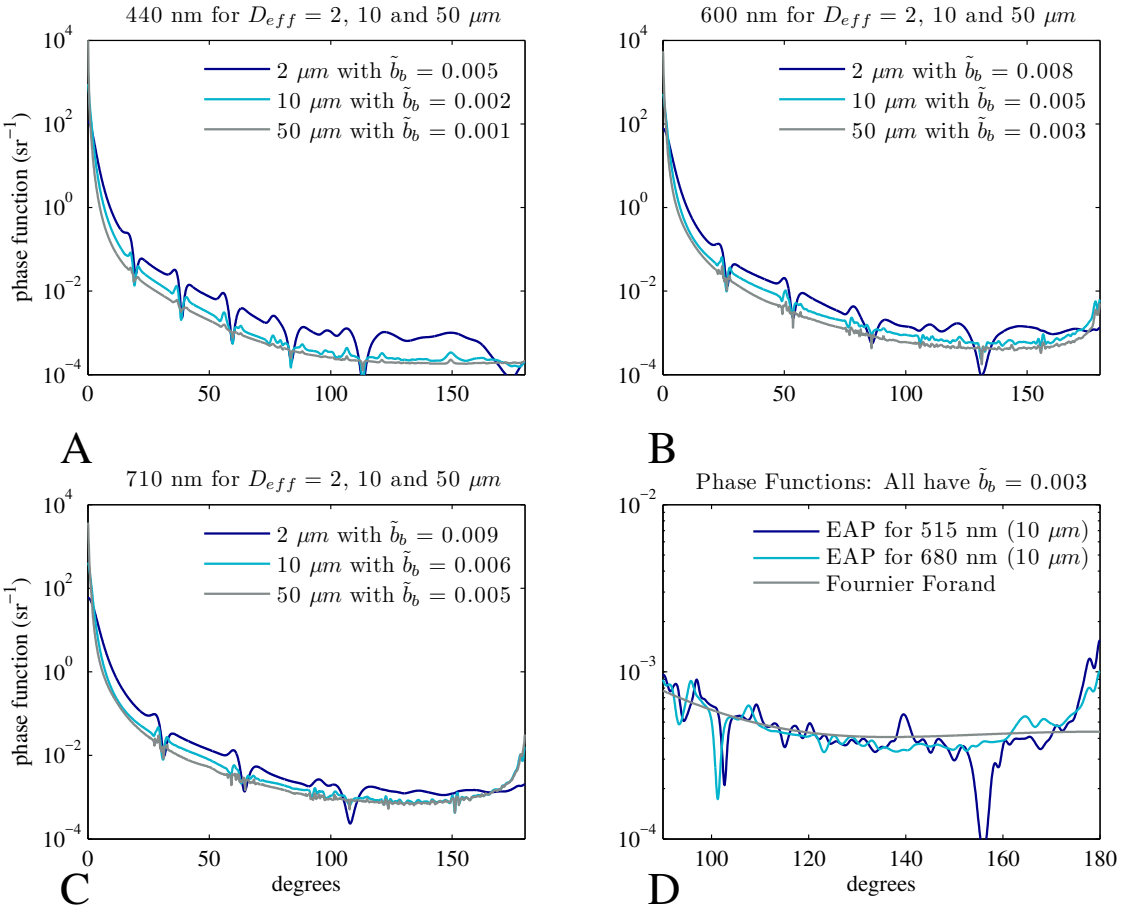

Figure 3.1: EAP phase functions for the phytoplankton component only of generalised eukaryote populations at selected λ, for three different D_{eff} 2, 10 and 50 μm, with corresponding phytoplankton backscatter fraction $\tilde{b}_{b\phi}$ (A-C). (D) illustrates the differences in EAP phase functions due only to wavelength, for constant $\tilde{b}_{b\phi}$, compared with a single corresponding Fournier Forand phase function which does not vary with wavelength.

In (Chami et al., 2006a), Chami et al. compared measured coastal VSFs and derived phase functions with their appropriate Fournier Forand counterparts chosen for their equivalent backscatter fractions. Following their findings of significant differences between both the actual structure of the phase functions themselves, and

between the respective resulting R_{rs}, this study presents a similar comparison. It should be emphasised that the Fournier Forand functions are intended for generalised use with the combined phytoplankton and non-algal particulate components of a water sample, whereas the EAP phase functions are phytoplankton specific, and applicable only when it is known that phytoplankton dominate the IOPs. For an example eukaryote population of mixed dinoflagellates, $\tilde{\beta}_{EAP}$ for selected wavelengths and D_{eff} are shown in Fig. 3.1, together with their corresponding $\tilde{b}_b$. They share the most notable features of $\tilde{\beta}$s derived from VSF measurements in coastal waters, described in (Chami et al., 2006a) as typical of natural waters. These features include strong forward peaks, minima at intermediary angles, and elevated levels of scattering towards reverse angles (160°-180°) (Chami et al., 2006a). This increase past 150° is also noted by Harmel et al. (2016) in measured VSFs of phytoplankton cultures at 515 nm, and Fig. 3.1(D) shows a comparable EAP phase function at 515 nm (sample population with D_{eff} 10 μm). It can additionally be observed that this elevation is not present in the $\tilde{\beta}_{EAP}$ at shorter wavelengths (e.g. 440 nm), where there are strong phytoplankton absorption features, and that there is some variability in the shape and magnitude of this feature at different wavelengths: at much smaller particle sizes (e.g. 2 μm), the opposite effect is observed at 440 nm. This is in some sense compensated for by the overall comparably greater magnitude of the $\tilde{\beta}$ at intermediate angles. This emphasizes the complexity of the relationships between $\tilde{b}_b$, D_{eff} and λ: the shape of $\tilde{\beta}_{EAP}$ changes with $\tilde{b}_b$ as well as D_{eff} and λ.

$\tilde{\beta}_{EAP}$ features compare well to Chami's measured $\tilde{\beta}$ in terms of structural features which are not evident in the Fournier Forand equivalents, calculated according to Mobley et al. (2002)[Fig. 3.1(D)], and the shape of the relative percentage differences ($\tilde{\beta}_{EAP} - \tilde{\beta}_{FF}$) between them agreeing well with Chami et al. (2006a) (their Fig. 3.4, here Fig. 3.2), although varying somewhat in magnitude at very small scattering angles. Also notable are the interference structures most evident at small D_{eff}. Their prominence is reduced with larger D_{eff} as the high-angular resolution discrete particle size phase functions are integrated over a greater range of particle sizes, where the correspondingly larger core spheres absorb more, reducing reflected light at the outer/core sphere interface. They are likewise reduced by increasing the

size distribution's effective variance (Mishchenko et al., 2002). The resulting phase functions at larger D_{eff} are shapewise more consistent with Chami's data. These features are not seen in measured oceanic VSF data, as natural waters generally contain both phytoplankton and non-algal sources of scattering, and also have unique particle size distributions.

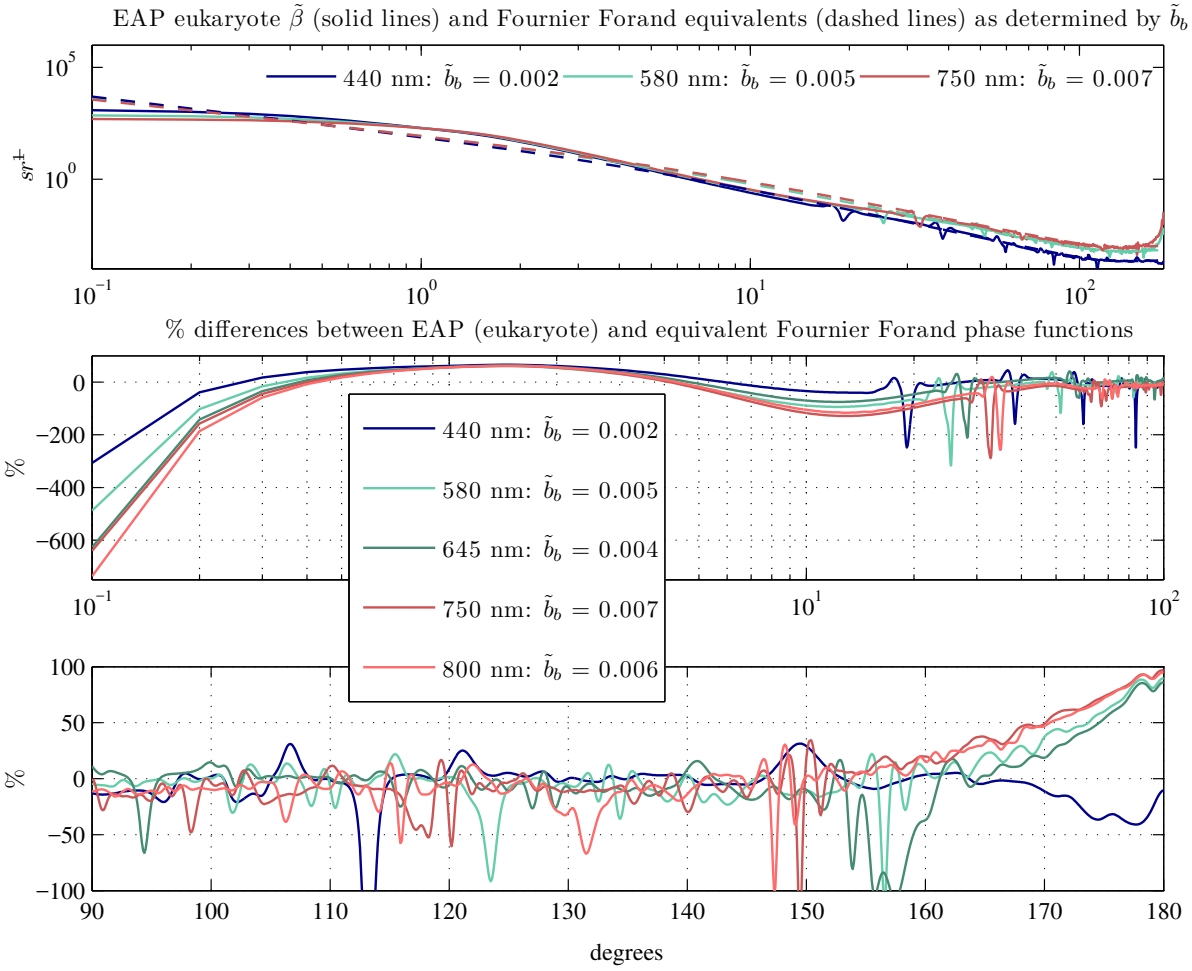

Figure 3.2: Percentage differences between $\tilde{\beta}_{EAP}$ for a generalised eukaryote assemblage with D_{eff} = 12 μm, and corresponding $\tilde{\beta}_{FF}$. Percentages are calculated by $(\tilde{\beta}_{EAP}\text{-}\tilde{\beta}_{FF})/\tilde{\beta}_{EAP} * 100$. Selected phase functions for different wavelengths and phytoplankton backscatter fractions are shown in the top panel. The differences between them are shown in the bottom two panels: 0.1° to 100° are shown on a log scale, and 90° to 180° below. These phase functions were selected to illustrate variability in wavelength and backscatter fraction, and how the differences between $\tilde{\beta}_{EAP}$ and $\tilde{\beta}_{FF}$ vary with both of these parameters.

3.3.2 Comparing the Fournier Forand and EAP phase functions: prokaryote (vacuolate) group

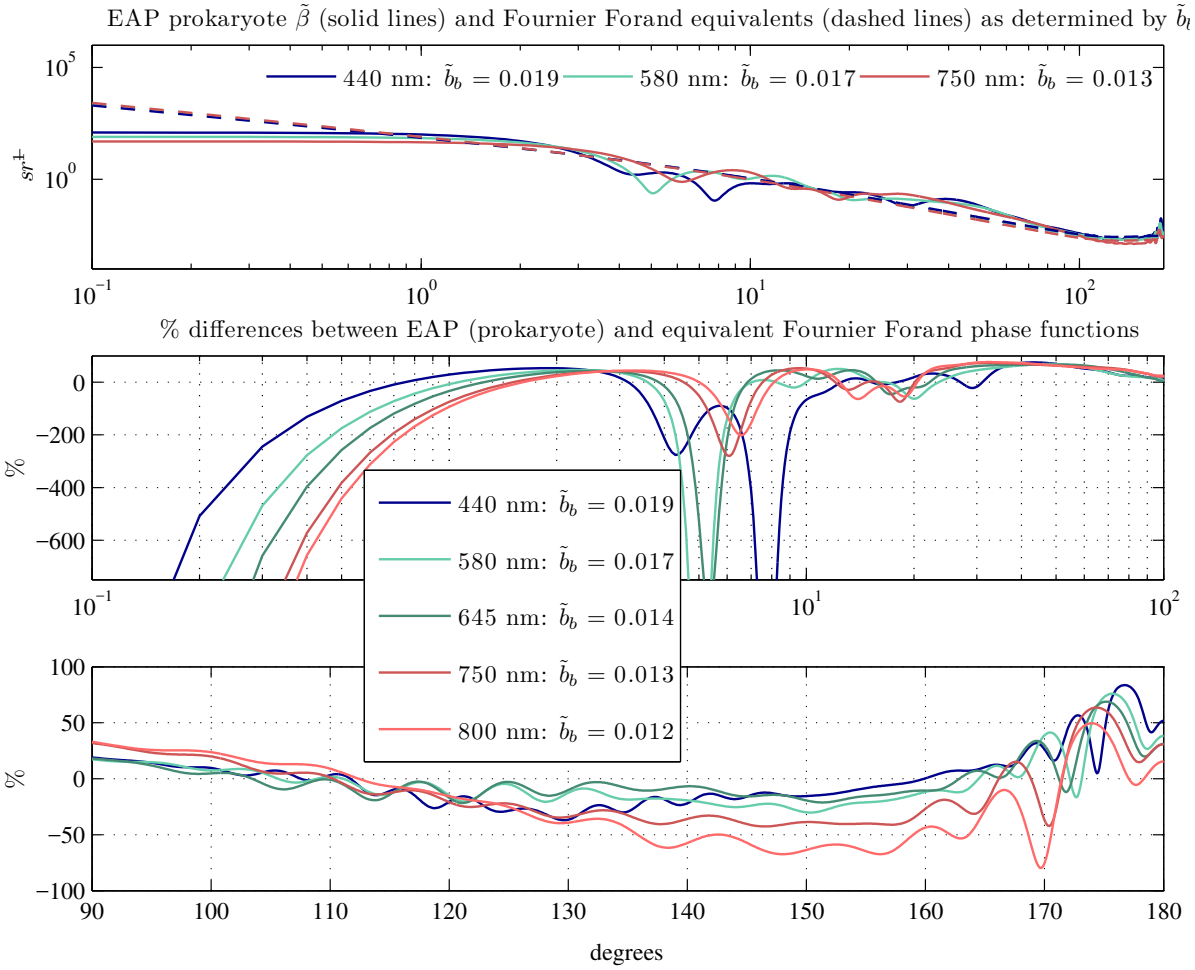

Figure 3.3: Selected EAP phase functions for a generalised prokaryote (vacuolate) assemblage with $D_{eff} = 5\ \mu m$, are shown in the top panel together with their corresponding $\tilde{\beta}_{FF}$, and the percentage differences between them are shown in the panels below.

Figure 3.3 shows the analagous comparison of vacuolate $\tilde{\beta}_{EAP}$ with the equivalent $\tilde{\beta}_{FF}$ as determined by the appropriate particulate backscatter fraction. Both eukaryotic (dinoflagellate) and prokaryotic (cyanobacterial) $\tilde{\beta}_{EAP}$ have reduced small angle maxima with respect to to their corresponding $\tilde{\beta}_{FF}$, but the cyanobacterial $\tilde{\beta}_{EAP}$ is reduced to a much greater extent. The reduction in forward light scatter is caused by the lowering of the overall real refractive index of the cell by the gas vacuole (Volten et al., 1998). The reduction of scatter at small angles is compensated for

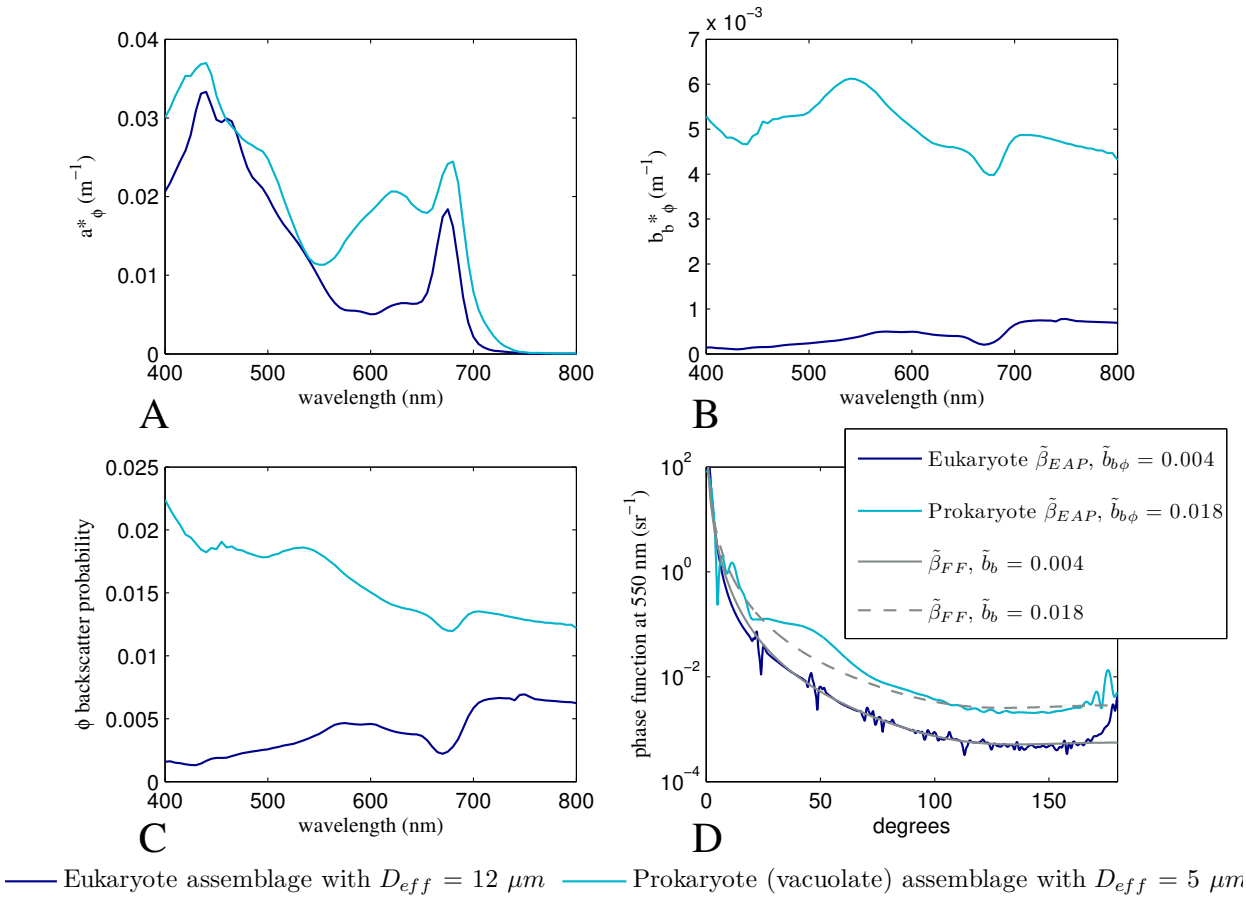

Figure 3.4: IOPs for generalised eukaryote and prokaryote assemblages, with effective diameters of 12 and 5 μm respectively.The elevated total scatter by the prokaryotes (B), and correspondingly elevated backscatter probability (C), is reflected in the comparatively higher phase function values (D), with unique angular variability (D). The angular variability in the phase function of the highly scattering prokaryote assemblage is markedly different in shape from the equivalent $\tilde{\beta}_{FF}$.

by a noticeable increase in scatter compared to the $\tilde{\beta}_{FF}$ at intermediate angles of 20° to about 100°. The high perpendicular light scatter was also attributed to gas vacuoles in cyanobacteria, observed experimentally (Dubelaar et al., 1987). This is therefore not evident in the case of the dinoflagellates. The contrasting IOPs of these two populations are presented in Figs. 3.4(A)–3.4(C), together with the 550 nm phase function for each population and its Fournier Forand equivalent in Fig. 3.4(D).

3.3.3 High Biomass Validation of EAP phase functions in terms of resulting modelled R_{rs}

In Case 1 bloom conditions (Chl $a > 100\ mg.m^{-3}$) it can be assumed that the phytoplankton IOPs dominate the IOP budget, and Benguela blooms therefore offer an ideal opportunity to compare the use of the EAP and FF phase functions in terms of their impact on the R_{rs}. Mean measured R_{rs} are shown for three samples in Fig. 3.5, with the standard deviation representing the variability in the measurements. The measurements are all from a 2005 Southern Benguela bloom (see (Lain et al., 2014)) dominated by *Prorocentrum triestinum*, a small dinoflagellate approximately 18-22 μm in length and 6-11 μm in width. Size was measured by Coulter Counter (see (Evers-King et al., 2014)), with a resulting effective diameter of 13.1 μm $\pm$ 1.2.

The modelled $R_{rs}(\lambda)$ were generated using a 4-component Hydrolight 5.2 model with non-algal particle (NAP) scatter $b_{nap}(\lambda)$, combined gelbstof and detrital absorption $a_{gd}(\lambda)$ and phytoplankton components as detailed in (Lain et al., 2014). This method describes the use of the combined spectrally variant particulate $\tilde{b}_b(\lambda)$ to determine an appropriate $\tilde{\beta}_{FF}$. For this exercise, for comparison with the combined $\tilde{b}_b$ Fournier Forand approach, the appropriate $\tilde{\beta}_{EAP}$ were used for the phytoplankton component, combined with a 1% $\tilde{b}_b$-determined $\tilde{\beta}_{FF}$ for the non-algal particulate component. Because the $\tilde{\beta}_{EAP}$ vary with both $\tilde{b}_b$ and λ, it was only possible to model this in Hydrolight using 101 single-wavelength runs (400 to 900 nm at 5 nm resolution) and collating the results to get the full spectral R_{rs}. This means that the effects of fluorescence could unfortunately not be included, so deviation from the measured R_{rs} is to be expected in the 683 nm Chl a fluorescence region and will be ignored in this discussion.

Forward modelled populations of D_{eff} of both 12 and 16 μm are presented, to illustrate how the influence of particle size is inextricable from that of the choice of scattering functions unless size information is known. The corresponding FF R_{rs} are much brighter than their EAP counterparts. This is consistent with the differences in phase functions as described earlier, and also with previously published results (Chami et al., 2006a; Tuchow et al., 2016). While a good fit in terms of shape and

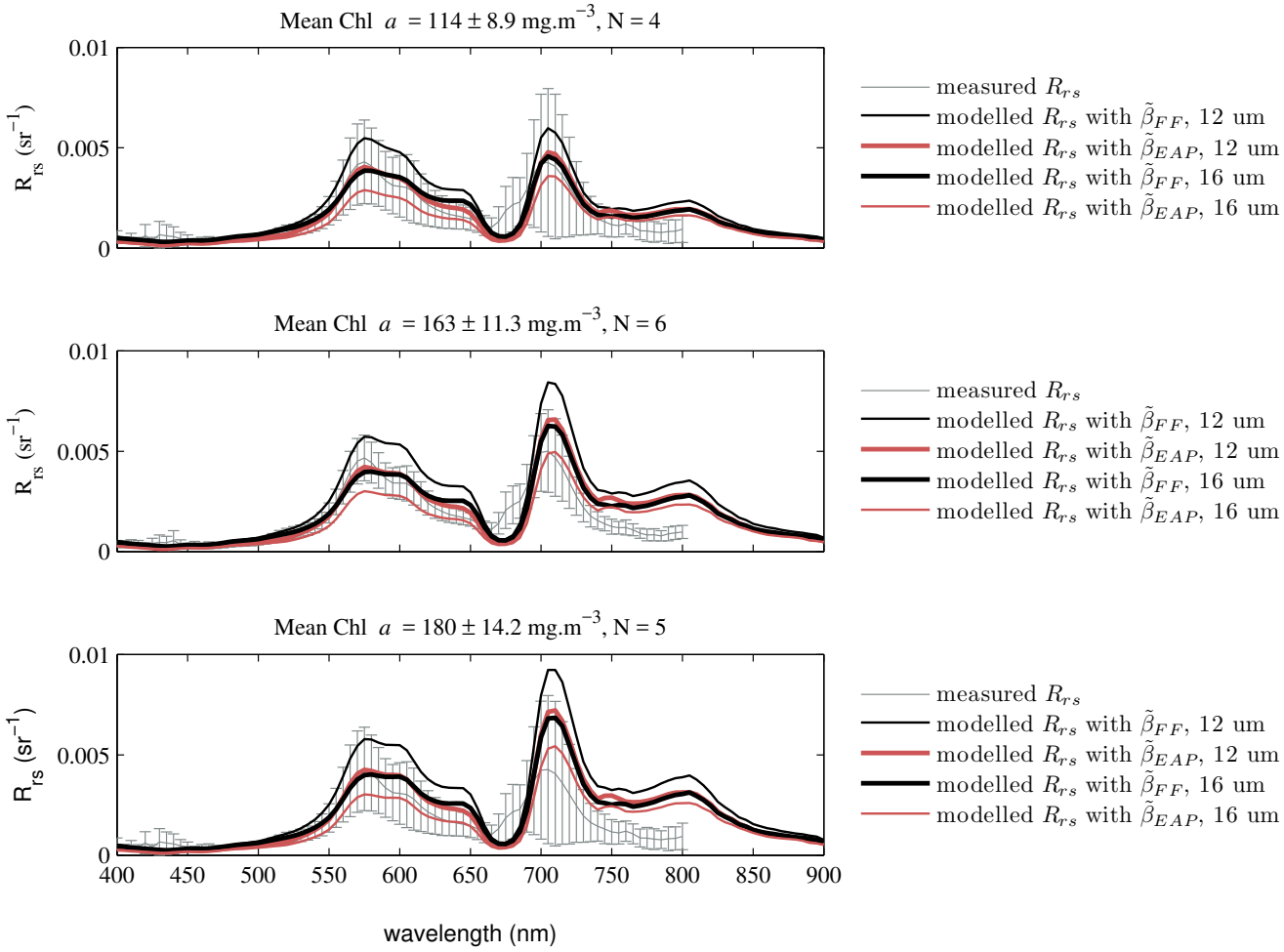

Figure 3.5: Demonstration of measured/modelled R_{rs} closure for 3 high biomass examples from a 2005 bloom in the Southern Benguela. The corresponding FF R_{rs} are much brighter than their EAP counterparts.

magnitude is attainable with $\tilde{\beta}_{FF}$ combined with a larger D_{eff}, the proper assessment of uncertainty due to choice of phase function must be measured between R_{rs} modelled with identical size parameters. When it comes to model closure, this ambiguity in contributions to brightness of the R_{rs} must be satisfactorily resolved. To be clear, in the absence of more detailed assemblage information from this bloom, no definitive conclusion can be made about any advantage of the $\tilde{\beta}_{EAP}$ at 12 μm over the $\tilde{\beta}_{FF}$ at 16 μm in terms of validation of either model with respect to the measurements. But when evaluating the impact of choice of phase function in modelling R_{rs}, the comparison must be made between FF and EAP R_{rs} resulting from

the use of the same population effective diameter - these differences indicate the uncertainty attributable only to the phase function.

In both versions of the modelled R_{rs} there is a notable deviation from the measured data from about 730 nm onwards, although the two modelled versions agree well. Mobley et al. (Mobley et al., 2002) describe a drop off in instrument performance (resulting in underestimated upwelling radiance L_u) as the signal approaches the instrument noise level with depth - the TSRB measures at a depth of 0.66 m, which in such high biomass equates to many optical depths in the NIR, leading to greater uncertainties at these wavelengths due to rapid light attenuation and instrument self-shading, particularly in the red region where absorption by water is significant (Leathers et al., 2001). In addition, the measured data were not corrected for temperature-dependent absorption by water in the near infra-red (NIR). Pending further measurements no further comment can be made on the deviation of both modelled R_{rs} from the measurements in this region.

Importantly, the 709 nm region (carrying critical biomass and assemblage-related signal (Matthews et al., 2012)) is sensitive to the use of the comparative phase functions in the modelled data. Likewise, large differences are noticeable in the 550 - 650 nm region. Both of these regions (550 to 650 nm, and 709 nm peak) contain absorption features of diagnostic accessory pigments useful in resolving for example, trophic status and the presence of diagnostic features of cyanobacteria, including phycocyanin pigment (Simis et al., 2005; Matthews et al., 2012), and have previously been identified as sensitive to size-related assemblage variability as well (Evers-King et al., 2014). Information in these critical spectral regions is vital for PFT algorithm development including inversions and the retrieval of IOPs.

Figure 3.6 shows the R_{rs} generated from Hydrolight, resulting from the use of the $\tilde{\beta}_{EAP}$ and $\tilde{\beta}_{FF}$ respectively for idealised prokaryote and eukaryote populations. These modelled examples were run for Chl *a* values of 1, 10, 100 and 500 mg.m^{-3} in order to show the progressive effect of the difference in phase function as trophic status increases. In order to isolate the effect of the phytoplankton absorption and scattering, additional optical components are not included here (i.e. absorption by gelbstoff and/or tripton, and additional small particle/sediment/detrital scattering).

This is not the case in natural waters and these examples are intended as illustrative.

When examining the R_{rs} systematically in this way, the resulting effect of the differences in shape and magnitude of the phase functions becomes apparent. Overall, the cyanobacterial R_{rs} (as representative of a prokaryotic assemblage) using the $\tilde{\beta}_{EAP}$ are brighter than the R_{rs} using the corresponding $\tilde{\beta}_{FF}$. However this is not the case with the mixed dinoflagellates (representing eukaryotes). Here, the R_{rs} resulting from the use of the $\tilde{\beta}_{FF}$ are brighter overall. This appears to indicate that the greatly elevated scatter seen in the intermediate angles of the vacuolate $\tilde{\beta}_{EAP}$ contributes significantly to the overall magnitude of the spectral R_{rs}. This observation is consistent with Chami et al's 2006 Monte Carlo experiment which determined, among other results, that in highly scattering conditions brighter R_{rs} is due to the phase function being greater at angles 10° to 100° (Chami et al., 2006a). Differences observed in the R_{rs} in a single scattering environment (where differences in small angle scattering are important) are magnified in a multiple scattering environment, where increased variability in scattering at the intermediate angles is seen.

The EAP model has significant potential as a tool for evaluating the PFT signal across different biomass and IOP ranges. The large differences in the phase functions themselves have been presented above, and their impact on model closure explored. Detailed modelling of the interaction of biophysical relationships is now possible with some understanding of causality. Figures 3.7 and 3.8 show that differences in phase function shape are translated into significant uncertainties in the R_{rs} even at quite low biomass where total particulate scatter is small, such as in an oceanic environment. The contribution of non-algal scatter is modelled with $b_{bnap}(550) = 0.0005$ m^{-1} (Evers-King et al., 2014). 'Model uncertainty' denotes the difference in R_{rs} resulting from the use of either $\tilde{\beta}_{EAP}$ or $\tilde{\beta}_{FF}$ in the radiative transfer calculation. For a eukaryote (e.g. dinoflagellate) phytoplankton population with effective diameter of 6 μm (Fig. 3.7), the absolute magnitude of the model uncertainty is in the order of 10^{-4} from a Chl a concentration of 1 mg.m^{-3}, which is significant given that the instrument threshhold resolution of measured reflectance is about 1x10^{-4} sr^{-1} (Chami et al., 2006a). Figure 3.9 shows the actual comparative R_{rs} at selected wavelengths of the large and small absolute and percentage differences discussed

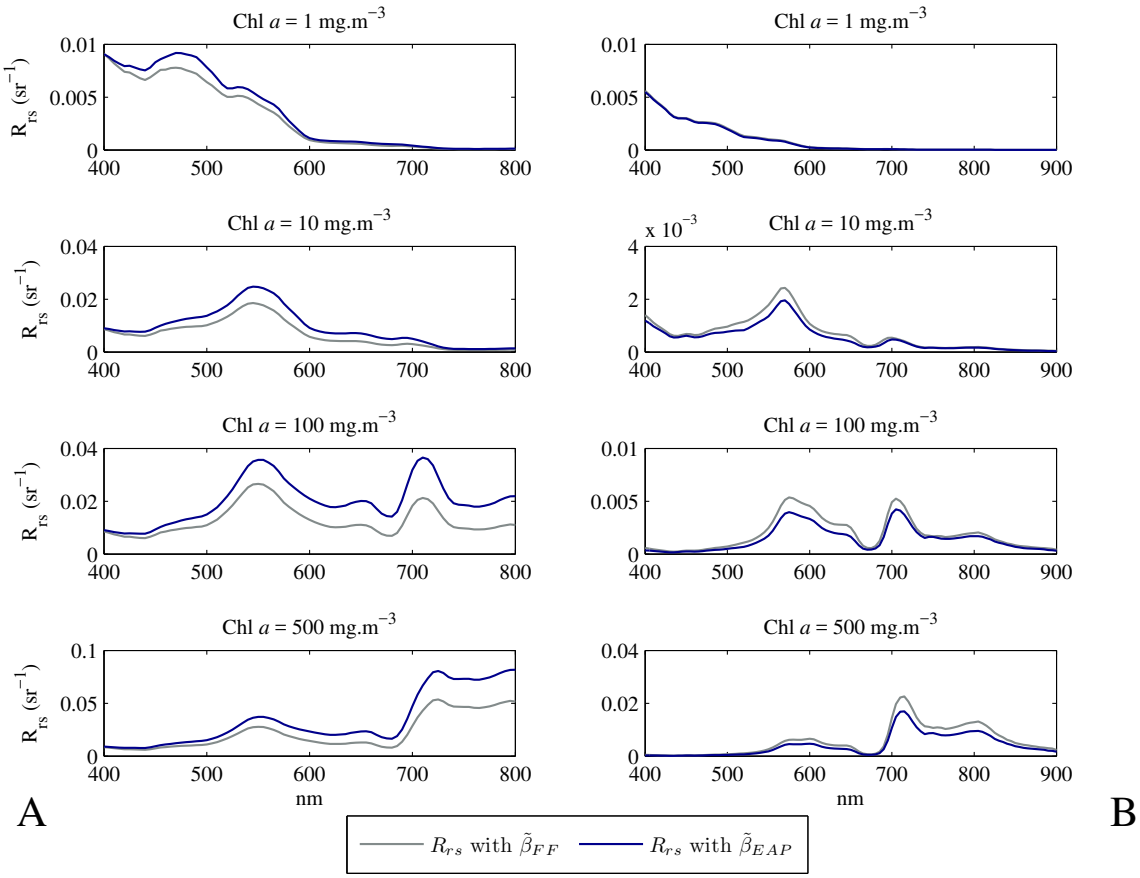

Figure 3.6: Modelled R_{rs} for prokaryotes (cyanobacteria) (A), with $D_{eff} = 5\ \mu m$, and eukaryotes (mixed dinoflagellates) (B), with $D_{eff} = 12\ \mu m$, for increasing Chl $a = 1$, 10, 100 and 500 mg.m^{-3}.

with respect to Figs. 3.7 and 3.8.

The spectral variability of the absolute differences in R_{rs} means that the comparative $\tilde{\beta}_{EAP}$ or $\tilde{\beta}_{FF}$ R_{rs} yield notably different shapes in many spectral regions. The absolute differences translate into percentages of over 10% across much of the spectrum, and notably in diagnostically important regions for PFT analysis. The effect of an increased population effective diameter can be seen in Fig. 3.8, showing that at the same biomass, both the absolute and percentage differences are reduced for a 16 μm population with respect to the 6 μm example. This is due to the elevated total scatter by smaller cells - which means pronounced spectral variability in the backscatter, translating into large differences between the shapes of the Fournier Forand and EAP phase functions. Harmel et al. (2016) observe that the most notable source of inaccuracy of the Fournier Forand approximation is in the region from 150^o upwards, and these results appear to confirm this. In the bottom panel

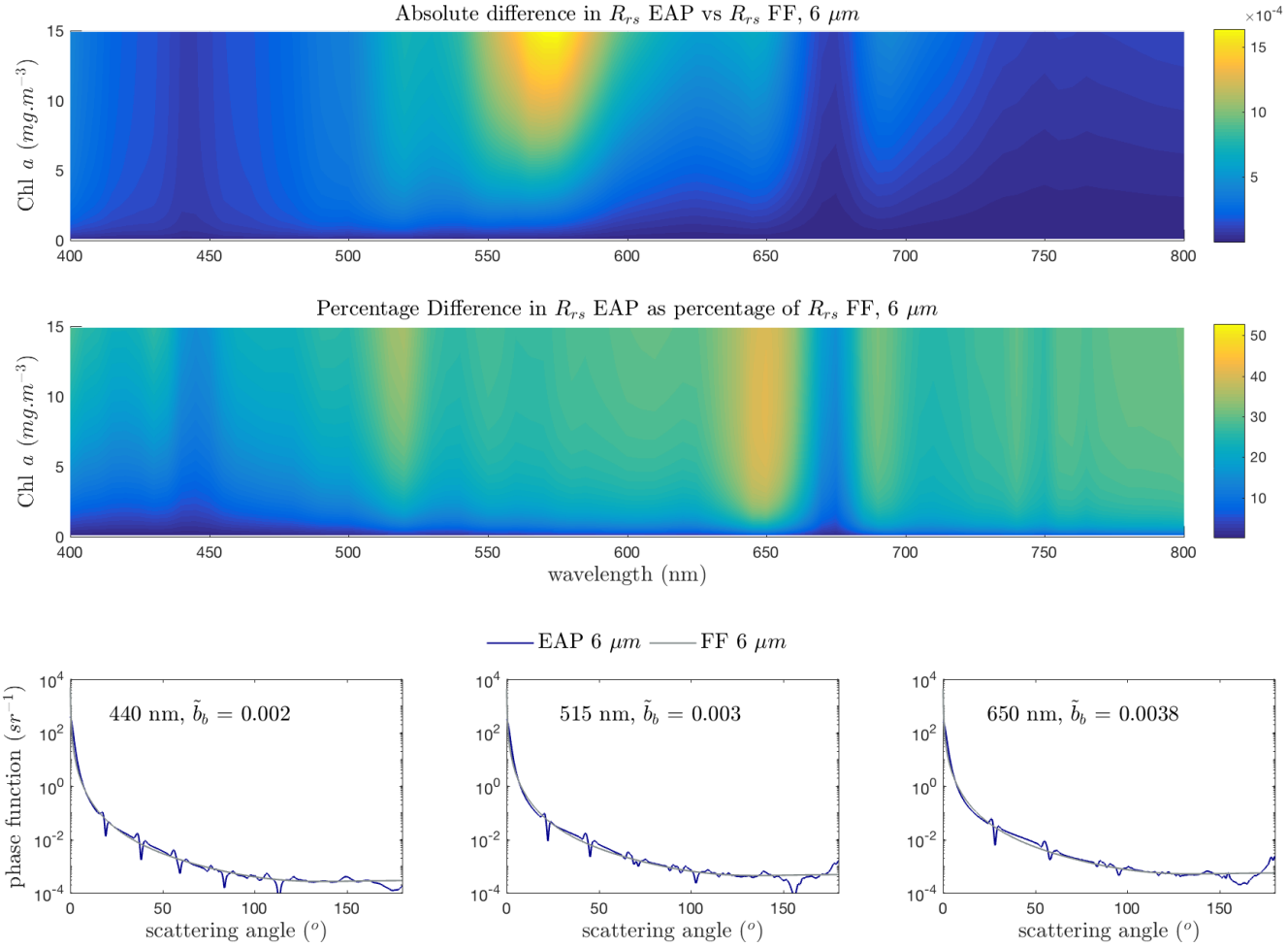

Figure 3.7: Differences between R_{rs} EAP and R_{rs} FF, R_{rs} expressed per steradian (above) and as unsigned percentages of R_{rs} FF (below), shown for a generalised 6 μm population against a background of low NAP backscatter ($b_{bnap}(550) = 0.0005$ m^{-1}). Comparative EAP and FF phase functions for 3 different wavelengths and backscatter fractions are presented in the bottom row.

of each figure, three wavelengths have been selected to examine this effect further: 440 nm is an area of low resulting difference in R_{rs} (due to large absorption by phytoplankton and thus a reduced number of photons available for scattering), and the differences between $\tilde{\beta}_{EAP}$ and $\tilde{\beta}_{FF}$ are the smallest of the three cases - negligible for the 16 μm example, which results in comparably small R_{rs} error. 515 nm is an area of intermediate difference in the R_{rs} which corresponds to some divergence in the phase functions, while 650 nm represents an area of large divergence in the R_{rs} and shows sizeable differences between $\tilde{\beta}_{EAP}$ and $\tilde{\beta}_{FF}$ post 150^o.

Both figures show Chl a from 0 to 15 mg.m^{-3}, but it should be considered that

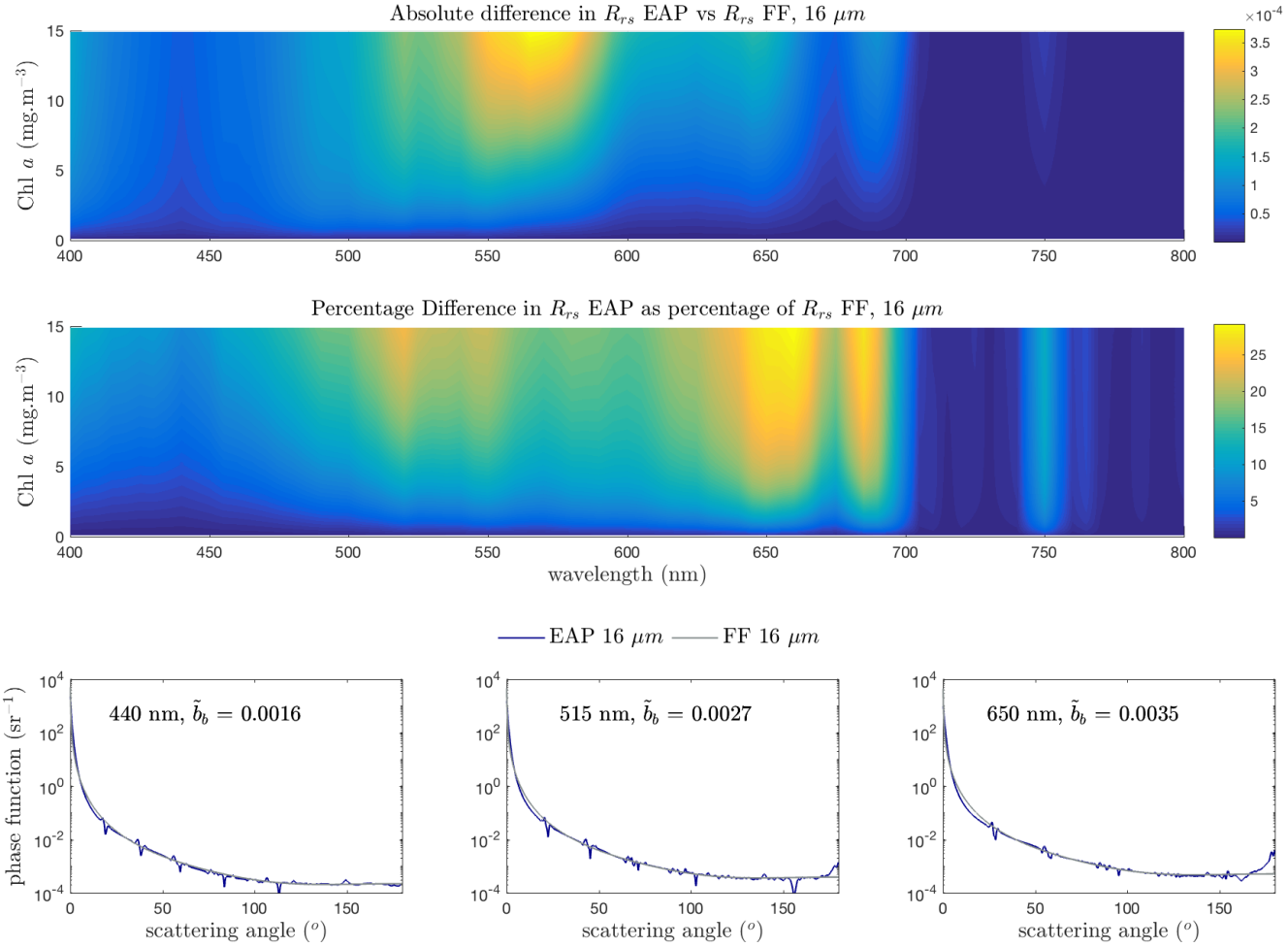

Figure 3.8: Differences between R_{rs} EAP and R_{rs} FF, R_{rs} expressed per steradian (above) and as unsigned percentages of R_{rs} FF (below), shown for a generalised 16 μm population, low NAP ($b_{bnap}(550) = 0.0005$ m^{-1}) conditions. Comparative EAP and FF phase functions for 3 different wavelengths and backscatter fractions are presented in the bottom row.

in practice it is likely that a 16 μm population of eukaryotes (e.g. diatoms) would occur at the higher end of this Chl a scale while a 6 μm population would be observed at the lower end (Ciotti et al., 2002), and so the magnitude of differences in R_{rs} are comparable when considering the respective ecological niches of these populations. At low biomass, the impact on R_{rs} due to choice of phase function is greater for small cells than for a large celled population because small cells scatter proportionally more: in certain spectral regions differences of 30% are seen as low as Chl $a = 1.5$ mg.m^{-3} for a 6 μm population. At high biomass the uncertainty due to the phase function grows because of the increased number of cells.

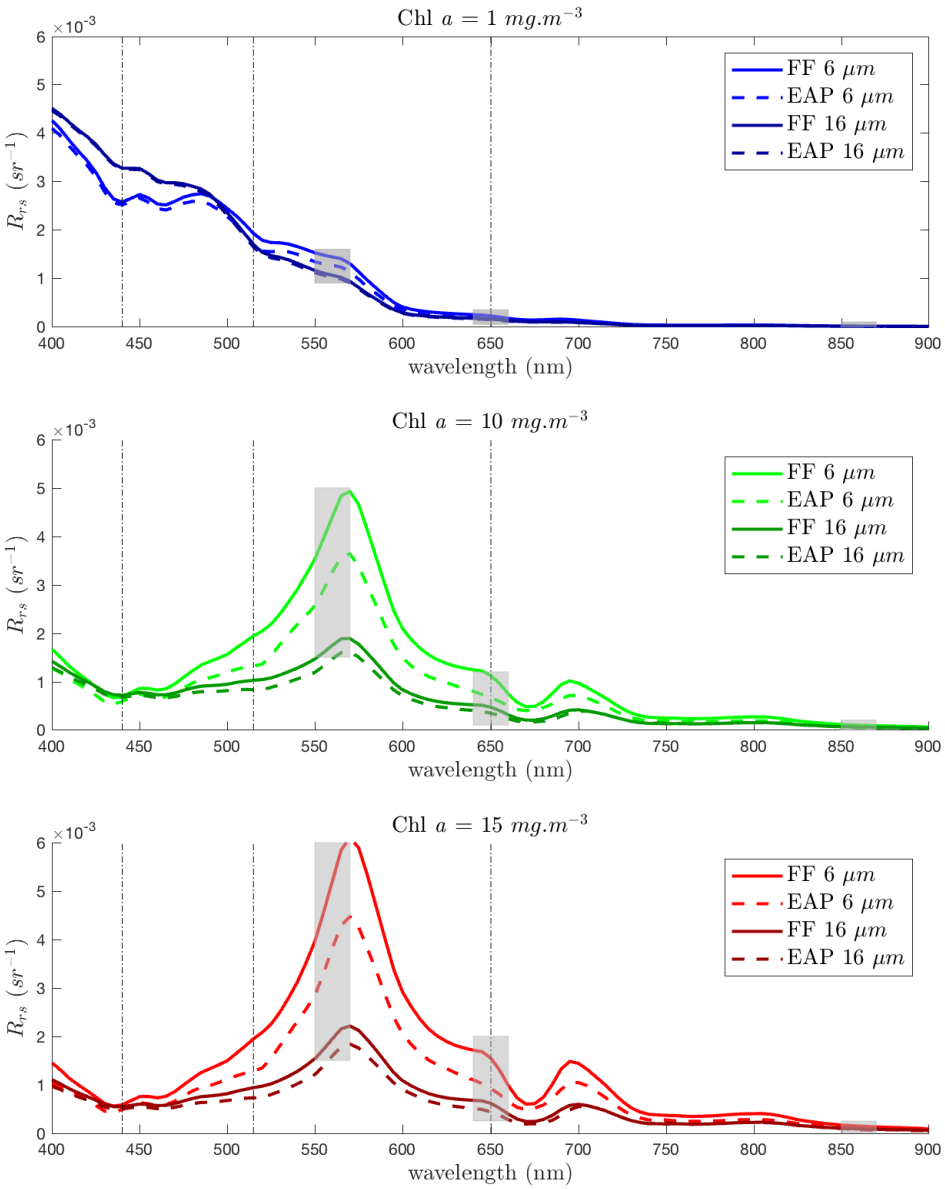

Figure 3.9: R_{rs} EAP and R_{rs} FF, R_{rs} shown for generalised 6 and 16 μm populations in low NAP ($b_{bnap}(550) = 0.0005$ m^{-1}) conditions. The vertical dot-dashed lines indicate the wavelengths for which the phase functions are shown in Figs. 3.7 and 3.8. The grey boxes identify three example regions of high absolute and low percentage error (shown in Figs. 3.7 and 3.8) and vice versa.

3.4 Conclusions

It is evident that given the impracticalities of VSF and phase function measurements, only by modelling can we generate phytoplankton-specific phase functions across wide ranges of assemblages and water types. The need for angularly resolved VSFs both measured and modelled has been articulated elsewhere (Chami et al., 2014; Tan et al., 2013) and confirmed here. The EAP model presents a full physics-based calculation of the directional scattering characteristics of various modelled phytoplankton populations, unveiling a new opportunity to further understanding of the importance and impact of the highly variable spectral and angular scattering properties of phytoplankton. It is clear that to properly address the PFT question, detailed variability in phytoplankton phase functions must be represented.

In both forward and inverse models in use by the ocean colour community, reflectance is generally simplified in one of two ways: either by approximating the phase functions themselves, or by avoiding the radiative transfer calculation altogether and instead representing the bidirectional character of the upwelling light field using an f/Q parameter (Zaneveld, 1995). These are powerful and necessary tools but it is important to properly understand the implications of these approximations in a PFT context, given that the magnitude of the uncertainty in R_{rs} due to choice of phase functions has been shown here to be significant. A previous study on accuracy and ambiguity in inversion models making these approximations (including a Fournier Forand version of the EAP model) describes the difficulties encountered by these models in highly scattering waters (Evers-King et al., 2014). It has been shown in this chapter that even for intermediate levels of phytoplankton scatter (whether due to elevated biomass or small particle sizes), the question of an appropriate phase function must be adequately addressed if measurement/model closure is to be attained.

It is clear that there is considerably more variability in the spectral and angular scattering properties of phytoplankton than is either explicity or implicity acknowledged by the ocean colour community. It is also clear that this variability has considerable effect on the spectral nature of the water-leaving radiance.

Due to the technical computing challenges of routinely using the EAP phyto-

plankton phase functions in a coupled EAP-Hydrolight model, the best available solution of a $\tilde{b}_b$ - specific Fournier Forand formulation is used for all modelling going forwards unless explicitly stated otherwise. However, uncertainty in the EAP phytoplankton-related signal due to the choice of phase function remains an important consideration, and further results are contextualised with this in mind.

Chapter 4

Biomass, size and pigments: the EAP model and the PFT signal

4.1 Introduction

The ability to retrieve Phytoplankton Functional Type from satellite radiometry is central to being able to accurately assess the ocean's role in climate and climate change (Le Quéré et al., 2005). Due to immense species diversity and variability in distribution, the Phytoplankton Functional Type (PFT) approach (e.g. Sathyendranath et al. (2004); Alvain et al. (2005); Ciotti and Bricaud (2006); Nair et al. (2008)) groups phytoplankton species according to their biogeochemical function and attempts to relate this to their biophysical characteristics, primarily their size (Le Quéré et al., 2005; Kostadinov et al., 2009; IOCCG, 2014). This approach is important for oceanic waters, characterised by widespread but low biomass, which contribute the largest proportion of global oceanic primary production (Field et al., 1998). Cell size governs many biological traits (Dutkiewicz et al., 2015); smaller phytoplankton are widespread and play an important role in nutrient recycling, while larger phytoplankton display the highest growth rates (Dutkiewicz et al., 2015). The dynamics of phytoplankton ecology have profound and intricate influence not only on oceanic biogeochemistry (e.g. acidification, and its effects on both CO_2 uptake and on marine life) but also on higher trophic levels e.g. fisheries, as certain phytoplankton environments promote the development of different fish populations

(IOCCG, 2014). A size-based PFT approach is particularly meaningful in the context of carbon sequestration (Le Quéré et al., 2005), as particle size in large part determines sinking rates.

But phytoplankton ecology is complex, and modelling PFTs with adequate parameterisation in a biogeochemical context is consequently extremely challenging (Anderson, 2005). When applying these models to satellite data there is additional uncertainty in relating biogeochemical parameters to optical ones. Abundance-type approaches, following observed relationships between phytoplankton assemblage taxonomic information (e.g. pigments) and biomass, show good results in low biomass conditions where the covariability of the phytoplankton optical contribution with that of other in-water consituents generally holds (Sauer et al., 2012), but do not address the sources of second order variability (Brown et al., 2008), or the likelihood that these empirical relationships will not withstand the ecological shifts resulting from changing climatic conditions (Brewin et al., 2017). A biophysical approach to PFTs is likely to have greater validity in a future ocean.

It is suggested that a thorough and meaningful approach to understanding and detecting the PFT signal from satellite radiometry comprises three main components: a good forward model addressing the causal nature of the optical signal, an assessment of the potential for inversion in terms of signal ambiguity, and a further constraining of all of this information with respect to sensor measurement uncertainty, including that of derived quantities such as the R_{rs}. This chapter addresses primarily the first requirement: the forward modelling of the causal optical signal. This allows an assessment of the magnitude, sensitivity, and spectral location of the PFT signal under varying conditions, and informs on the ambiguity-related complexity and potential constraints of the second step, the inversion (Evers-King et al., 2014).

To clarify for the purposes of this chapter, natural waters with Chl *a* concentrations of less than 5 mg.m^{-3} are referred to as "low biomass", and upwards of this as "high biomass". However this distinction is a nominal one, here used entirely in an optical sense, based on observations of approximate PFT detection change thresholds by the EAP model. Discussion with reference to approaches used by

other authors for low biomass generally implies those used for oligotrophic oceanic conditions, and so are expected to be appropriate only for very low biomass within the < 5 mg.m^{-3} frame of reference used here.

In low biomass it is the strong absorption by phytoplankton which dominates the phytoplankton contribution to the ocean colour signature, and has therefore been identified as a promising signal in terms of PFT identification e.g. (Alvain et al., 2005; Devred et al., 2006) and others. However, it appears that the relative contributions of phytoplankton absorption and scatter change with biomass, size and other functional type traits, and as the $a_{gd}(\lambda)$ and $b_{bnap}(\lambda)$ components vary. Brewin et al. (2017) acknowledges that as biomass increases, both the abundance-based approaches as well as approaches relying on differential absorption, break down. In Chapter 2 it was concluded that the EAP model's detailed handling of phytoplankton spectral backscatter is a vital aspect of successfully modelling high biomass waters, and it follows that the scattering contribution should be examined further in the context of the causal phytoplankton signal.

The total water-leaving signal represents the complex interaction of each in-water consistuent's absorption and scattering properties. Contributions to the bulk water-leaving signal can be addressed in terms of cell counts, Chl *a* concentration, carbon, or any other biophysical quantity. Here the contribution of phytoplankton to the R_{rs} is discussed with the aim of determining under which bulk IOP conditions there is enough signal due to phytoplankton to be able to observe PFT-related features. Furthermore, the causality of the signal within the phytoplankton component is a key question towards understanding when and how PFT information might be derived.

It has been observed that the most important sources of second order variability in ocean colour are absorption due to CDOM and detrital particles, i.e. $a_{gd}(\lambda)$, and particulate backscatter i.e. $b_b(\lambda)$ (Brown et al., 2008). Backscatter anomaly maps (i.e. backscatter independent of variability due to biomass) correlate approximately with phytoplankton type distribution maps (Brown et al., 2008) calculated from optical anomalies which are attributed to differences in phytoplankton accessory pigments (Alvain et al., 2005) rather than backscattering characteristics. This leads

to the suggestion, in Brown et al. (2008), that the Alvain criteria used to distinguish PFTs, identified as representing absorption signatures (Alvain et al., 2005), are in fact primarily due to backscattering characteristics (Brown et al., 2008), indicating that phytoplankton groups either directly determine, or perhaps are simply associated with, backscattering variability around the mean.

As concluded in (Brown et al., 2008), these relationships can only be fully explored if a method is applied where the phytoplankton groups are causally linked to the optical conditions. The EAP model provides exactly such a method, and is used here to investigate the impact of size-based PFTs on the optical signal, and to confirm the assertion (Matsuoka et al., 2007; Brown et al., 2008) that biomass drives the largest part of observed variability in the water-leaving signal, and that the radiometric signal in the blue is ambiguous due to the effects of $a_{gd}(\lambda)$, and the additional effects of $b_{bnap}(\lambda)$.

At the core of the PFT problem is the question of ambiguity. The bulk water-leaving signal is a delicate balance of the frequently opposing optical effects of biomass, D_{eff}, second order assemblage variability such as size, pigments and ultrastructure, and the non-algal in-water consistuents. This chapter presents a series of experiments to determine quantitatively under which bulk optical conditions the influence of phytoplankton cell size, in terms of assemblage effective diameter (D_{eff}), as well as differential pigmentation, can be identified in the water-leaving signal. The first case studies address only changes in biomass and effective diameter i.e. assemblage changes relating to phytoplankton with similar spectral absorption properties based on their primary pigmentation. The broad absorption peaks around 500 nm characteristic of both fucoxanthin and peridinin, dominant light-harvesting pigments of diatoms and dinoflagellates respectively (see Section 1.2), allows for reasonable optical comparison of diatom and dinoflagellate-dominated assemblages based on their D_{eff}. In the final two case studies, some pigment variability is introduced to demonstrate that while fine spectral resolution might improve opportunities to identify individual pigments and hence PFT information, the constraints of biomass and D_{eff} with respect to the magnitude of the PFT signal, and ambiguities in the water-leaving signal, still remain. The persistent dependence of the magnitude of

the PFT signal on the IOP budget is a primary focus of this chapter.

4.2 Modelling approach

The EAP IOPs used in this chapter are from two groups, calculated using the generalised diatom-dinoflagellate refractive indices and a set of phycoerythrin-based refractive indices (originally derived from measurements of *Mesodinium Rubra* (Bernard et al., 2009)). They are presented in Appendix A. These are combined, in various proportions as indicated, with appropriate non-algal optical constituents as detailed for each experiment. Water types are considered homogenous with depth, generic atmospheric and geographic conditions, and the full radiative transfer solution is calculated by Hydrolight at a spectral resolution of 5 nm. Given the technical challenges with using EAP phase functions for modelling high resolution spectra, a Fournier Forand phase function chosen for the backscatter fraction of the combined particulate IOPs is used at each wavelength throughout these experiments. A basic fluorescence efficiency model is included for completeness (see Section 2.2) but modelling this spectral region accurately is challenging and outside of the scope of this work, so the features of this spectral region are not discussed in terms of PFT sensitivity.

4.3 Interpreting the R_{rs} signal

4.3.1 Deconvolving the optically significant constituents

The combined effects of assemblage D_{eff} and biomass, together with non-algal optical contributors, are not easily interpreted from the water-leaving signal as these quantities have ambiguous effects on the bulk optics (Evers-King et al., 2014). Following a general allometric abundance approximation of increasing effective diameter with biomass (Agusti et al., 1987), elevated scattering associated with the increased number of cells brightens the R_{rs}, but the associated decrease in D_{eff} acts to reduce R_{rs}. So a dense, small celled population would have a large reflectance signal, with elevated scatter due to both cell numbers and cell size - hence species such as *Au-*

reococcus anophagefferens are detectable in bloom (Quirantes and Bernard, 2006; Probyn et al., 2010). Other particularly highly scattering species such as coccolithophores are also easily detectable due to their massive impact on water-leaving reflectance, which is due in this case to their ultrastructure - their calcium carbonate liths are highly reflective particularly when detached (Vance et al., 1998).

$a_{gd}(\lambda)$ provides a further layer of complexity by ambiguating the phytoplankton signal with further absorption in the blue. Additionally, $b_{bnap}(\lambda)$ can make a significant contribution to the total backscatter (Dall'Olmo et al., 2009) but is not very well characterised (Stramski et al., 2004) and likely comprises two components - that portion which may vary approximately predictably with biomass (e.g. phytoplankton detritus), and the portion which likely does not (e.g. the ubiquitous but uncharacterised contribution of bubbles, sediment and/or aeolian particles (Stramski et al., 2004)). These optical components may be associated with, but not determined by, certain phytoplankton groups (Brown et al., 2008), such as populations of highly scattering bacteria attendant to diatoms (Moutier et al., 2017).

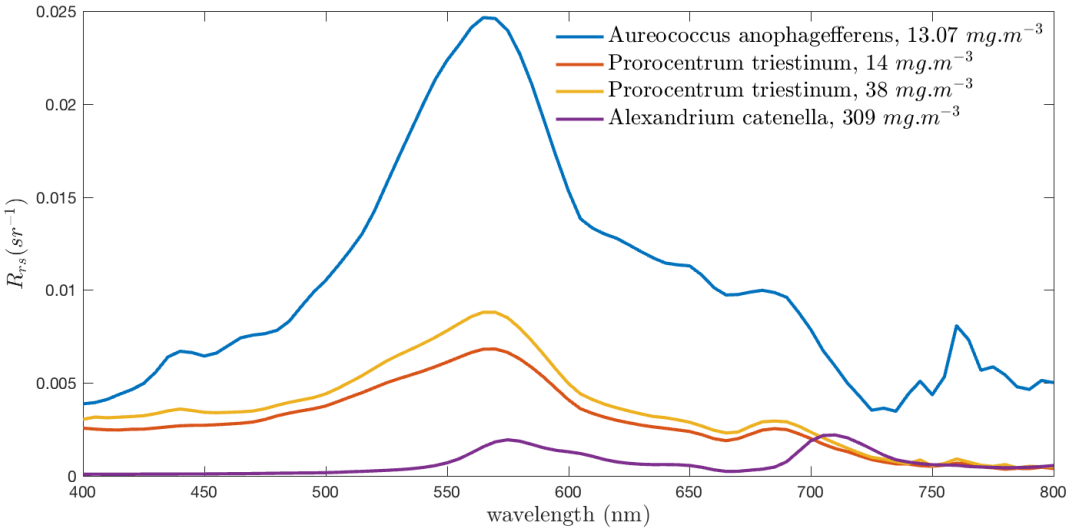

Figure 4.1: Variability in the R_{rs} signal in phytoplankton-dominated waters: Measured R_{rs} from 3 bloom events in the southern Benguela (processing in Appendix B).

Figure 4.1 illustrates the combined effects of assemblage D_{eff} and biomass. These are measured R_{rs} data [processing in Appendix B], from blooms in the Southern Benguela region dominated by the species indicated. The huge cell counts

(around 6 $\times$ 10^8 cells per litre) from the *Aureococcus sp.* bloom (Probyn et al., 2010) yielded a Chl *a* concentration of only 13 mg.m^{-3}, but the spectra are unusually bright, primarily due to the heightened scattering of the small cells (the Equivalent Spherical Diameter is approximately 2 μm). The *Alexandrium catenella* bloom, with a cell count of 9.8 $\times$ 10^6 cells per litre (Bernard et al., 2009), reached a Chl *a* concentration of 309 mg.m^{-3} but the spectrum is depressed as the ESD of these cells is very large - about 30 μm. In between, *Prorocentrum triestinum* of 14 and 38 mg.m^{-3} are shown from samples from the same bloom event, with the same D_{eff} of approximately 15 μm. While these 'extreme Case 1' measurements will reflect some variability in $a_{gd}(\lambda)$ and $b_{bnap}(\lambda)$ (notably in the *A. anophageffferens* example, which likely includes significant b_{bnap}), the proportional contribution of phytoplankton to the total IOPs depend primarily on both biomass and effective diameter.

It should be noted that phytoplankton IOPs result from the interaction, optically, of all of the various cellular properties (size, Chl *a* density, surface area etc.) and the numerical abundance of the cells. The total Chl *a* concentration of a sample is approximately proportional to the biovolume, but not necessarily to the cell abundance. This is illustrated well by the bloom examples above - the *A. catenella* bloom reached a Chl *a* concentration of 309 mg.m^{-3} at a cell count of 9.8 $\times$ 10^6 per litre, while the *Aureococcus sp.* bloom had a count of 6 $\times$ 10^8 cells per litre - two orders of magnitude higher - but only reached a Chl *a* concentration of 13 mg.m^{-3}. The D_{eff} parameter (Bernard et al., 2007) is defined as the assemblage volume divided by the total surface area, therefore implicitly accommodating the effects of both the abundance of cells and the pigment concentration (as it scales to the biovolume).

4.3.2 Proportional contribution of phytoplankton to bulk IOPs, and hence AOPs

Given the observation that R_{rs} is to first order, proportional to b_b/a, it follows that the phytoplankton contribution to a hypothetical R_{rs} without non-algal in-water constituents, would be proportional to $b_{b\phi}/a_\phi$. This 'net' optical contribution

of phytoplankton to the water-leaving signal is a way of quantifying the relative contribution of phytoplankton to the IOP budget, and determining the proportional contribution of the phytoplankton-driven signal to the total.

Being able to identify the spectral regions sensitive to changes in phytoplankton assemblage (focusing on those due to change in assemblage D_{eff}) is valuable, especially to identify spectral regions which might be sufficiently independent from the ambiguity introduced by other in-water constituents to allow the quantification of the phytoplankton signal with confidence, even where these other constituents are not well characterised.

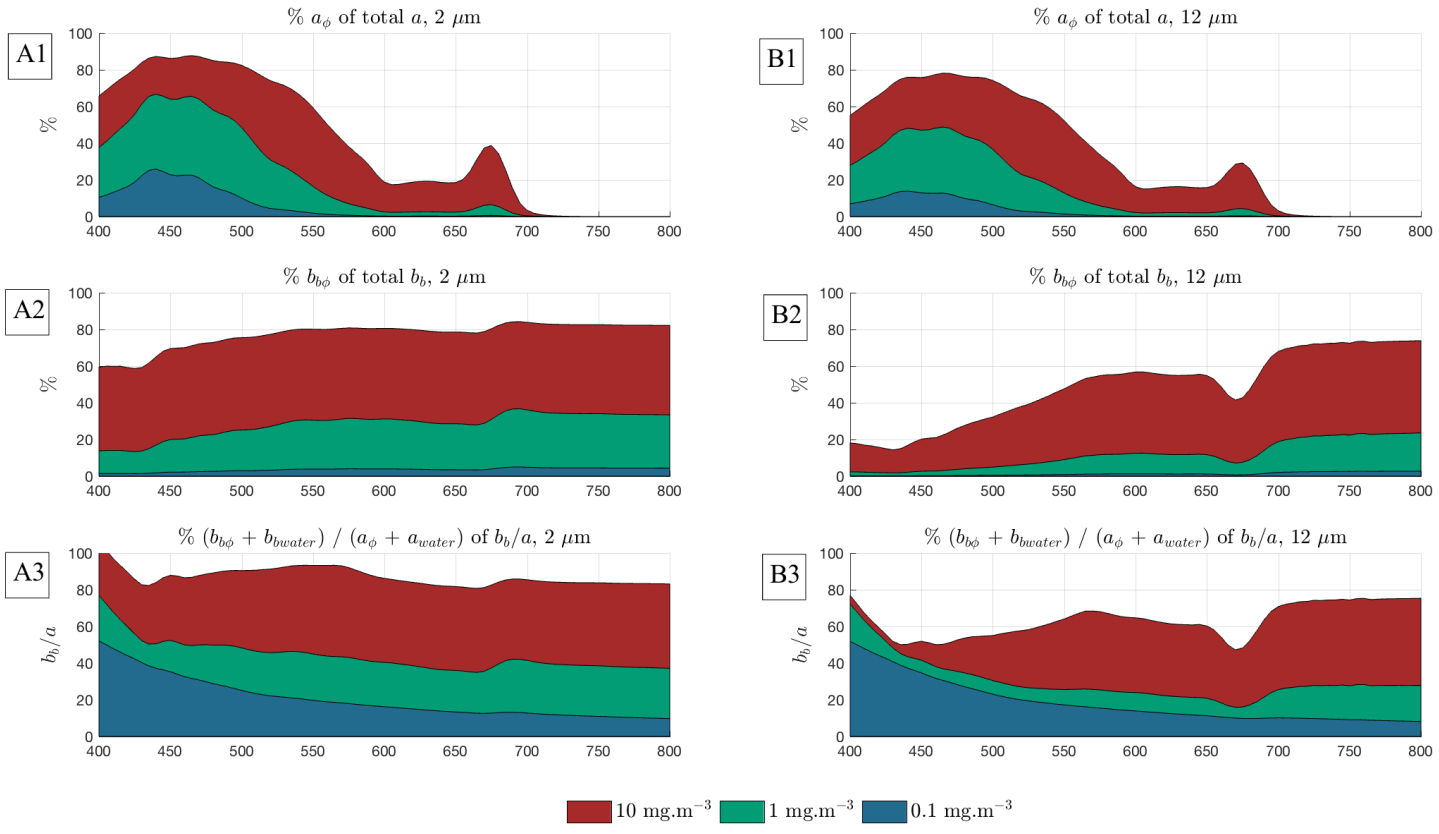

Figure 4.2: Percentage contributions of phytoplankton to total IOPs (including water), and b_b/a with $a_{gd}(400) = 0.07 * [Chl_a]^{0.75}$, and $b_{bnap}(550) = 0.005$ m^{-1}. This demonstrates the variable phytoplankton IOP contribution for generalised Case 1 waters as assemblage D_{eff} and biomass change.

The contribution of phytoplankton to the total IOPs in terms of absorption and backscatter is shown in Fig. 4.2, for increasing Chl *a*, and for generalised, theoretical Chl *a*-carotenoid eukaryote assemblages of D_{eff} of 2 and 12 μm. The total IOPs include those of water itself and of the non-algal constituents; $a_{gd}(400)$ is accounted for as $0.07*[Chl_a]^{0.75}$ m^{-1}, and $b_{bnap}(550)$ is held constant at 0.005 m^{-1}, with spectral character as described in Lain et al. (2014).

A 50% contribution to the total backscatter is reached well under a biomass of 10 mg.m^{-3} at a D_{eff} of 2 μm (red shading, Fig. 2.2 A2), but at 12 μm even the 10 mg.m^{-3} example only reaches a 50% contribution in certain spectral regions (B2). It is acknowledged that because the model is controlling all IOP inputs, natural variability (particularly that of the non-algal components) is not addressed here. The absolute proportions depend entirely on the non-algal IOPs, and this example is simply illustrative: the aim here is to show the relative increases and decreases in the phytoplankton proportional contribution as biomass and D_{eff} vary, and highlight some of the spectral regions where these changes are most evident.

For a given D_{eff}, the $b_{b\phi}/a_{\phi}$ will be constant for any concentration of Chl *a*, but the contribution of the phytoplankton IOPs to the total, will vary. Plots A3 and B3 of Fig. 4.2 compare the % contribution of $(b_{b\phi} + b_{bwater})/(a_{\phi} + a_{water})$ to the value of the total b_b/a for the various water types shown above. Water is included with the constituent IOPs to allow a more intuitive interpretation of the results. These plots show very clearly how little of the signal in the blue is due to phytoplankton at very low biomass. The point of interest in these plots is that the dominance of the phytoplankton signal (i.e. 50% of the total), is reached at relatively low biomass in the 2 μm assemblage, that is, at about 1 mg.m^{-3}, in contrast to the larger D_{eff} at this biomass. The spectral regions of maximum proportional phytoplankton signal are the ones which hold potential for detecting PFT changes from an in-water perspective, as these represent the regions of the largest phytoplankton-related signal variability as the assemblage changes.

The EAP model additionally allows close inspection of how the combined phytoplankton IOP parameter $b_{b\phi}/a_{\phi}$ contributes to the bulk water-leaving reflectance, and how this contribution varies with the total IOP budget. The EAP phytoplank-

ton IOPs are used with Hydrolight to calculate a full radiative transfer solution resulting in a new theoretical quantity, $R_{rs}\phi$. This quantity is introduced here as an approximate quantification of the phytoplankton contribution to the bulk R_{rs}, in order to more intuitively understand the relative optical contributions in terms of remote sensing. $R_{rs}\phi$ is the calculation of reflectance with only water and phytoplankton IOPs. It does not, as noted in Chapter 2, account for any optical interaction between the phytoplankton and other in-water constituents likely to be present in natural waters, such as CDOM or detrital and mineral particles. These interactions are assumed to be secondary to the contribution of phytoplankton, but have not been quantified. It is anticipated that trans-spectral effects are most likely to suffer from this type of subtractive approach, but a full photon tracing model (such as a Monte Carlo model) would be needed to ascertain this. By modelling the phytoplankton contribution to the water-leaving signal we can assess the availability of signal for PFT retrieval in light of the proportionality study shown above.

The resulting contribution of phytoplankton to the total R_{rs} is shown in Fig. 4.3, for typical Case 1 waters. As seen in the previous figure, as the phytoplankton contribution to the IOPs increases (i.e. generally, as biomass increases), the impact of the other constituents is proportionally less in the R_{rs}. This is observable in Fig. 4.3 to a greater degree in the R_{rs} with the smaller D_{eff} of 2 μm as compared with the larger of 12 μm - the higher level of phytoplankton backscatter contributing to brighter R_{rs} which is less sensitive to the addition of scattering from other sources. The 12 μm D_{eff} R_{rs} are not as bright due to less scatter by larger phytoplankton even at elevated biomass, and other scattering sources consequently have a greater potential to influence bulk R_{rs}. Also note that small proportional contributions of phytoplankton to the total IOPs in Fig. 4.2 translate into large differences between R_{rs} and $R_{rs}\phi$ in Fig. 4.3, revealing the sensitivity of these spectral region to variability in non-algal contributions.

For each D_{eff}, it is evident that the phytoplankton percentage contribution to the bulk R_{rs} increases with biomass. But it can be seen that there is a dependency on D_{eff} which, when considered in the context of transitioning assemblages, is not straightforward. This observation indicates a requirement to go beyond the Case

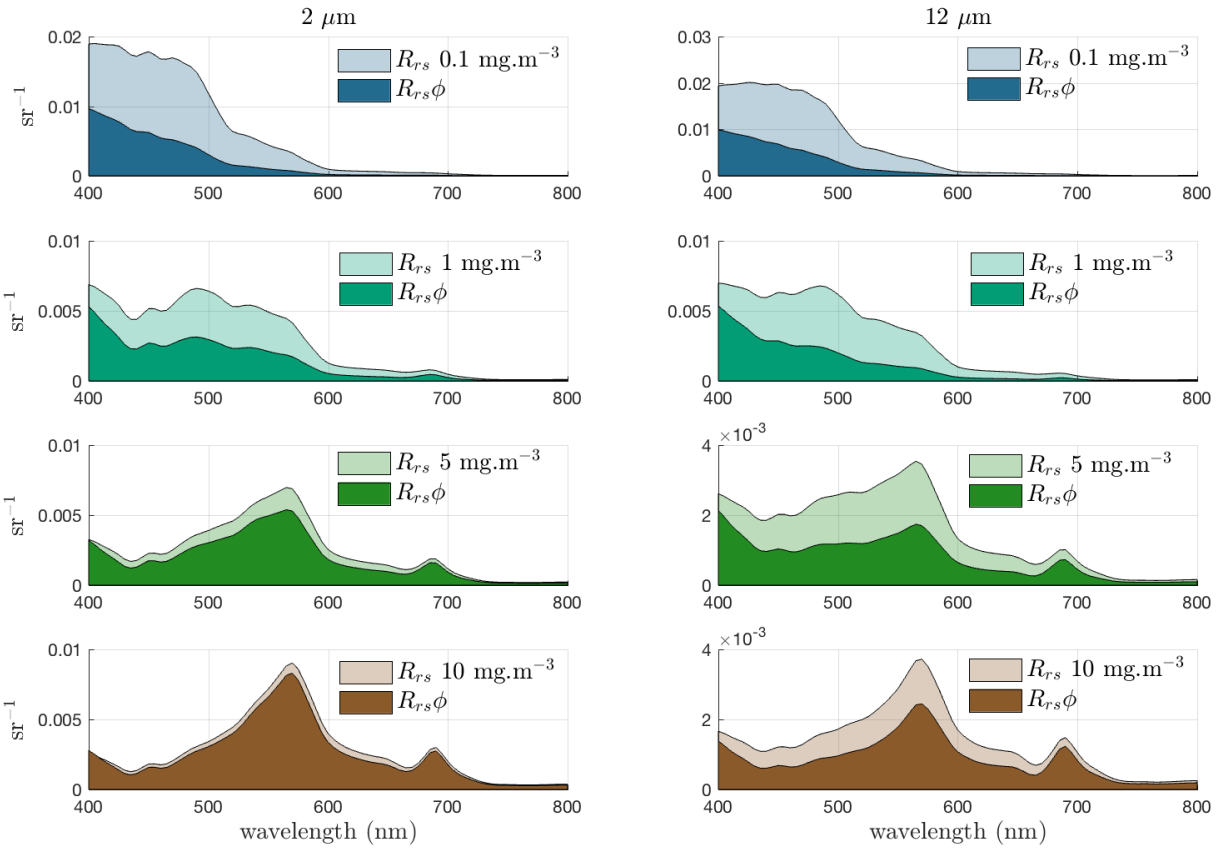

Figure 4.3: Relative contribution of phytoplankton to total R_{rs} (with $a_{gd}(400) = 0.07{*}[Chl_a]^{0.75}$, and $b_{bnap}(550) = 0.005$ m^{-1}) for increasing biomass with $D_{eff} = 2$ and 12 μm.

1/Case 2 water type distinction for PFT signal analysis and applications. When it comes to retrieving information about the phytoplankton IOPs, their proportional contribution to the bulk IOPs should be considered. Due to the variable contributions of phytoplankton to total absorption and backscatter, the contribution of the combined IOP parameter $b_{b\phi}/a_{\phi}$ to the total b_b/a appears useful, as it allows non-covariance of the non-algal constituents to be addressed.

4.3.3 Satellite considerations

Additional layers of complexity are to be considered when retrieving water-leaving signal from satellite TOA radiometric data, and then inverting it in the attempt to retrieve PFT information from the bulk signal (Evers-King et al., 2014). Satellite water-leaving radiance (or remote sensing reflectance) retrievals display more uncertainty in the blue (Antoine et al., 2008; Mélin et al., 2016), due to radiometric noise in the blue channel, larger Top Of Atmosphere (TOA) signal due to Rayleigh scattering, and high sensitivity to noise in the NIR because the aerosol scattering contribution to TOA signal is estimated from the NIR and extrapolated towards the shorter wavelengths (Mélin et al., 2016). Average measurement uncertainty in satellite R_{rs} due to these effects is at its greatest at the shorter wavelengths, estimated at $0.7 - 0.9 \times 10^{-3} sr^{-1}$ at 412 nm, decreasing to $0.05 - 0.1 \times 10^{-3} sr^{-1}$ at 670 nm (Mélin et al., 2016). Detecting small changes in R_{rs} to infer information about PFTs must be done in the context of both uncertainties in the R_{rs} quantity, and the accompanying effects of non-algal absorption and scatter.

This work does not directly address ambiguity in terms of inversion of the water-leaving signal but rather, ambiguity in the causality of the signal. The magnitude of changes to the water-leaving signal as the in-water constituents vary is the first question to address, when ultimately aiming to determine whether there may be enough radiometric signal at TOA to even detect the change. In this chapter a threshold *in situ* measurement resolution of 1×10^{-4} sr^{-1} (Chami et al., 2006a) is taken as an indication of sensitivity to detecting change in R_{rs} by direct measurement. Given an average estimated uncertainty in satellite R_{rs} of $\pm$ 0.6 $\times$ 10^{-3} sr^{-1} across the spectrum (Gordon, 1997), here a conservative 1×10^{-3} sr^{-1} is used to indicate a potentially detectable change in water-leaving signal from satellite. These thresholds are not definitive and are used purely for the purpose of contextualising the discussion.

4.4 Locating the PFT signal

4.4.1 Separating the effects of biomass from the effects of PFT (D_{eff}) change

Generally speaking for a constant assemblage (i.e. unchanging PFTs and size distribution), as biomass increases and the spectral character of backscatter changes, reflectances become brighter in the green and red, and are reduced in the blue. This forms the basis of many satellite Chl a estimating algorithms (O'Reilly et al., 1998), using narrow wavebands as indicated in Fig. 4.4 (those of the Ocean and Land Colour Instrument OLCI, on the Sentinel-3 satellite, are shown). For clarity and following determined ranges for abundance (Agusti et al., 1987), $R_{rs}\phi$ are shown for Chl a = 0.1 and 1 mg.m^{-3} with D_{eff} 2 - 8 and 8 - 20 μm (A), and Chl a = 1 and 5 mg.m^{-3} with with D_{eff} 2 - 8 and 8 - 20 μm (B). The larger size range would not be generally appropriate for a low biomass of 0.1 mg.m^{-3}, but is shown to illustrate how the range and spectral location of size effects changes with biomass.

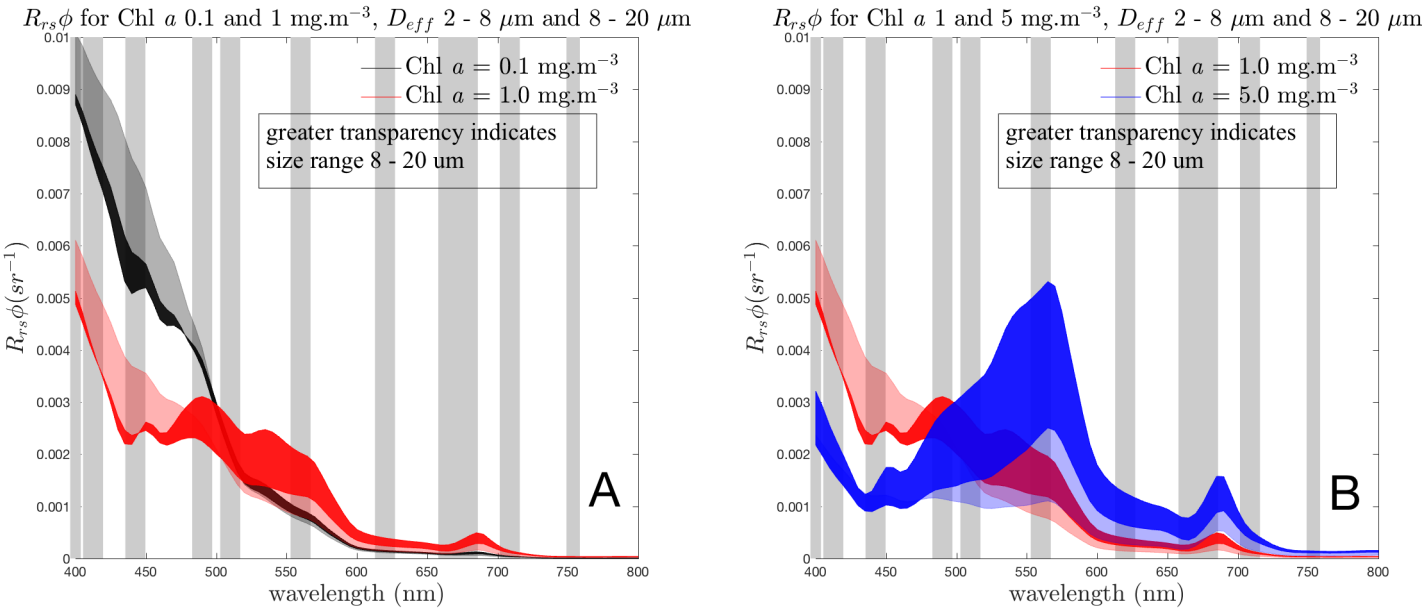

Figure 4.4: Modelled R_{rs} in the absence of additional optically significant in-water constituents overlaying OLCI wavebands, for Chl a = 0.1 and 1 mg.m^{-3} with D_{eff} 2 - 8 and 8 - 20 μm (A), and Chl a = 1 and 5 mg.m^{-3} with D_{eff} 2 - 8 and 8 - 20 μm (B).

Wavelength (or waveband) ratios are useful as a simple first order representation of spectral shape, and are used by most ocean colour algorithms. Fig. 4.5 shows, on a log scale, the full spectral ratios with λ:665 (A) and λ:560 nm (B), chosen to correspond with OLCI wavebands, for four Chl a values between 0.1 and 10 mg.m^{-3}. These ratios show virtually no size sensitivity at 0.1 mg.m^{-3}. At 1 mg.m^{-3} a sensitivity emerges at small D_{eff} in the blue, and this persists as biomass increases although the magnitude of the change in ratio decreases: So, while the causal signal is there, it becomes less detectable due to increased phytoplankton absorption and a_{gd} (which in this case is proportional to biomass, as indicated in the figure caption). It should be noted also that any variability in a_{gd} in the blue will have an effect on the radiometric measurement here and so this spectral region of size signal in the ratios will be sensitive to a_{gd} to at least some degree. The extent of this sensitivity will be investigated further in the next section. As the biomass reaches 5 mg.m^{-3} a signal emerges at around 570 nm, strengthening with increased biomass but decreasing with larger D_{eff}. This signal (i.e. the change at 570 nm with increasing D_{eff}) is more apparent in the λ:665 nm ratio, and is mostly lost in the λ:560 nm ratio.

Fig. 5 in Evers-King et al. (2014) shows that for OC4 maximum band reflectance ratios, higher ratios are associated with larger D_{eff} (this is consistent with this Fig. 4.5), and also provides example spectral ranges with similar R_{rs} ratios but representing vastly different water types. In Fig. 4.5, the range of λ:665 nm ratio values is much larger as the radiometric magnitude of the ratio denominator at 665 nm is small, so the absolute magnitudes of this kind of ratio analysis should be interpreted with caution. It is the rate of change across D_{eff} that reveals the size information encapsulated in the spectral shape.

The complex optical interactions of D_{eff} and biomass, and the question of whether they can be adequately separated into a useable PFT signal from a background environment of further non-algal optical complexity, is best addressed by investigating specific ecological events of interest to the remote sensing community. The following case studies give an indication of which types of in-water ecological events may be optically observable.

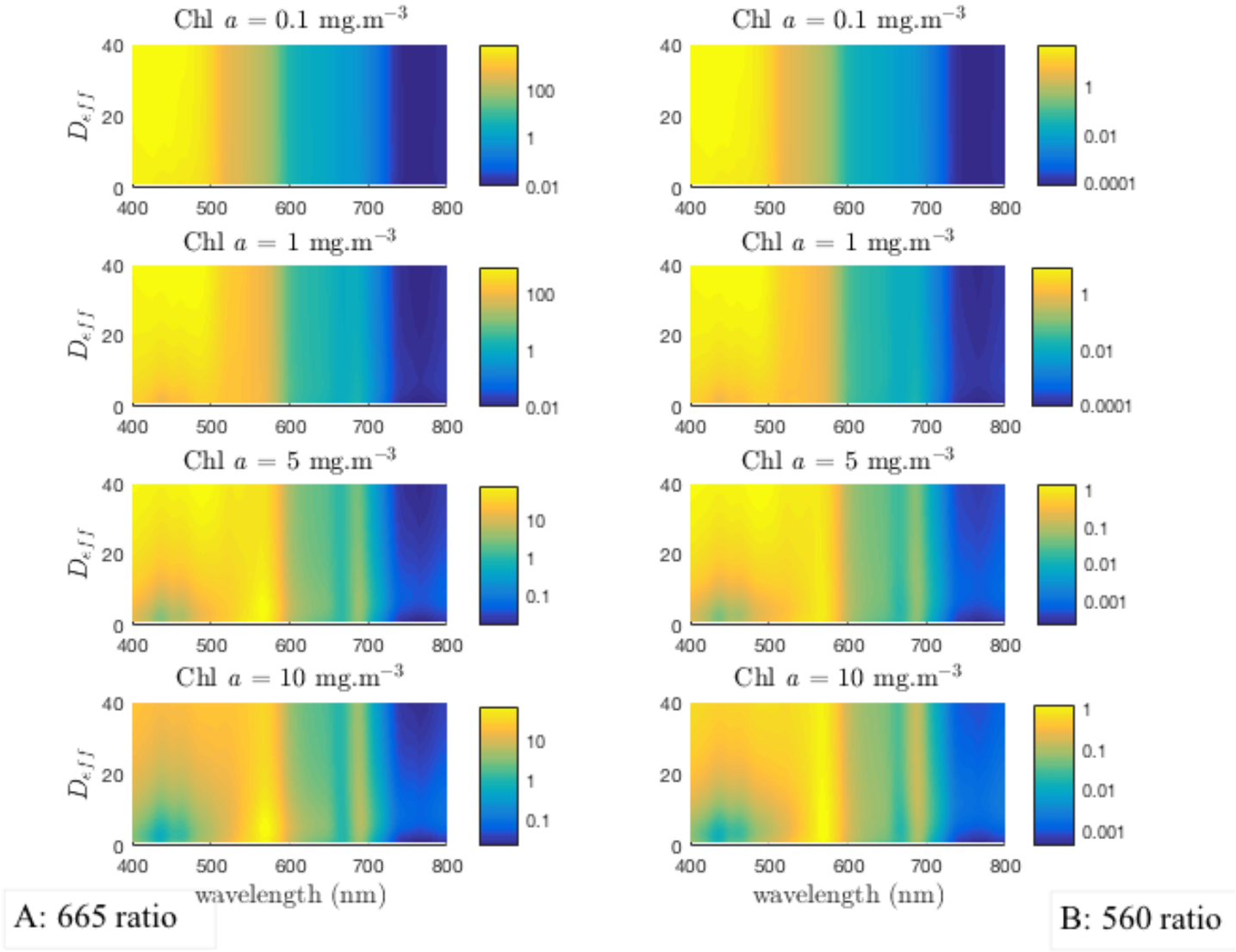

Figure 4.5: Full spectral ratios to 665 (left) and 560 (right) nm, shown on a log scale. Non-algal contributions are modelled with $a_{gd}(400) = 0.07 * [Chl_a]^{0.75}$, and $b_{bnap}(550) = 0.005$ m^{-1}. Note the colour bar range increases by an order of magnitude for the 665 ratios, and also for the lower biomass panels in both cases.

Case Study 1: Size effects in the Southern Ocean

As shown in the previous chapters, where the water-leaving signal is phytoplankton-dominated (e.g. in the Benguela system), it is quite reasonable to expect that some PFT information may be derived from the bulk signal. But the challenge for the ocean colour community is determining the PFT signal in low biomass oceanic conditions, for example in the Southern Ocean, where this case study is set.

Phytoplankton dynamics in the Southern Ocean are particularly important for their role in uptake of anthropogenic CO_2 (around half of all oceanic uptake), and hence carbon sequestration (Thomalla et al., 2011; Swart et al., 2012). Variability in phytoplankton ecology is directly linked to mineral and nutrient cycles: assemblages of large diatoms drive primary productivity and carbon export, while assemblages of small phytoplankton play a significant role in nutrient recycling although the net productivity is very low (Constable et al., 2014).

The third Southern Ocean Seasonal Cycle Experiment (SOSCEx III) undertaken on the SANAE 55 cruise (austral winter 2015) provides the phytoplankton size distribution and Chl *a* data for this experiment (Mtshali, 2016). Assemblage D_{eff} were calculated from Coulter Counter measurements, and Chl *a* determined by fluorometric analysis (Ryan-Keogh et al., 2017). The additional $a_{gd}(\lambda)$ and $b_{bnap}(\lambda)$ components for the R_{rs} in Fig. 4.6 were estimated guided by observations in (Del Castillo and Miller, 2011) and (Reynolds et al., 2001) respectively, noting that these are simply used to approximate the bulk R_{rs} in Fig. 4.6, and do not influence any of the other results below, as they are discussed in terms of likely variability rather than absolute magnitudes. EAP phytoplankton IOPs with generalised Chl *a*-carotenoid eukaryotic refractive indices were calculated according to the measured D_{eff} and Chl *a* concentrations, and were combined with these estimates and run through Hydrolight to produce the modelled R_{rs}.

Given that the refractive indices used to model the EAP IOPs for this example are from the generalised Chl *a*-carotenoid group suitable for diatom and dinoflagellate species, the likelihood of encountering *Phaeocystis sp.* in the Southern Ocean must be addressed. Given the oceanographic context, as the D_{eff} of 16 μm is reached, it can reasonably be assumed that the assemblage comprises

both diatoms and *Phaeocystis*. The main accessory pigment in *Phaeocystis* is 19-hexanolyoxyfucoxanthin, a derivative of fucoxanthin, a dominant light harvesting pigment in diatoms, and so it may be reasonable to model the intracellular absorption properties of individual cells with the generalised eukaryote refractive indices, but this species forms large floating colonies which result in quite different optical effects, and this cannot currently be addressed with the model. So while the likely presence of *Phaeocystis* is acknowledged, it is not explicitly catered for in the modelling. This does not affect the observations on identifying changes in D_{eff} in the discussion below.

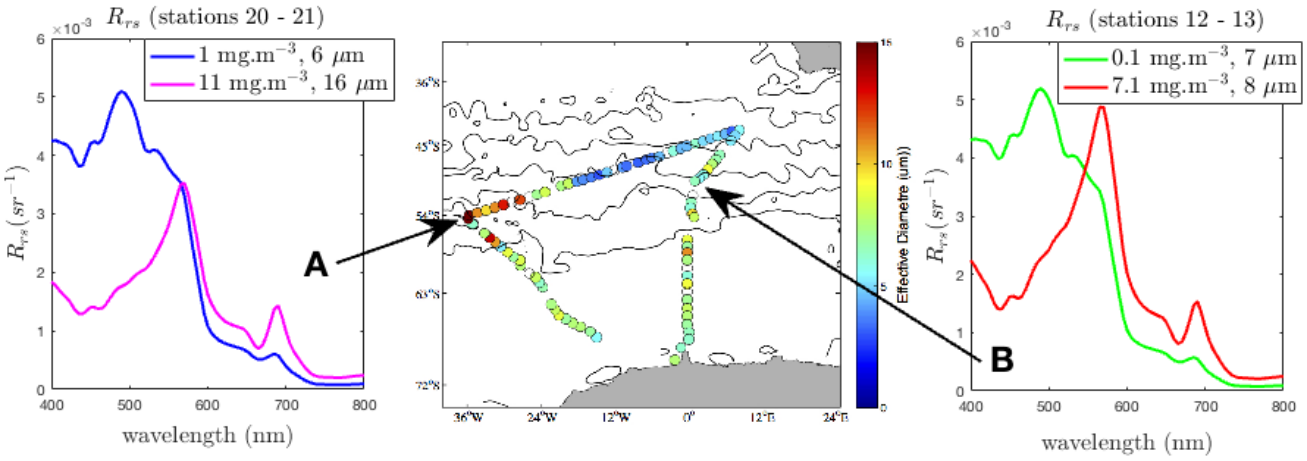

Figure 4.6: Modelled R_{rs} for stations 20, 21, 12 and 13 of SOSCEX III. The modelled bulk R_{rs} are calculated using EAP generalised Chl *a*-carotenoid refractive indices and measured Chl *a* concentrations for the phytoplankton component, and include estimated $a_{gd}(\lambda)$ and $b_{bnap}(\lambda)$ contributions appropriate for this region (Del Castillo and Miller, 2011; Reynolds et al., 2001). Stations 20 to 21 (A) represent a large change in both Chl *a* concentration and in D_{eff}. Stations 12 to 13 (B) represent a large change in Chl *a* concentration only. The centre panel shows the measured D_{eff} for the cruise track (starting at the ice shelf on the bottom right and continuing in an anticlockwise direction.) Effective diameter image courtesy of SANAE 55 Report (Mtshali, 2016).

In Fig. 4.6 attention is drawn to two distinct events which illustrate the inter-dependency of the size and biomass signals. Modelled R_{rs} are shown for selected adjacent stations (20 to 21 is marked A; 12 to 13 is marked B) where the nominal threshhold of change detectable by satellite is reached in the blue and green spectral regions, in other words, where a change in R_{rs} would be evident on a satellite image. Both examples display large changes in R_{rs}, but these are causally distinct: (A) represents a large change in Chl *a* concentration *and* in D_{eff}, while (B) represents a large change in Chl *a* concentration but a negligible change in D_{eff}.

Station 20 to 21 therefore represents a significant phytoplankton community shift, as large changes in both D_{eff} (from 6 to 16 μm) and Chl *a* concentration (from 1 to 11 mg.m^{-3}) were recorded. To isolate this change in phytoplankton signal, the differences in $R_{rs}\phi$ for an assemblage D_{eff} of 6 μm and an assemblage D_{eff} of 16 μm are presented in Fig. 4.7 (A) for the measured range of Chl *a* concentration. The spectral location of the most promising size-related signal for PFT retrieval is evidently dependent on biomass, and at low biomass it is positioned near 435 nm, while at higher biomass it is around 570 nm. As this is the phytoplankton-only signal, the question remains to what extent this signal is expressed in the bulk R_{rs}, when the optical impact of the non-algal constituents is also considered.

Working with the change in phytoplankton size signal identified at 435 nm, $a_{gd}(\lambda)$ is added at increasing concentrations to simulate a range of bulk R_{rs} at 435 nm in Fig. 4.7 (B), and $b_{bnap}(\lambda)$ is likewise added incrementally at 570 nm (Fig. 4.7 C). In these plots, horizontal gradients indicate R_{rs} sensitivity primarily to the constituent on the y axis, while vertical gradients indicate that the change in R_{rs} is driven by the biomass, and is not sensitive to variability on the y axis.

Fig. 4.7 (B) shows that the difference in bulk R_{rs} for the given δD_{eff} is only detectable at the satellite threshold level (shown in yellow) at low biomass under low $a_{gd}(\lambda)$ conditions. As biomass increases, increasing absorption by phytoplankton as well as by additional $a_{gd}(\lambda)$, reduces the magnitude of the water-leaving signal and renders any δD_{eff} information ambiguous. When additionally considering the brightening effect of $b_{bnap}(\lambda)$ in the blue (not quantified here), it can readily be perceived that the water-leaving signal is too complex at 435 nm to retrieve useful

size information.

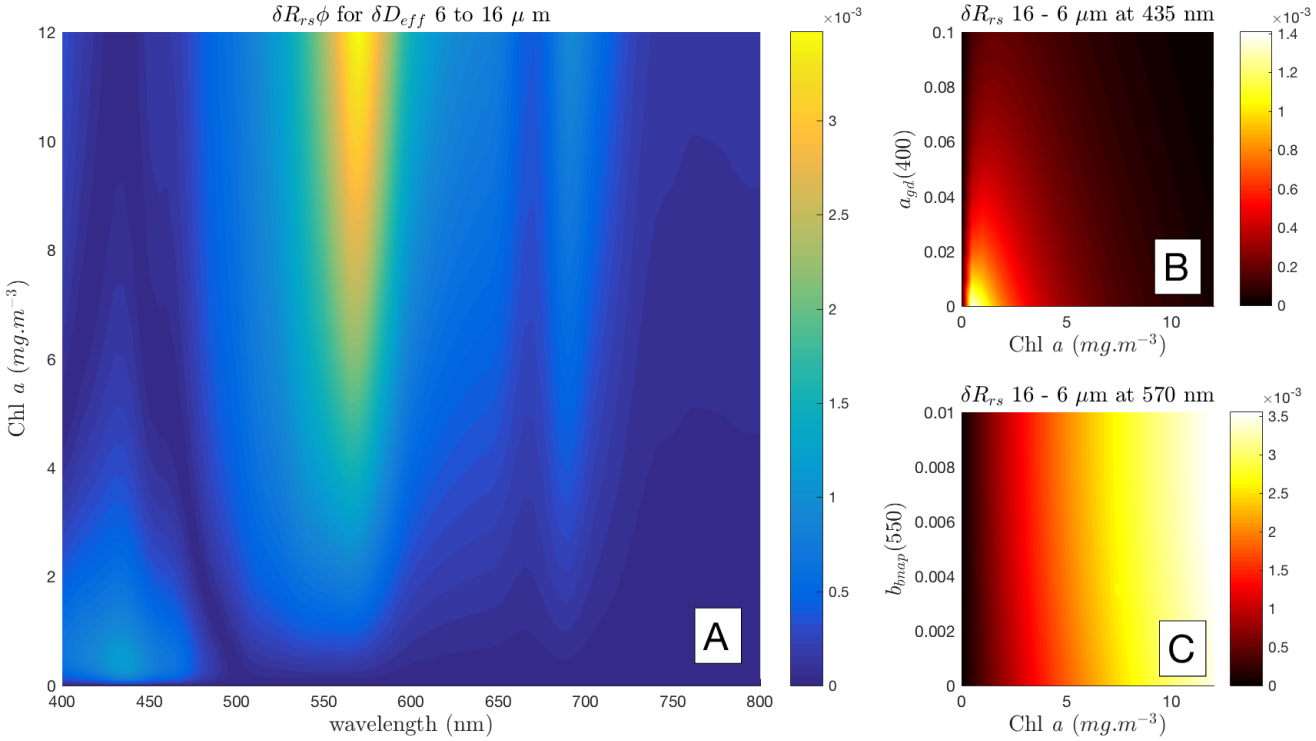

Figure 4.7: Southern Ocean stations 20 to 21: $\delta R_{rs}\phi$ is shown for δD_{eff} of 6 to 16 μm (A). The effect of $a_{gd}(\lambda)$ at 435 nm is shown in (B), and $b_{bnap}(\lambda)$ at 570 nm in (C). The units of the colour bars are sr^{-1}.

In Fig. 4.7 (C), the relationship with $b_{bnap}(\lambda)$ at 570 nm is more straightforward. Change in R_{rs} due to δD_{eff} is detectable in the bulk R_{rs} at the threshold (in red) from about 2.5 $\mathrm{mg.m}^{-3}$ upwards regardless of the $b_{bnap}(\lambda)$ contribution, at least for oceanic Case 1 type conditions. The magnitude of this signal is almost entirely biomass driven. This is in line with the observation made by (Brown et al., 2008) that the MODIS wavebands at 531 and 551 nm are good indicators of backscatter anomalies because their magnitude is proportional to the addition or removal of particulate backscattering, and the longer wavelength band at 551 nm is less affected by variability in both $a_{gd}(\lambda)$ and phytoplankton absorption (Kostadinov et al., 2009).

It should be appreciated, though, that $R_{rs}\phi$ in these figures is representing the change in R_{rs} due to size *at* a particular biomass (i.e. biomass is constant while assemblage characteristics vary). Figure 4.8 simulates a transition from 6 to 16 D_{eff}

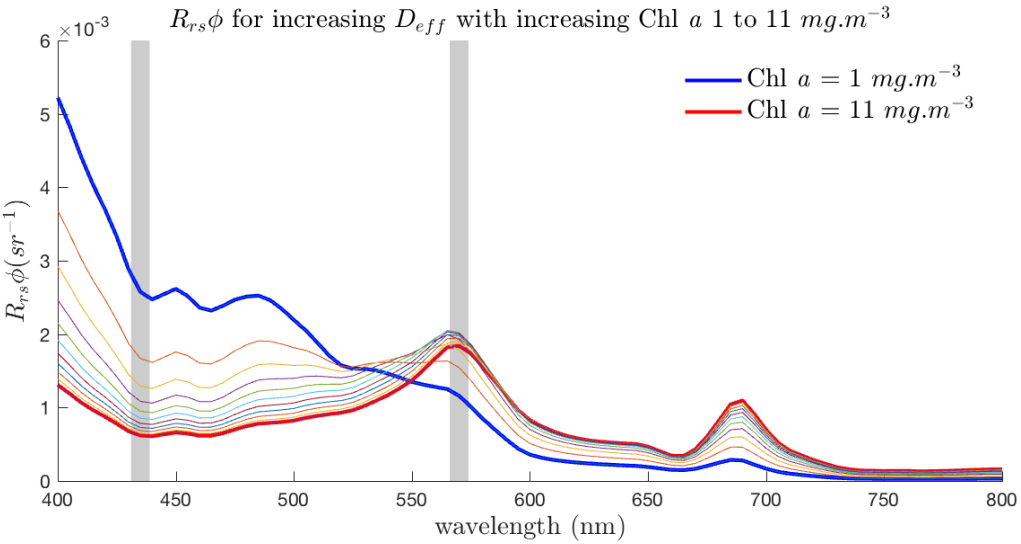

Figure 4.8: A simulated transition from 6 to 16 D_{eff} with biomass 1 to 11 mg.m^{-3}. Intermediate values of D_{eff} and Chl a are simply linearly interpolated. The lines highlight 435 nm and 570 nm, regions of maximum size signal, which are (at 435 nm) and are not (at 570 nm) sensitive to the effects of additional optical consituents.

with biomass 1 to 11 mg.m^{-3}, where the intermediate values of both D_{eff} and Chl a are simply linearly interpolated. The vertical lines highlight 435 and 570 nm which were identified in Fig. 4.7 (A) as being the spectral regions of greatest size-driven signal. In Fig. 4.8, while biomass and size effects combine to form large changes in $R_{rs}\phi$ in the blue, it is the smaller signal around 570 nm that contains the most size-driven change as it is not affected by biomass to the same degree. Figure 4.7 (B) and (C) show that the signal at 435 nm is sensitive to the effects of variable a_{gd}, while the phytoplankton signal at 570 nm remains robust against variability in the non-algal optical contributions.

By contrast, stations 12 to 13 exhibit a large change in R_{rs} (seen first in Fig. 4.7 (B); shown again in Fig. 4.9 A), with an increase in Chl a from 0.9 to 7.1 mg.m^{-3} but only a very small change in D_{eff} from 7 to 8 μm. This is likely, given the location in the lee of the South Sandwich Islands, to reflect a diatom bloom associated with island wake effects, due to fertilisation by terrestrial iron (Boyd and Ellwood, 2010). Tracing the signal due to this change in D_{eff} across all Chl a concentrations in this range (Fig. 4.9 B) show that there is a size related signal between 550 and 600 nm but it is of an order of magnitude less than in the previous example, and so does

not show potential for detection by satellite radiometry. This is illustrated further in the lower panel C, showing the location of this signal, but that it is almost all attributable to biomass - as shown by the $R_{rs}\phi$ representing D_{eff} 7 at 7.1 mg.m^{-3} i.e. what the higher biomass R_{rs} would look like without the increase in effective diameter as the assemblage changes. It can be seen quite clearly from these spectra that a difference in the blue due only to this δD_{eff}, with any variability $a_{gd}(\lambda)$, would not be detectable by any means.

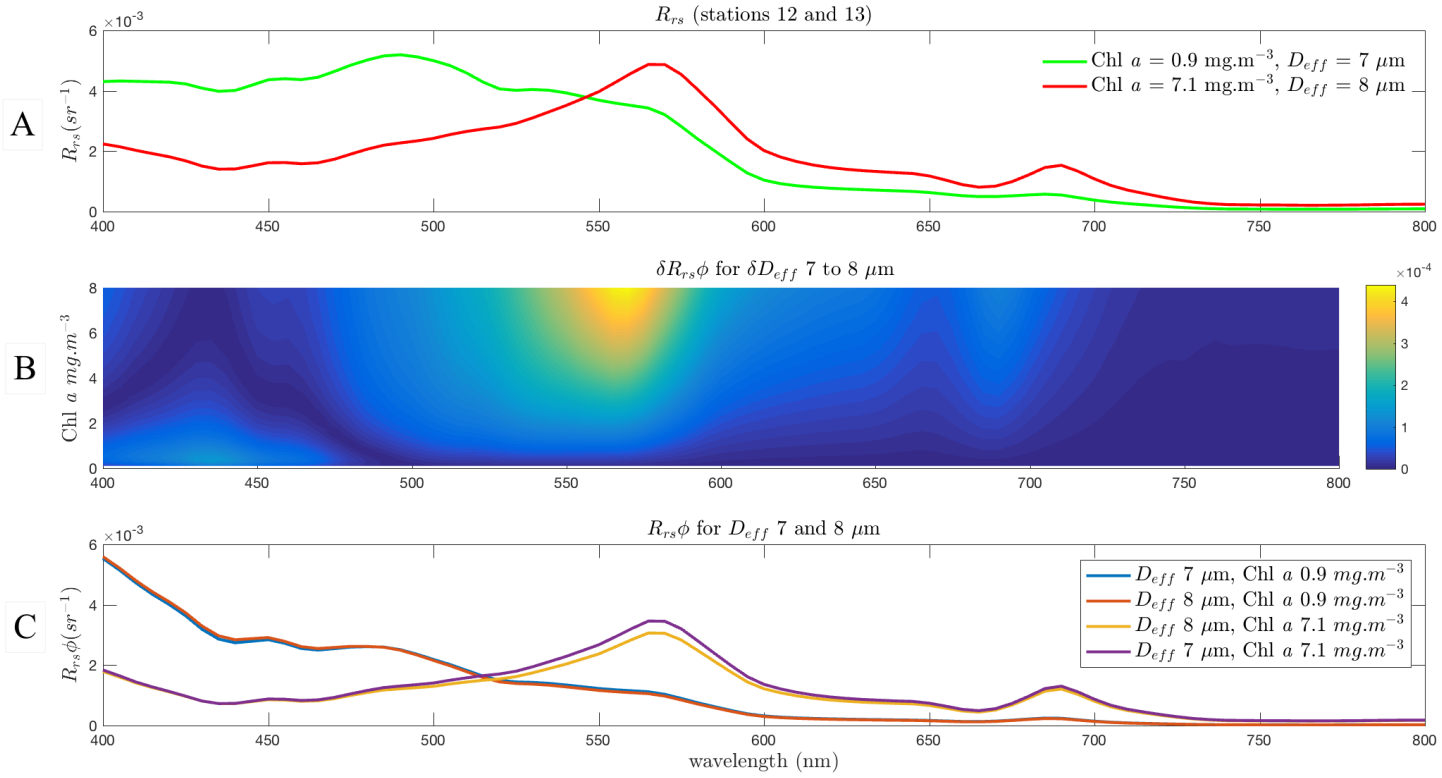

Figure 4.9: Modelled R_{rs} for Stations 12 and 13 (A), with EAP eukaryote phytoplankton IOPs, and $a_{gd}(\lambda)$ and $b_{bnap}(\lambda)$ components estimated guided by observations in (Del Castillo and Miller, 2011) and (Reynolds et al., 2001) respectively. (B) shows $\delta R_{rs}\phi$ for this large change in Chl a concentration (1 to 7 mg.m^{-3}) but a small δD_{eff} of 7 - 8 μm. The unit of the colour bar is sr^{-1}. Note that the results are one order of magnitude less than in the previous example. (C) shows the negligible effect on $R_{rs}\phi$ of a change in D_{eff} from 7 to 8 μm at the measured Chl a concentrations.

It should be noted that the spectral locations of maximum δD_{eff} features are a direct consequence of the spectral nature of the IOPs used in the modelling, and that both of these examples use the same Chl a-carotenoid refractive indices to

generate the phytoplankton IOPs. The spectral character of the optical effects of assemblage changes will differ as phytoplankton IOPs are varied to accommodate pigment differences, for example. A slight migration in the exact location of the maximum available δD_{eff} signal is observable with different ranges of D_{eff}, although within the Chl *a*-carotenoid group it remains between 550 and 600 nm for any difference in D_{eff} between 1 and 40 μm.

Summary of observations on detecting δD_{eff}

The size of $\delta R_{rs}\phi$ is proportional to the magnitude of the δD_{eff}, but in the blue this is a second order effect to a change in biomass, whose effect is much greater. For a given δD_{eff} of 6 - 16 μm, a detectable size signal appears around 570 nm from a biomass of approximately 2 mg.m^{-3}, and this is affected by biomass to a lesser degree. At low biomass (with Chl *a* less than 2 mg.m^{-3}) there is a distinct size-related signal at 435 nm, but this is not useful as it is very sensitive to the effects of $a_{gd}(\lambda)$ and $b_{bnap}(\lambda)$, which renders the bulk signal ambiguous as to its origin. As biomass increases, there is an increasingly prominent size-related signal at around 570 nm, which is shown to be insensitive to reasonable variability in $b_{bnap}(\lambda)$.

4.4.2 Addressing pigment variability

The assemblages modelled in the above examples address optical changes due only to biomass (i.e. concentration of Chl *a* pigment) and size (assemblage D_{eff}), as the same set of generalised Chl *a*-carotenoid refractive indices is used for all phytoplankton particles represented. But this approach addresses only a small subset of important changes in phytoplankton assemblage type, and in the presence of variability in dominant accessory pigments, the EAP model can be set to incorporate different refractive indices as appropriate for phytoplankton displaying accessory pigments other than carotenoids.

Case Study 2a: High biomass Benguela example

To illustrate the effects of pigment variability, this case study simulates a transition from a high biomass *Myrionecta rubra*-dominated assemblage, to a high biomass peridinin (carotenoid)-containing dinoflagellate-dominated assemblage. It should be made clear that this is not intended to represent a likely ecological succession (except possibly a Lagrangian one, if a dinoflagellate bloom is advected into a previously *M. rubra*-dominated region), but rather to test what biomass and pigment differences are required for the detection of distinct optical conditions, particularly in the context of remote sensing.

M. rubra is a fascinating but troublesome ciliate species, and enjoys an endosymbiontic relationship with cryptophytes containing the diagnostic pigment phycoerythrin (Gustafson Jr et al., 2000), and so "borrows" their characteristic red colour. *M. rubra* blooms can reach extraordinary biomass, resulting in darkly pigmented 'red tide' waters which have negative impacts both ecologically (depletion of nutrients, and the potential for anoxia as the bloom dies), as well as on the recreational use of coastal waters (Gustafson Jr et al., 2000).

Both assemblages are modelled here (Fig. 4.10) with D_{eff} of 12 μm, so the resulting optical changes as the assemblage changes from *M. rubra*-dominated to dinoflagellate-dominated are all due to differences in pigmentation, for any given Chl *a* concentration. From the log-scale R_{rs} it is evident that the pigment-related differences in R_{rs} become larger as biomass increases. In the very high biomass

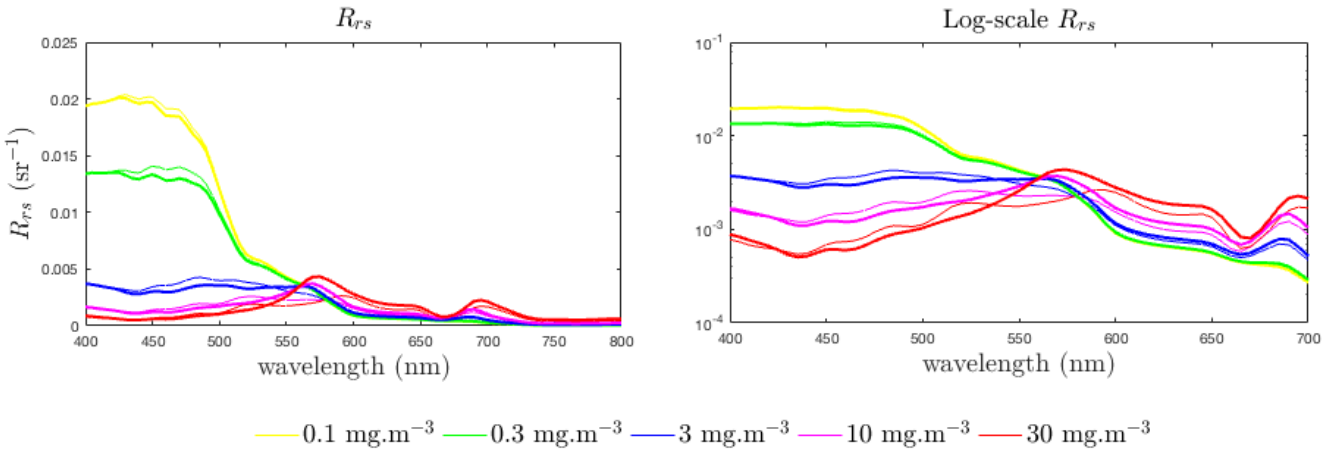

Figure 4.10: Benguela-like pigment-based experiment: Modelled R_{rs} shown for Chl a-carotenoid pigmented assemblages (thick lines) and a phycoerythrin containing assemblages (thin lines) for identical Chl a concentrations, at 0.1, 0.3, 3, 10 and 30 mg.m^{-3}. There is no change in D_{eff}, both are 12 μm. The non-algal optical consituents are modelled with $a_{gd}(400) = 0.07 * [Chl_a]^{0.75}$, and $b_{bnap}(550) = 0.005$ m^{-1}.

blooms ($\geq$ 30 mg.m^{-3}) typical of the Benguela system, it is known that *M. Rubrum* - containing assemblages are identifiable from MERIS satellite imagery (Bernard et al., 2014) due to the effects of the diagnostic phycoerythrin peak (at 565 nm) appearing in the 560:520 nm band ratio.

If an analagous study to the sensitivity of the maximum $\delta R_{rs}\phi$ signal to non-algal constituents is made at 570 nm for high biomass (Fig. 4.11), the sensitivity to size differs from previous examples in that it is largely driven by variability in $b_{bnap}(\lambda)$, as shown by the predominantly horizontal colouration in Fig. 4.12 (B). This is affected by the range of $b_{bnap}(\lambda)$, which is much larger here than in the lower biomass Southern Ocean case studies. If the $b_{bnap}(\lambda)$ remains fairly constant, the magnitude of the change in water-leaving signal is still sufficient to be detectable.

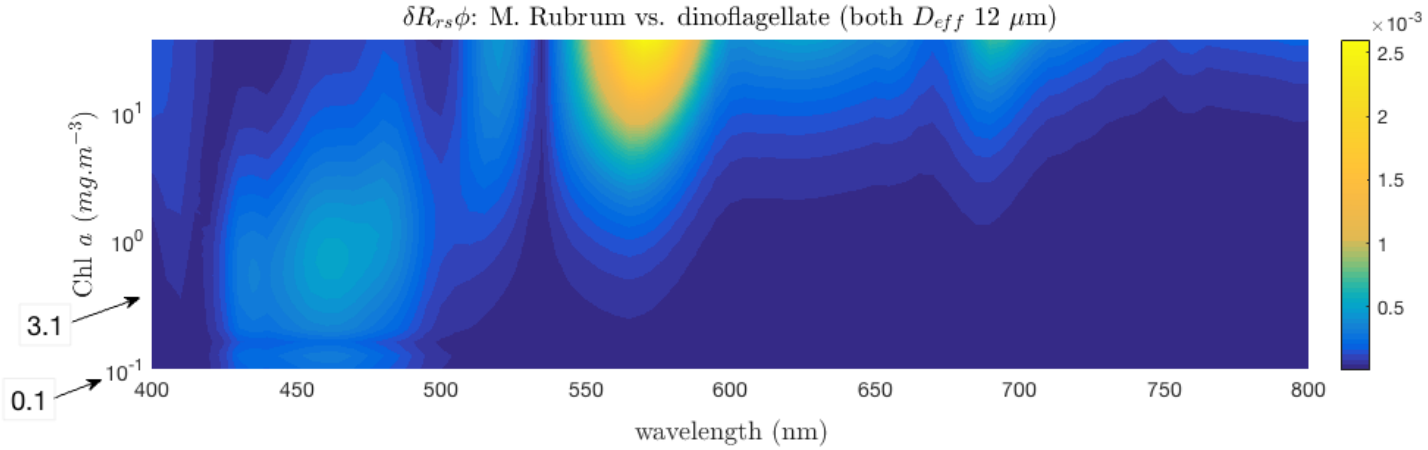

Figure 4.11: Benguela-like pigment-based experiment: $\delta R_{rs}\phi$ shown for a gradual change from *M. rubra*-dominated conditions to dinoflagellate-dominated, with Chl a concentrations from 10 to 50 mg.m^{-3}). There is no change in D_{eff}.

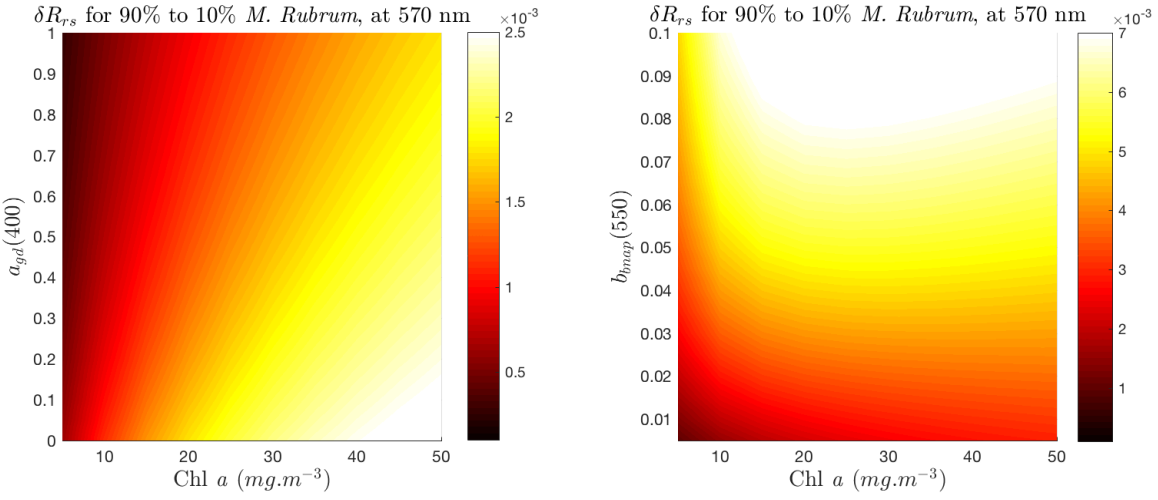

Figure 4.12: Benguela-like pigment-based experiment: δR_{rs} shown for a demonstration dinoflagellate to *M. rubra* succession under varying $a_{gd}(\lambda)$ and $b_{bnap}(\lambda)$ conditions, at the spectral location of maximum $\delta R_{rs}\phi$ (570 nm). The differences shown are for assemblages modelled with a combination of phytoplankton IOPs: the transition is from 90% *M. Rubrum* and 10% generalised eukaryotes, to 10% *M. Rubrum* and 90% eukaryote.

Case Study 2b: Low biomass Southern Ocean example

In the Southern Ocean, the spring bloom is one of the most important ecological events as it signals the change from *Synechococcus sp.*-dominated very low biomass, and low productivity, to diatom-dominated waters with high productivity and implications for carbon export and sequestration (Constable et al., 2014). It is also an interesting case study in terms of the EAP model as it presents the opportunity to identify optical changes which are pigment-driven as well as by D_{eff}. For this experiment, *Synechococcus sp.* IOPs were modelled using the refractive indices measured from *Myrionecta rubra* (or *Mesodinium rubrum*) in the Benguela - which shares with *Synechococcus sp.* the diagnostic pigment phycoerythrin (Bricaud et al., 1988), while being a much larger cell. Following measurements by Bricaud et al. (1988), a c_i of 2.2x10^6 kg.m^{-3} was used, with an assemblage effective diameter of 1 μm, and the resulting phytoplankton specific absorption spectrum was compared with those measured by Morel et al. (1993) to ensure consistency.

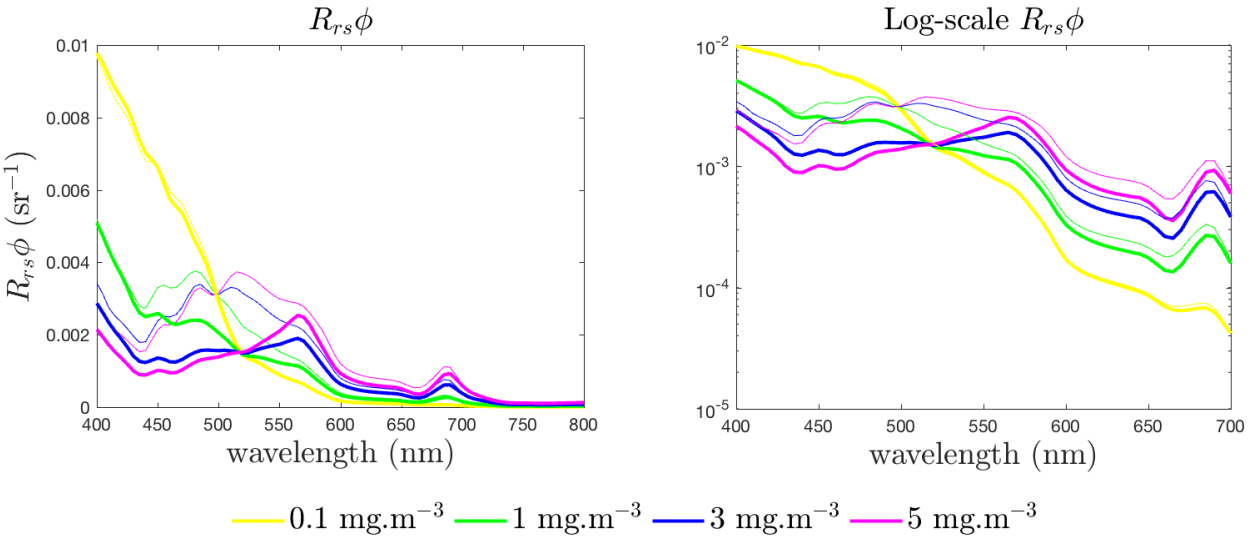

Figure 4.13: Low biomass $R_{rs}\phi$ spectra for Chl *a*-carotenoid-containing (thick line) and phycoerythrin-containing (thin line) assemblages at varying biomass as indicated. The phycoerythrin-containing assemblage is modelled with $D_{eff} = 1$ μm, representing *Synechococcus sp.*. The eukaryote assemblage is modelled with $D_{eff} = 8$ μm, representing diatoms. The resulting size and pigment changes approximate those at the onset of the Southern Ocean spring bloom.

As this example is not only size-driven but also features pigment changes, the

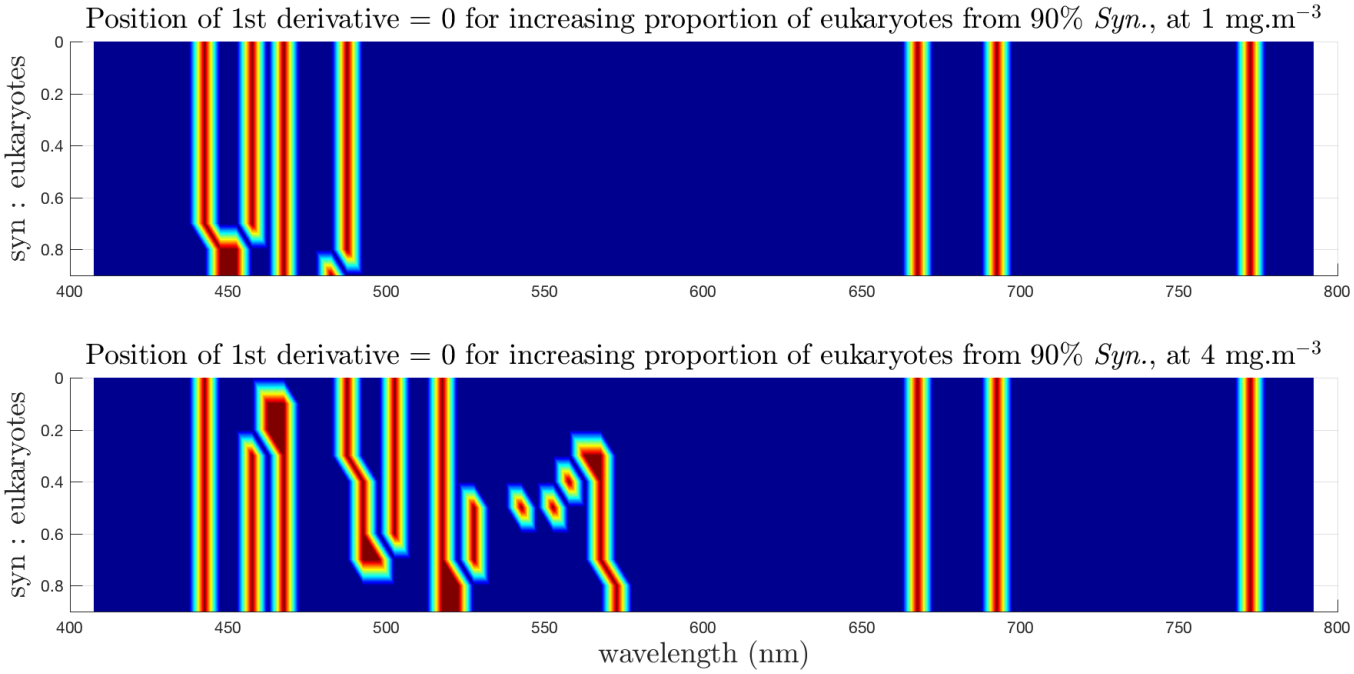

Figure 4.14: Low biomass pigment changes: the spectral position of the first derivative = 0, indicating peaks and troughs in the spectral signal, for decreasing proportions of *Synnechoccocus* as the proportion of diatoms rises. The δD_{eff} is from just over 1 μm at 90% *Synnechoccocus*, to 8 μm at 100% diatoms. The derivatives are shown for 1 and 4 mg.m^{-3}.

spectral position of the first derivative $\frac{dx}{dy}\ R_{rs}\phi = 0$ (i.e. peaks and troughs in $R_{rs}\phi$), is modelled with the incremental change in proportional contribution of *Synechococcus sp.* to diatoms, with the initial population comprising 90% *Synechococcus sp.* (with D_{eff} 1 μm) and 10 % diatoms (with D_{eff} 8 μm) (Fig. 4.14). A Savitzky-Golay filter was used on 5 nm spectral resolution data to calculate the derivatives. At 1 mg.m^{-3}, some small variability is observed but the shift in peak positions is arguably not detectable at this resolution. At 4 mg.m^{-3}, the effect of phycoerythrin appears clearly, and can be observed shifting to shorter wavelengths as the assemblage comprises more and more diatoms, until it eventually disappears. Note that this signal is not entirely due to phycoerythrin, as this is an important spectral region for size changes too. These combined effects form the instability in the position of peaks and troughs visible in Fig. 4.14 between 520 and 570 nm, meaning that even at a relatively high biomass of 4 mg.m^{-3}, the changing signal in the first derivative can only be detected with confidence once the assemblage is almost entirely comprises

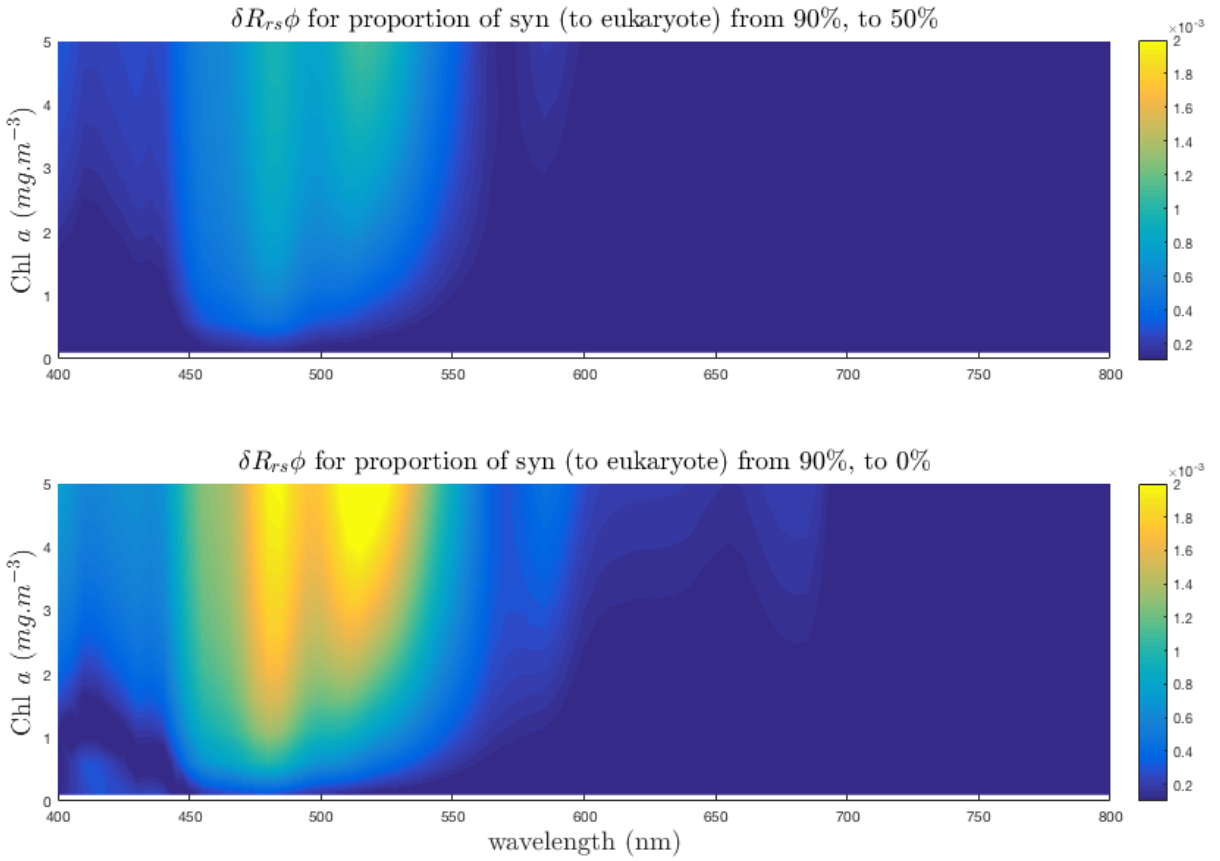

Figure 4.15: $\delta R_{rs}\phi$ shown for a decreasing proportion of *Synechococcus sp.* to diatoms, over a range of Chl a concentrations (1 to 5 mg.m^{-3}) μm. The δD_{eff} is from 1 μm to 8 μm at 100% diatoms.

either one phytoplankton group or the other. This is a similar observation to that in Morel (1997), which concludes that detecting the phycoerythrin pigment differential is difficult even in substantial biomass (Chl $a \sim 1.25$ mg.m^{-3}).

The position of the derivative addresses the spectral peak position shifts, but it remains to be seen whether the magnitude of the δR_{rs} at a given wavelength is large enough to be detectable. Fig. 4.15 shows the strength of the δR_{rs} signal from the initial assemblage of 90% *Synechococcus sp.* to 50% eukaryote (diatoms) and 100% eukaryote respectively. Note that these features do not represent individual peaks or troughs, but rather the resulting difference in $R_{rs}\phi$ as the spectral character of the assemblages are impacted by both size and pigment effects. Importantly, the spectral regions of maximum δR_{rs} for this biomass range are not impacted by the

proportion of *Synechococcus sp.* to ekaryotes, but the signal is strengthened by increasing the change in both forms of assemblage variability - biomass and PFT composition.

It is logical that the 520 nm signal in Fig. 4.15 will be less impacted by variability in a_{gd}, and so given its similar magnitude to that at 480 nm, it is the 520 nm signal that holds the most potential for PFT identification from a δR_{rs} perspective. Fig. 4. 16 shows how the signal at 520 nm changes (from 90 to 10 % *Synechococcus sp.*), against a background of changing $a_{gd}(\lambda)$ and $b_{bnap}(\lambda)$. Where these reach a difference of δR_{rs} of 1×10^{-3} sr^{-1}, shown in red, this indicates a large enough change in signal to be detected by satellite radiometry with confidence. For the greatest change in assemblage composition, the δR_{rs} is detectable from about 1.5 $\mathrm{mg.m}^{-3}$ but shows slight sensitivity to a_{gd} as well as b_{bnap}. These sensitivities are opposing: $a_{gd}(520)$ decreases $\delta R_{rs}(520)$ while $b_{bnap}(520)$ increases the difference, for a given Chl *a* concentration. This optical relationship is complex even in this idealised scenario.

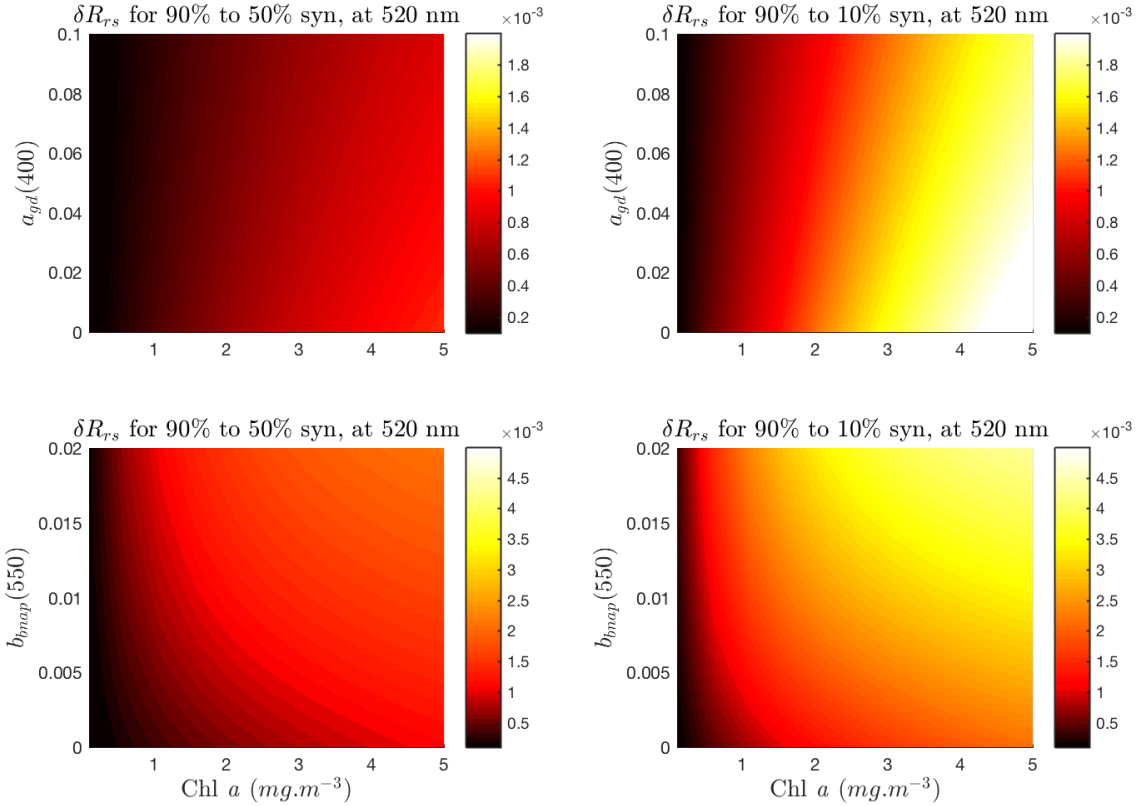

Figure 4.16: Case Study 2b: δR_{rs} under varying $a_{gd}(\lambda)$ and $b_{bnap}(\lambda)$ conditions, shown at 520 nm (region of maximum $\delta R_{rs}\phi$) for varying proportions of *Synechococcus sp.* to diatoms, over a range of Chl a concentrations (1 to 5 mg.m^{-3}).

Summary of observations on pigments

In the Benguela-like example, the effect of δD_{eff} is removed, and differences result only from pigment changes. Despite the high biomass range, and therefore a large proportion of the total backscatter being due to phytoplankton, the maximum $\delta R_{rs}\phi$ appears very sensitive to the influence of $b_{bnap}(\lambda)$. This differentiates this example from the other case studies and suggests that it is differences in (back)scatter due to a change in D_{eff} (not present in this example), which drives an identifiable PFT signal, and that differences due mainly to absorption characteristics (i.e. different accessory pigments), are less robust in the context of the bulk R_{rs} signal (i.e. in spectral regions where size-related features appear in the backscatter).

The spring bloom study considers the optical transition from a small-celled, phycoerythrin-containing assemblage, to a mid-sized-celled, fucoxanthin-containing assemblage, at relatively low biomass. The resulting changes in R_{rs} are driven by both size- and pigment-related optical features. A transition from 90% to 50% *Synnechococcus* yields a sufficient signal at the highest biomass of this Chl *a* range (i.e. approaching 5 mg.m^{-3}), and is interestingly comparatively less sensitive to the non-algal constituents than the corresponding transition from 90% to 0% *Synnechococcus* (i.e. to 100% diatoms), which is detectable at lower biomass (around 1 mg.m^{-3}), but sensitive to variability in $b_{bnap}(\lambda)$.

4.4.3 Conclusions from the Case Studies

The water-leaving signal in the blue spectral region is highly complex and causally ambiguous, with varied and contrasting effects of the variously absorbing and scattering characteristics of both the algal and non-algal in-water constituents. PFT approaches based on the features of phytoplankton absorption (where the largest signal is in the blue) all suffer from this shortcoming where phytoplankton relationships with $a_{gd}(\lambda)$ and $b_{bnap}(\lambda)$ are not well characterised. So it can be concluded from these examples that even where R_{rs} is absorption-dominated (i.e. in low biomass), it is the (back)scattering properties of phytoplankton that show potential for PFT identification, as the $b_{b\phi}$ signal is the most pronounced in less ambiguous spectral

regions. (Phytoplankton whose prominent absorption features are at longer wavelengths, such as phycocyanin-containing cyanobacteria, present a different case.)

This finding exposes a vulnerability in historical approaches to phytoplankton identification and quantification based on absorption characteristics in the blue. Overall, spectral scattering properties of natural waters are not well characterised (Tan et al., 2015; Harmel et al., 2016), and phytoplankton spectral backscattering charactersitics are underexploited in terms of their impact on the water-leaving signal. Some progress has been made (Kostadinov et al., 2009; Kostadinov, 2016) but due to the assumption of a Jungian distribution (and the reliance on Mie modelling, which does not adequately represent absorbing particles), there are high uncertainties in PSD retrieval where the slope is low, i.e. highly productive and coastal areas (Kostadinov et al., 2009). This method also assumes that all non-algal scattering is by particles with D_{eff} less than 0.5 μm, and conversely that there is no non-algal scattering by larger particles. So the scope of application of such an approach is limited.

4.5 Sensitivity of EAP size-based PFT detection

4.5.1 Radiometric sensitivity - magnitude of $\delta R_{rs}\phi$

Due to the large number of variables, a completely flexible analysis in terms of Chl *a* concentration, assemblage D_{eff}, and varying non-algal constituents, is challenging to represent graphically. An online tool has been developed to estimate the water-leaving signal as these quantities are varied by the user, so that the interactions of the various optical constituents can be observed interactively at
http://www.sea.uct.ac.za/lisl-lain-thesis

Having established that the PFT signal in the blue is easily overwhelmed by the effects of $a_{gd}(\lambda)$ and $b_{bnap}(\lambda)$, the PFT signal due to phytoplankton scattering in the 500 to 600 nm region can be evaluated for sensitivity in terms of changes in D_{eff} and biomass. In this section the EAP model is again coupled with Hydrolight to simulate expected variability in R_{rs} due to changes in D_{eff} for low and high biomass environments respectively, with the aim of evaluating the sensitivity of the model.

A general allometric approximation of changing D_{eff} from 2 to 8 μm was chosen for the low biomass example (0.1 to 10 mg.m^{-3}), and a change in D_{eff} from 8 to 20 μm for the higher biomass example (10 to 20 mg.m^{-3}). It is recognised that these scenarios do not represent all possible ecological changes, but are reasonable approximations for low and high biomass diatom and dinoflagellate-dominated environments. Note also that these experiments address only the phytoplankton-related signal, indicating only the minimum optically detectable changes, and that it is necessary to evaluate these in the context of ambiguity with varying non-algal constituents when attempting to identify these signals in the bulk R_{rs}.

Figure 4.17 (A) demonstrates how the combined effects of biomass and D_{eff} interact to form the maximum available δR_{rs} signal at low biomass and small size ranges. The figure shows the maximum $\delta R_{rs}\phi$ signal between 520 and 600 nm - as seen in the case studies, the exact wavelength varies with both size difference and biomass. The shifting position of maximum $\delta R_{rs}\phi$ is shown in Fig. 4. 17 (B). Increasing biomass improves the ability to trace change size-related effects. Using 1 $\times$ 10^{-3} as a threshhold for detection by satellite, it can be seen that an ecologically

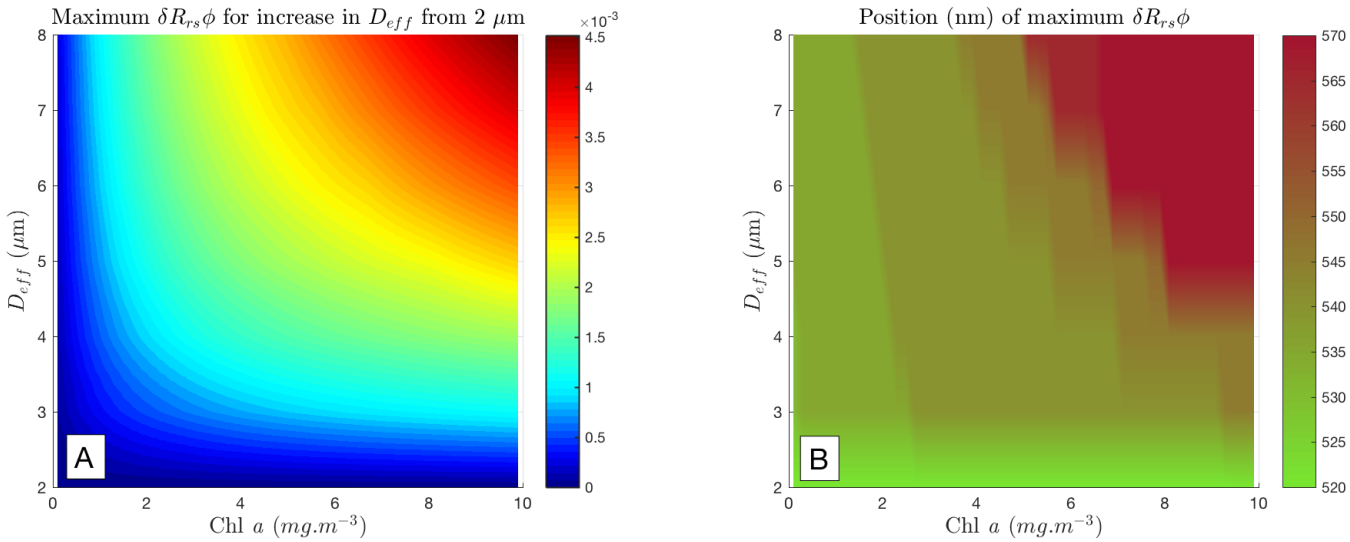

Figure 4.17: Maximum $\delta R_{rs}\phi$ for δD_{eff} from a starting assemblage with D_{eff} 2 μm, as Chl a varies. Note that the $\delta R_{rs}\phi$ occurs at different wavelengths from 500 to 600 nm, and this shows the maximum signal, so there is no exact wavelength information here. Using a difference of 1×10^{-3} sr^{-1} as a threshhold for detection by satellite, it can be seen that by 10 mg.m^{-3} even a small change in D_{eff} results in a detectable change in R_{rs}.

significant shift in D_{eff} from 2 or 3 to 6 μm, such as at the onset of an oceanic bloom, looks potentially detectable from about 2 mg.m^{-3}. By 10 mg.m^{-3} even a small change in D_{eff} results in a detectable change in R_{rs}, but as biomass falls below this, the change in D_{eff} must be increasingly large to be detected.

The spectrally shifting nature of the $\delta R_{rs}\phi$ signal for oceanic PFT applications provides a strong case for hyperspectral sensors in the 520 to 570 nm wavelength region. The extent to which the $\delta R_{rs}\phi$ signal persists in fixed waveband ratios is investigated in the next section on shape sensitivity.

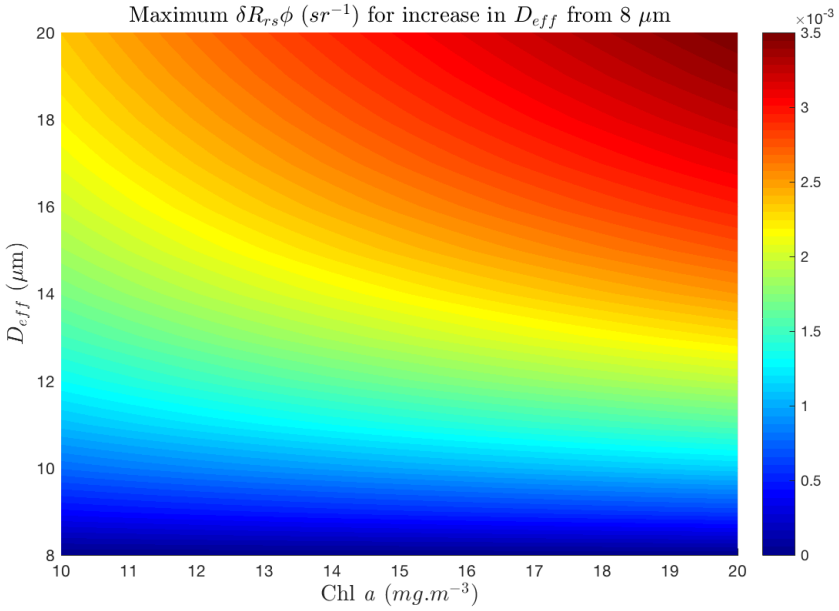

Figure 4.18: Maximum $\delta R_{rs}\phi$ for generalised change in D_{eff} with a high biomass range of Chl *a*. For this biomass and size range, $\delta R_{rs}\phi$ always occurs at 570 nm. The satellite threshhold for detection of change in PFT from 8 μm is easily reached from about 10 μm upwards.

Figure 4.18 shows that in high biomass environments with Chl *a* concentrations of over 10 mg.m^{-3}, the satellite threshhold for detection of change in PFT from 8 μm is easily reached from about 10 μm upwards. For this range of δD_{eff} and Chl *a* concentrations, the maximum δR_{rs} signal is always reached at 570 nm, so no analogous figure to Fig. 4.17(B) is shown.

4.5.2 Spectral shape sensitivity

To further test the sensitivity of the EAP model and the causal IOP variability in terms of identifiable changes in spectral shape from a multi-spectral perspective, $R_{rs}\phi$ ratios for 440:560 nm (blue:green), 560:665 nm (green:red) and 665:710 nm (red:NIR) wavelengths were calculated for a range of D_{eff} and biomass. These are shown in Figure 4.19, representing corresponding changes in both $R_{rs}\phi$ and in the underlying (causal) phytoplankton backscattering and absorption, for these wavelength pairs. The B:G $R_{rs}\phi$ ratio shows a strong biomass dependency and a small sensitivity to size at large sizes, for $0.5 \leq$ Chl $a \leq 4.5$ mg.m^{-3}. The R:NIR ratio shows some sensitivity to larger sizes from about 3 mg.m^{-3} but this decreases as biomass increases. The G:R ratio shows a significant size-related feature for small sizes (≤ 6 μm) from biomass of about 2 mg.m^{-3} upwards (encircled in Fig. 4.19). This where a peak in the corresponding $b_{b\phi}$ ratio appears, suggesting that the large change in magnitude of $b_{b\phi}$ between small D_{eff} (Fig. 4.20) is directly responsible for the sensitivity in the $R_{rs}\phi$ G:R ratio seen in Fig. 4.19.

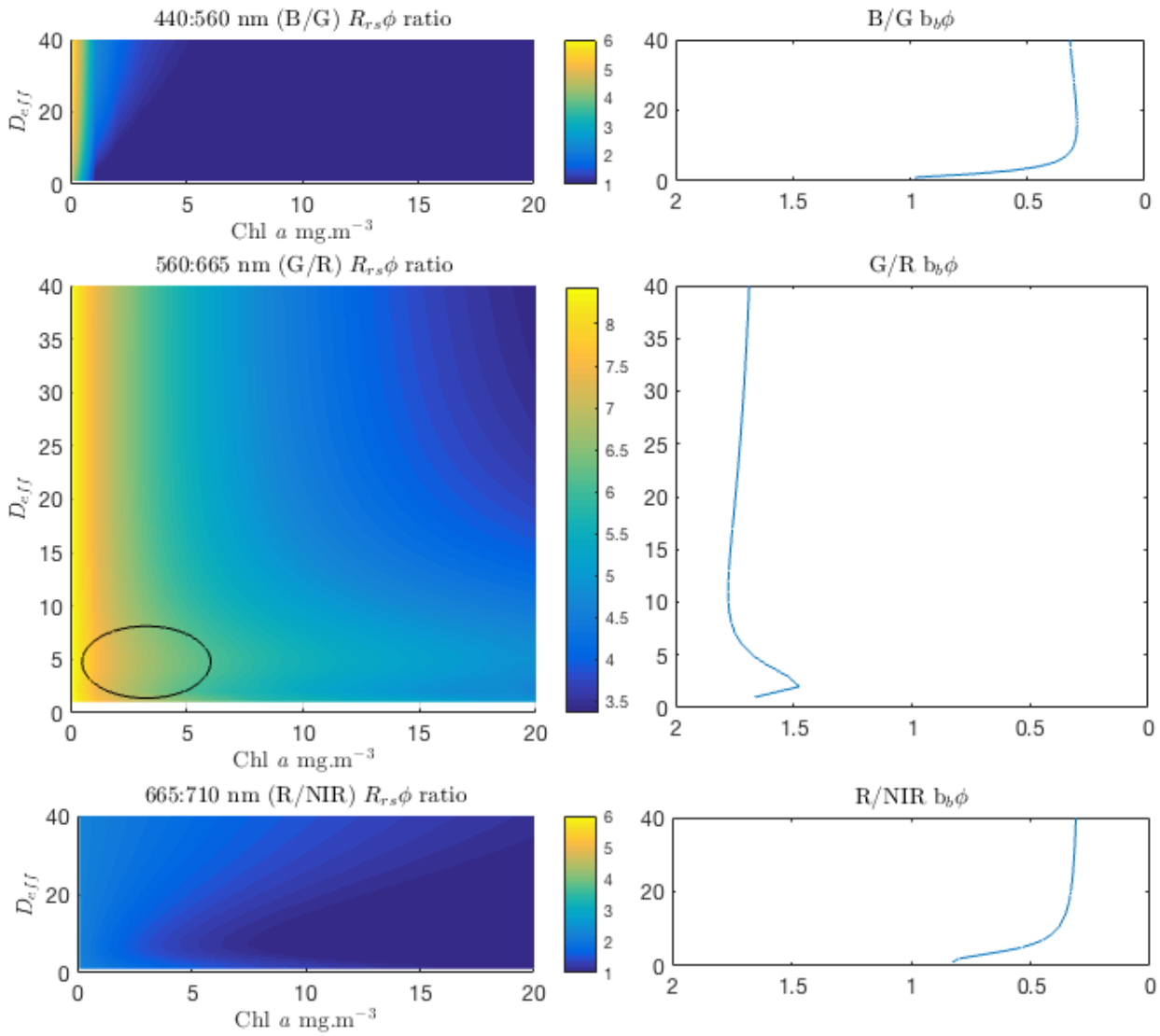

Figure 4.19: $R_{rs}\phi$ ratios for blue:green, green:red and red:NIR wavelengths as shown, for Chl a concentrations of 0.1 to 20 mg.m^{-3} and D_{eff} 1 to 40 μm. The B/G ratio shows a strong biomass dependency and a small sensitivity to size at large sizes, for 0.5 $\leq$ Chl a $\leq$ 4.5 mg.m^{-3}. The $b_{b\phi}$ ratios all display a strong size signal at 2 - 4 μm, and the G/R ratio shows a corresponding size-related feature.

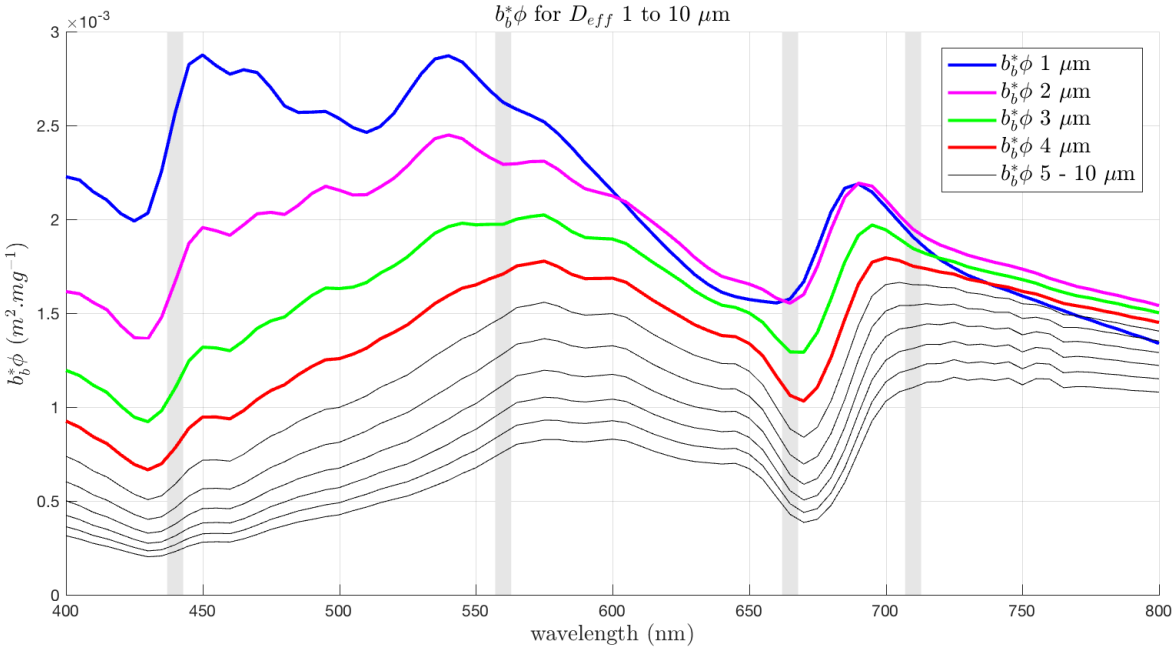

Figure 4.20: $b_b^*\phi$ shown for D_{eff} 1 to 10 μm. The largest differences in backscatter across the spectrum occur between 1 and 4 μm, with the exception of the overlapping of $b_b^*\phi$ in the red and NIR.

This is an important finding. There is a marked size dependency in all of the $b_b^*\phi$ ratios, with the greatest rate of change somewhere between D_{eff} 2 and 8 micron, but it is only in the case of the G:R ratio that the magnitude of the backscatter is sufficient for this signal to be identifiable in the $R_{rs}\phi$. Given that the radiometric signal in the blue is greatly reduced by large phytoplankton absorption and a_{gd}, and the red and NIR wavelengths are similarly affected by the absorption of water, it can be concluded that the the main driver of the useable PFT signal in the green and red is phytoplankton backscatter.

Figure 4.21 shows the rapid increase in the proportional contribution of phytoplankton to total backscatter at 560 and 665 nm. It is known that for typical diatom/dinoflagellate assemblages the 560 nm region is more influenced by backscatter than by absorption. The fact that the magnitude of the total backscatter is much lower at 665 than at 560 nm, together with the strong absorption by water in this region, result in a small useable R_{rs} signal. A 40% contribution of phytoplankton to total b_b at 560 nm corresponds with the limits of detectable $\delta R_{rs}\phi$ in Fig. 4.17(A)

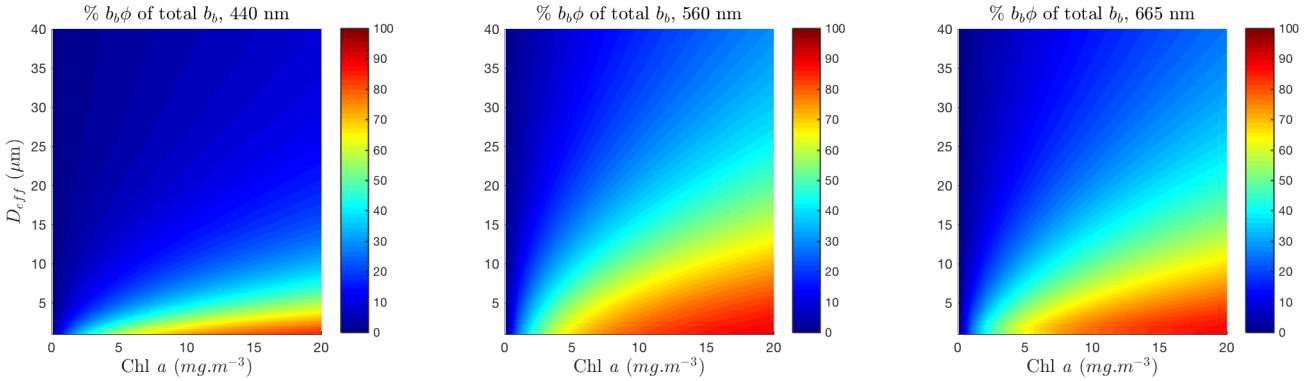

Figure 4.21: Percentage contribution of phytoplankton to total backscatter (including water, and with nominal $b_{bnap}(550) = 0.005$), shown for D_{eff} 1 to 40 μm and Chl a from 0.1 to 20 mg.m^{-3}, at 440, 560 and 665 nm.

(p. 87), indicating that this is the proportion at which phytoplankton backscatter starts driving the bulk water-leaving signal around 560 nm. Consequently, this is the minimum contribution for which some δD_{eff} information may be known. For an oceanic bloom example δD_{eff} from 2 - 6 μm this threshold contribution is reached at about 2 mg.m^{-3}, while to detect an example δD_{eff} of 10 to 20 μm in a diatom/dinoflagellate succession, extremely high biomass is required.

4.6 Considering Uncertainties

Particularly when considering δR_{rs} retrievals from satellite, it is important and necessary to contextualise the magnitude of the PFT signal with respect to uncertainties on the satellite radiometry, and this is detailed in Appendix A.5. It is also important to note that, while the 500 to 600 nm region of promising PFT signal may be mostly insensitive to the effects of non-algal consituents, it is also where variability in R_{rs} due to the different approaches to phytoplankton phase functions is important, leading to upwards of 10% difference in R_{rs} from about 2 mg.m^{-3} (Figs 3.7 and 3.8 in Chapter 3), and implying uncertainty in assemblage D_{eff}.

4.7 Conclusions

In this chapter the complex nature of the R_{rs} signal was examined in detail. A case study from the Southern Ocean looked at differences in R_{rs} due to changes in both biomass and D_{eff} for Chl *a*-carotenoid-dominated phytoplankton, and investigated whether or not the causal effect of δD_{eff} could be identified. A further case study considered the effects of pigment variability (due to phycoerythrin) in addition to δD_{eff}: firstly simulating the onset of the Southern Ocean spring bloom, and secondly looking at Benguela-like conditions. In the case studies the spectral regions of maximum $\delta R_{rs}\phi$ were investigated in terms of their sensitivity to non-algal IOPs. Finally, generalised low and high biomass environments were modelled in order to estimate the thresholds of δD_{eff} and biomass at which the resulting δR_{rs} signal may be detected with confidence. The summarised conclusions of these experiments follows.

Most of the R_{rs} signal that is due to phytoplankton is driven by biomass, and consequently at any significant biomass it is phytoplankton backscatter that dominates the water-leaving signal between 500 and 600 nm where PFT effects are largest. The EAP model shows that the size-related PFT signal is driven by phytoplankton scattering, and that spectral regions where scattering is at its most sensitive to D_{eff} show the most potential for PFT detection from the bulk water-leaving signal. Size-related signal in the blue is too ambiguous to be useful except in very low biomass waters where $a_{gd}(\lambda)$ and $b_{bnap}(\lambda)$ are known to covary predictably with phytoplankton absorption due to Chl *a*. Absorption-based PFT detection algorithms rely on a covariance between phytoplankton and other IOPs which does not always hold. Abundance-based approaches rely on implicit relationships between biomass and assemblage D_{eff} which limit their scope of application.

Isolating variability in $R_{rs}\phi$ as D_{eff} and biomass vary, shows that an example oceanic bloom δD_{eff} from 2 to 6 μm is only detectable at the satellite measurement threshhold of 1×10^{-3} when the biomass reaches 2 mg.m^{-3}. The location of the maximum $\delta R_{rs}\phi$ size feature shifts between 520 and 570 nm (Fig. 4.17 B), suggesting strongly that hyperspectral data in this region would add greater capability here. Further analysis is needed to quantify the potential advantages of hyper- over multi-

spectral data with respect to this shifting maximum signal, and also with respect to the reduced SNR implicit in narrow waveband measurements.

The size-related signal in the 500 to 600 nm region are not always the largest features in the bulk R_{rs}, but they are the most useful as they are sufficiently insensitive to both $a_{gd}(\lambda)$ and $b_{bnap}(\lambda)$. At low biomass where the blue signal dominates, differences in assemblage types can only be detected when they are of unusual magnitude, and additionally, when the non-algal IOPs are known by direct measurement, as satellite a_{gd} retrievals are not sufficiently accurate to resolve the signal ambiguity inherent in this (blue) region.

Depending on the non-algal IOPs, a typical oceanic bloom with δD_{eff} 2 - 8 μm may be identifiable from a biomass of approximately 2 $mg.m^{-1}$. An ecologically significant change in D_{eff} from 8 to 16 μm (representing a possible diatom to dinoflagellate assemblage shift) is comfortably detectable in a biomass environment of over 10 mg.m^{-3}. This confirms the results in Evers-King et al. (2014), which established that EAP D_{eff} can be retrieved with confidence via the inversion of this model from 10 mg.m^{-3} for large D_{eff}. The low biomass sensitivity demonstrated in this chapter presents opportunities for identifying higher resolution size classes than the 2 to 20 μm and >20 μm categories currently frequently employed (Devred et al., 2006; Sathyendranath et al., 2004; Brewin et al., 2017; Kostadinov et al., 2009). The ability to distinguish between diatoms and dinoflagellates in the 2 - 20 μm size class is desirable for marine ecosystem modelling where these two phytoplankton groups are handled independently (Brewin et al., 2017).

The proportional 'net' contribution of phytoplankton i.e. $b_{b\phi}/a_{\phi}$ as a percentage of total b_b/a, has been identified as the driver of PFT sensitivity in the R_{rs}. Given the detectable differences in R_{rs} as size and biomass change, a proportional phytoplankton contribution of approximately 40% appears to a reasonable minimum threshold in terms of yielding a detectable optical change. The proportional contribution always varies with the non-algal optical constituents $a_{gd}(\lambda)$ and $b_{nap}(\lambda)$.

The most useful spectral region for PFT diagnostics in terms of assemblage D_{eff} has been shown to be between 520 and 570 nm. The uncertainty in modelled $R_{rs}\phi$ due to the choice of phase function is in the order of 1×10^{-3} sr^{-1} in this spectral

region, corresponding to an ambiguity in D_{eff} of approximately 4 μm (see Fig. 3.5 - but this varies with the D_{eff} itself). Measurement uncertainty in satellite R_{rs} due to random effects is at its greatest at the shorter wavelengths, estimated at $0.7 - 0.9\times 10^{-3}$ sr^{-1} at 412 nm, decreasing to $0.05 - 0.1\times 10^{-3}$ sr^{-1} at 670 nm. Using an estimated total uncertainty on R_{rs} of 0.0006 sr^{-1} (Gordon, 1997) across the spectrum, this amounts to an uncertainty in the water-leaving signal approaching 1.5 $\times 10^{-3}$ sr^{-1}, which is about half of the measurement itself at the maximum 560 nm feature in R_{rs} for generalised eukaryote assemblages of about 10 mg.m^{-3} upwards (see Fig. 2.6). In the context of these uncertainties, as biomass increases and the R_{rs} signal is reduced, the remaining useable signal for the retrieval of size information is reduced. Returning to the generalised low biomass Fig. 4.17, given an uncertainty of 1.5 $\times 10^{-3}$ sr^{-1} on top of the $\delta R_{rs}\phi$ signal, the range of conditions under which size information may be known with confidence is reduced: an idealised oceanic bloom with δD_{eff} 2 - 8 μm would be detectable with confidence from 4 mg.m^{-3} upwards. In a high biomass environment (Fig. 4.18), a 100% δD_{eff} from 8 to 16 μm, applicable to a potential diatom/dinoflagellate succession, is detectable within uncertainty limits from about 14 mg.m^{-3}.

Chapter 5

Summary and Conclusions

5.1 Thesis summary and conclusions

This thesis addresses some of the core optical complexities at the heart of the effort to identify Phytoplankton Functional Types from satellite radiometry. There is substantial multi-disciplinary interest in PFTs from ocean ecologists, bioegeochemists and climate change scientists, particularly in achieving better closure with global PFT models. Bio-optical and Radiative Transfer models have an important role to play as the only systematic way of understanding the complex interdependency of phytoplankton biomass and the IOP budget and their relationship to the water-leaving signal. An understanding of these interactions is critical to the ability to retrieve PFT-related signal from radiometry. Insight gained is only as good as the models themselves, however, and much improvement is needed in this regard. In particular, the spectral and angular scattering of phytoplankton, shown to be central to the PFT signal, is poorly understood in the context of assemblage variability and its subsequent influence on the bulk water-leaving signal. This work focuses on a fundamental constraint of PFT endeavours so far: that is, the lack of understanding of the PFT signal and its causality.

5.1.1 Model structure and IOP terms

The EAP model, with its origins in high biomass phytoplankton-dominated waters with large radiometric signal, is physically and optically coherent, and therefore al-

lows close, systematic inspection of phytoplankton bio-optical relationships. EAP phytoplankton IOPs are integrated over a choice of phytoplankton size distribution, with specified size bin resolution, and phytoplankton absorption and angular scattering characteristics are biophysically and biogeochemically consistent, derived from the same refractive indices. Coupled with Hydrolight, the EAP model provides a spectrally comprehensive and fully angularly resolved radiative transfer solution.

The performance of the EAP model has been evaluated by comparison with two other commonly used IOP models - those of Lee (2006) and Alvain et al. (2005) - and is shown to be robust under a wide range of biomass conditions. It significantly outperforms the other models in phytoplankton bloom conditions, which provide extremely useful high signal test cases, while comparing well with measured R_{rs} across a wide range of biomass (Chapter 2). This greatly improved degree of closure confirms the appropriate representation of EAP phytoplankton community IOPS. Central to this improved closure is the EAP handling of phytoplankton absorption, which avoids an inherent dependence of D_{eff} on Chl a concentration, making it suitable for use over a wide variety of water types. Also, phytoplankton scattering is addressed explicitly, calculated from first principles, resulting in spectrally variable phytoplankton backscatter and large assemblage-related phase function variability, as seen in Chapter 3.

5.1.2 Angular scattering and phase function models

It is clear that the spectral and angular character of phytoplankton backscatter is important across all water types. The phase function sensitivity study confirms the importance of using fully angularly and spectrally resolved, wavelength-dependent phase functions when scattering dominates the IOPs, and shows that approximating the phase functions can result in significant uncertainties even at intermediate biomass. In low biomass where phytoplankton scattering contributes considerably less to the bulk signal, it must be acknowledged that simplistic models of phytoplankton backscatter will not allow the retrieval of PFT information with any confidence.

5.1.3 Radiometric signal sensitivity and bio-optical characterisation of IOP budget metrics

Radiometric signal in the blue is high in measurement uncertainty and is very sensitive to variability in all of the in-water constituents. This precludes obtaining PFT information at very low biomass (less than about 2 mg.m^{-3}) unless the non-algal contributions are exactly known. Given the low proportional contribution of phytoplankton to total IOPs at low biomass, causal ambiguity in the signal due to non-algal contributions, and measurement uncertainty in the blue spectral region, the best opportunities for PFT retrieval lie between 520 - 570 nm.

Second order assemblage signals were found to be dependent on phytoplankton biomass and the IOP budget in general, showing that these must all be quantitatively considered when interpreting the assemblage signal from either the forward or backward (i.e. via inversion) direction. The proportional contribution of $b_{b\phi}/a_{\phi}$ to the total b_b/a_a was found to be a useful metric for the potential identification of PFT signal in R_{rs}. The case studies revealed further that size-driven features are secondary to those of biomass in the R_{rs}, and that pigment-related features are secondary to size-related features, requiring substantial biomass to be detectable.

5.1.4 Causality and sensitivity of the PFT signal

Isolating the D_{eff} signal at green wavelengths is therefore the key to PFT identification. The spectral location of the maximum PFT signal in $R_{rs}\phi$ shifts towards the longer wavelengths in the 520 - 570 nm range as D_{eff} and biomass increases. The sensitivity of the size signal in the green to non-algal backscatter depends on the wavelength, biomass, and the magnitude of b_{bnap}, D_{eff} and δD_{eff}, and these relationships are complex.

The model shows a direct causal relationship between changes in phytoplankton backscatter and the magnitude of the resultant impact on the $R_{rs}\phi$. Whether or not these changes lead to retrievable size information depend on the magnitude of the R_{rs} (i.e. the presence or absence of strong absorption relative to backscatter) and the proportional contribution of phytoplankton to the total backscatter. In

the visible wavelengths, it is around 560 nm that phytoplankton backscatter has the largest net impact on the water-leaving signal. For Chl *a*-carotenoid dominated assemblages this is a region of low a_ϕ, elevated $b_{b\phi}$, and the bulk optical signal is large and not overly ambiguated by the impact of non-algal constituents under Case 1 type conditions. A percentage contribution of 40% $b_{b\phi}$ to total b_b at 560 nm (Fig. 4.21) was found to correspond with the threshold of minimum measureable $\delta R_{rs}\phi$ signal in this region (Fig. 4.17A).

It corresponds then, that this green spectral region of scattering-driven maximum useable PFT signal is also the region of maximum uncertainty due to approximations made in the handling of modelled phytoplankton (back)scatter (as seen in Chapter 3, and in Fig. A.3). The uncertainty in modelled $R_{rs}\phi$ due to the choice of phase function is in the order of 1×10^{-3} sr^{-1} in this spectral region, corresponding to an ambiguity in D_{eff} of approximately 4 μm (see Fig. 3.5 - but this varies with the D_{eff} itself). Using an estimated total uncertainty on R_{rs} of 0.0006 sr^{-1} (Gordon, 1997) across the spectrum, this amounts to an uncertainty in the water-leaving signal approaching 1.5×10^{-3} sr^{-1}, which is about half of the measurement itself at the maximum 560 nm feature in R_{rs} for generalised eukaryote assemblages of about 10 mg.m^{-3} upwards (see Fig. 2.6). In the context of these uncertainties, as biomass increases and the R_{rs} signal is reduced, the remaining useable signal for the retrieval of size information is also reduced, requiring larger changes in D_{eff} to result in a sufficient change in $b_{b\phi}$ while maintaining the threshold contribution to the total backscatter.

This level of uncertainty affects the range of conditions under which size information may be known with confidence. An idealised oceanic bloom with δD_{eff} 2 - 8 μm would be detectable with confidence from 4 mg.m^{-3} upwards, while in a high biomass environment (Fig. 4.18), a 100% δD_{eff} from 8 to 16 μm, applicable to a potential diatom/dinoflagellate succession, is detectable within uncertainty limits from about 14 mg.m^{-3}.

5.1.5 Conclusion: Key findings

Despite the presence of some low biomass assemblage D_{eff} information in $R_{rs}\phi$ in the blue spectral region, the bulk satellite R_{rs} signal here is highly causally ambiguous and radiometrically imprecise, rendering it unsuitable for PFT detection. The very strong dependence of the 440:560 nm (blue/green) ratio on biomass (successfully exploited by many Chl *a* algorithms), gives it much greater ambiguity with respect to assemblage D_{eff}, whose optical signal has been found to be driven by phytoplankton backscatter.

The relatively small radiometric signal at 665 nm, where both phytoplankton and water absorb strongly but scatter comparatively weakly, is shown to be a good reference wavelength for a 560:665 nm (red/green) ratio, revealing size information driven by changes in phytoplankton backscatter. Size information in this wavelength ratio persists for significant ecological assemblage changes even when the maximum $\delta R_{rs}\phi$ signal is located flexibly between 520 and 570 nm, provided the biomass is high enough.

5.2 Recommendations

The importance of the detailed nature of phytoplankton backscatter is underestimated by the ocean colour community, and this must be addressed if PFT identification techniques are to improve. Better knowledge and routine observations of multi-spectral angular scattering functions in a variety of water types are essential to furthering these efforts, and this requires improved measurement technology and processing protocols. The increased availability of bio-optical models, radiative transfer models and appropriate phase functions would encourage more widespread community use of radiative transfer models with spectrally variable phase functions.

Knowledge of the biophysical characterisation of phytoplankton communities and community diversity also requires development, ideally by routine or systematic observations across a variety of ecological environments and events. Improvements in instrument technology will drive this capability.

The sensitivity analyses in this document can be used to guide more appropri-

ately constrained PFT algorithms, both empirical and semi-analytical. The sensitivity of D_{eff} change with biomass is an excellent example of how PFT detection in a certain biomass range can be improved.

There is a requirement for more quantitative and causally based analyses of the PFT signal, as well as inversion and application algorithms, from both multi- and hyperspectral perspectives. The causal complexity of the signal and its sensitivity to uncertainties in the radiometric signal as well as to wavelength indicate a requirement for more spectral information in the 520 - 600 nm region, which is underrepresented by current satellite sensors (it is recommended that due to the phycocyanin absorption feature at 580 nm the range be extended past the wavelength of maximum D_{eff} signal to 600 nm). However, a comprehensive multi- versus hyperspectral study is needed to evaluate the potential gains from hyperspectral data in the context of community requirements in terms of PFT assemblage change information. The modelled R_{rs} signal at 665 nm has been shown to be a useful reference wavelength for a size-sensitive green:red ratio, but in practice the radiometric sensitivity of an equivalent satellite wavelength band requires consideration as typical water-leaving R_{rs} signal is small in this spectral region, and a narrow waveband additionally implies a reduced signal-to-noise ratio.

Bibliography

Agusti, S., Duarte, C. M., and Kalff, J. (1987). Algal cell size and the maximum density and biomass of phytoplankton. *Limnology and Oceanography*, 32(4):983–986.

Alvain, S., Loisel, H., and Dessailly, D. (2012). Theoretical analysis of ocean color radiances anomalies and implications for phytoplankton groups detection in Case 1 waters. *Optics Express*, 20:1070–1083.

Alvain, S., Moulin, C., Dandonneau, Y., and Bréon, F.-M. (2005). Remote sensing of phytoplankton groups in Case 1 waters from global SeaWiFS imagery. *Deep Sea Research Part I: Oceanographic Research Papers*, 52(11):1989–2004.

Anderson, T. R. (2005). Plankton functional type modelling: running before we can walk? *Journal of Plankton Research*, 27(11):1073–1081.

Antoine, D., d'Ortenzio, F., Hooker, S. B., Bcu, G., Gentili, B., Tailliez, D., and Scott, A. J. (2008). Assessment of uncertainty in the ocean reflectance determined by three satellite ocean color sensors (MERIS, SeaWiFS and MODIS-A) at an offshore site in the mediterranean sea (BOUSSOLE project). *Journal of Geophysical Research: Oceans*, 113(C7):2156–2202. C07013.

Behrenfeld, M. J., Westberry, T. K., and Boss, E. (2009). Satellite-detected fluorescence reveals global physiology of ocean phytoplankton. *Biogeosciences*, pages 779–794.

Bernard, S., Pitcher, G., Evers-King, H., Robertson, L., Matthews, M., Rabagliati, A., and Balt, C. (2014). Ocean colour remote sensing of harmful algal blooms

in the benguela system. In *Remote Sensing of the African Seas*, pages 185–203. Springer.

Bernard, S., Probyn, T. A., and Quirantes, A. (2009). Simulating the optical properties of phytoplankton cells using a two-layered spherical geometry. *Biogeosciences Discussions*, 6:1497–1563.

Bernard, S., Probyn, T. A., and Shillington, F. A. (1998). Towards the validation of SeaWiFS in southern African waters: the effects of gelbstoff. *South African Journal of Marine Science*, 19:15–25.

Bernard, S., Shillington, F. A., and Probyn, T. A. (2007). The use of equivalent size distributions of natural phytoplankton assemblages for optical modeling. *Optics Express*, 15:1995–2007.

Boss, E. and Pegau, W. S. (2001). Relationship of light scattering at an angle in the backward direction to the backscattering coefficient. *Applied Optics*, 40:5503–5507.

Boyd, P. and Ellwood, M. (2010). The biogeochemical cycle of iron in the ocean. *Nature Geoscience*, 10(1038):675–682.

Brewin, R. J. W., Ciavatta, S., Sathyendranath, S., Jackson, T., Tilstone, G., Curran, K., Airs, R. L., Cummings, D., Brotas, V., Organelli, E., Dall'Olmo, G., and Raitsos, D. E. (2017). Uncertainty in ocean-color estimates of chlorophyll for phytoplankton groups. *Frontiers in Marine Science*, 4:104.

Bricaud, A., Babin, M., Morel, A., and Claustre, H. (1995). Variability in the chlorophyll-specific absorption coefficients of natural phytoplankton: Analysis and parameterization. *Journal of Geophysical Research*, 100:13321–13332.

Bricaud, A., Bédhomme, A., and Morel, A. (1988). Optical properties of diverse phytoplanktonic species: Experimental results and theoretical interpretation. *Journal of Plankton Research*, 10:851–873.

Bricaud, A., Claustre, H., Ras, J., and Oubelkheir, K. (2004). Natural variability of phytoplanktonic absorption in oceanic waters: Influence of the size structure of algal populations. *Journal of Geophysical Research: Oceans*, 109(C11).

Bricaud, A., Morel, A., and Prieur, L. (1981). Absorption by dissolved organic matter of the sea (yellow substance) in the UV and visible domains. *Limnology and Oceanography*, 26:43–53.

Brown, C. A., Huot, Y., Werdell, P. J., Gentili, B., and Claustre, H. (2008). The origin and global distribution of second order variability in satellite ocean color and its potential applications to algorithm development. *Remote Sensing of Environment*, 112(12):4186–4203.

Carder, K. L., Hawes, S. K., Baker, K. A., Smith, R. C., Steward, R. G., and Mitchell, B. G. (1991). Reflectance model for quantifying chlorophyll a in the presence of productivity degradation products. *Journal of Geophysical Research: Oceans (1978-2012)*, 96:20599–20611.

Chami, M., McKee, D., Leymarie, E., and Khomenko, G. (2006a). Influence of the angular shape of the volume-scattering function and multiple scattering on remote sensing reflectance. *Applied Optics*, 45:9210–9220.

Chami, M., Shybanov, E. B., Khomenko, G. A., Lee, M. E. G., Martynov, O. V., and Korotaev, G. K. (2006b). Spectral variation of the volume scattering function measured over the full range of scattering angles in a coastal environment. *Applied Optics*, 45:3605–3619.

Chami, M., Thirouard, A., and Harmel, T. (2014). POLVSM (Polarized Volume Scattering Meter) instrument: an innovative device to measure the directional and polarized scattering properties of hydrosols. *Optics Express*, 22:26403–26428.

Chislock, M. F., Doster, E., and Zitomer, R. A. (2013). Eutrophication: Causes, consequences and controls in aquatic ecosystems. *Nature Education Knowledge*, 4.

Ciotti, A. M. and Bricaud, A. (2006). Retrievals of a size parameter for phytoplankton and spectral light absorption by colored detrital matter from water-leaving radiances at SeaWiFS channels in a continental shelf region off Brazil. *Limnology and Oceanography: Methods*, 4(7):237–253.

Ciotti, A. M., Lewis, M. R., and Cullen, J. J. (2002). Assessment of the relationships between dominant cell size in natural phytoplankton communities and the spectral shape of the absorption coefficient. *Limnology and Oceanography*, 47(2):404–417.

Constable, A. J., Melbourne-Thomas, J., Corney, S. P., Arrigo, K. R., Barbraud, C., Barnes, D., Bindoff, N. L., Boyd, P. W., Brandt, A., Costa, D. P., et al. (2014). Climate change and Southern Ocean ecosystems I: how changes in physical habitats directly affect marine biota. *Global Change Biology*, 20(10):3004–3025.

Crichton, M., Hutchings, L., Lamont, T., and Jarre, A. (2013). From physics to phytoplankton: prediction of dominant cell size in St Helena Bay in the Southern Benguela. *Journal of Plankton Research*, 35:526–541.

Dall'Olmo, G., Westberry, T., Behrenfeld, M., Boss, E., and Slade, W. (2009). Direct contribution of phytoplankton-sized particles to optical backscattering in the open ocean. *Biogeosciences Discussions*, 6(1).

Del Castillo, C. E. and Miller, R. L. (2011). Horizontal and vertical distributions of colored dissolved organic matter during the Southern Ocean Gas Exchange Experiment. *Journal of Geophysical Research: Oceans*, 116(C4).

Devred, E., Sathyendranath, S., Stuart, V., Maass, H., Ulloa, O., and Platt, T. (2006). A two-component model of phytoplankton absorption in the open ocean: Theory and applications. *Journal of Geophysical Research: Oceans*, 111(C3).

Dierssen, H. M., Kudela, R. M., and Ryan, J. P. (2006). Red and black tides: Quantitative analysis of water-leaving radiance and perceived color for phytoplankton, colored dissolved organic matter, and suspended sediments. *Limnology and Oceanography*, 51:2646–2659.

Dubelaar, G. B., Visser, J. W., and Donze, M. (1987). Anomalous behaviour of forward and perpendicular light scattering of a cyanobacterium owing to intracellular gas vacuoles. *Cytometry*, 8:405–412.

Dutkiewicz, S., Hickman, A., Jahn, O., Gregg, W., Mouw, C., and Follows, M. (2015). Capturing optically important constituents and properties in a marine biogeochemical and ecosystem model. *Biogeosciences*, 12:4447–4481.

Evers-King, H., Bernard, S., Lain, L. R., and Probyn, T. A. (2014). Sensitivity in reflectance attributed to phytoplankton cell size: forward and inverse modelling approaches. *Optics Express*, 22:11536–11551.

Fawcett, A., Pitcher, G. C., Bernard, S., and Cembella, A. (2007). Contrasting wind patterns and toxigenic phytoplankton in the southern Benguela upwelling system. *Marine Ecology Progress Series*, 348:19–31.

Field, C. B., Behrenfeld, M. J., and Randerson, J. T. (1998). Primary production of the biosphere: integrating terrestrial and oceanic components. *Science*, 281(5374):237–240.

Fischer, J. and Fell, F. (1999). Simulation of MERIS measurements above selected ocean waters. *International Journal of Remote Sensing*, 20:1787–1807.

Fournier, G. R. and Forand, J. L. (1994). *Analytic phase function for ocean water*. Ocean Optics XII. International Society for Optics and Photonics.

Freda, W. (2012). Spectral dependence of the correlation between the backscattering coefficient and the volume scattering function measured in the southern Baltic Sea. *Oceanologia*, 54:355–367.

Freda, W. and Piskozub, J. (2007). Improved method of Fournier-Forand marine phase function parameterization. *Optics Express*, 15:12763–12768.

Gordon, H. R. (1997). Atmospheric correction of ocean color imagery in the Earth Observing System era. *Journal of Geophysical Research: Atmospheres*, 102(D14):17081–17106.

Greene, R. M., Geider, R. J., Kolber, Z., and Falkowski, P. G. (1992). Iron-induced changes in light harvesting and photochemical energy conversion processes in eukaryotic marine algae. *Plant Physiology*, 100(2):565–575.

Gustafson Jr, D. E., Stoecker, D. K., Johnson, M. D., Van Heukelem, W. F., and Sneider, K. (2000). Cryptophyte algae are robbed of their organelles by the marine ciliate Mesodinium rubrum. *Nature*, 405(6790):1049.

Harmel, T., Hieronymi, M., Slade, W., Röttgers, R., Roullier, F., and Chami, M. (2016). Laboratory experiments for inter-comparison of three volume scattering meters to measure angular scattering properties of hydrosols. *Optics Express*, 24:234–256.

Hoepffner, N. and Sathyendranath, S. (1991). Effect of pigment composition on absorption properties of phytoplankton. *Marine Ecology Progress Series*, pages 11–23.

Holm-Hansen, O., Lorenzen, C. J., Holmes, R. W., and Strickland, J. D. (1965). Fluorometric determination of chlorophyll. *ICES Journal of Marine Science*, 30(1):3–15.

IOCCG (2014). *Phytoplankton Functional Types from Space*, volume No. 15 of *Reports of the International Ocean Colour Coordinating Group*. IOCCG, Dartmouth, Canada.

Johnsen, G., Samset, O., Granskog, L., and Sakshaug, E. (1994). In vivo absorption characteristics in 10 classes of bloom-forming phytoplankton: taconomic characteristics and responses to photoadaptation by means of discriminant and hplc analysis. *Marine Ecology Progress Series*, pages 149–157.

Kostadinov, T., Siegel, D., and Maritorena, S. (2009). Retrieval of the particle size distribution from satellite ocean color observations. *Journal of Geophysical Research: Oceans*, 114(C9).

Kostadinov, T. S. (2016). Carbon-based phytoplankton size classes retrieved via ocean color estimates of the particle size distribution. *Ocean Science*, 12(2):561.

Lain, L. R., Bernard, S., and Evers-King, H. (2014). Biophysical modelling of phytoplankton communities from first principles using two-layered spheres: Equivalent Algal Populations (EAP) model. *Optics Express*, 22:16745–16758.

Lain, L. R., Bernard, S., and Matthews, M. W. (2017). Understanding the contribution of phytoplankton phase functions to uncertainties in the water colour signal. *Optics Express*, 25(4):A151–A165.

Le Quéré, C., Harrison, S. P., C. Prentice, I., Buitenhuis, E. T., Aumont, O., Bopp, L., Claustre, H., Cotrim Da Cunha, L., Geider, R., Giraud, X., et al. (2005). Ecosystem dynamics based on plankton functional types for global ocean biogeochemistry models. *Global Change Biology*, 11(11):2016–2040.

Leathers, R. A., Downes, T. V., and Mobley, C. D. (2001). Self-shading correction for upwelling sea-surface radiance measurements made with buoyed instruments. *Optics Express*, 8:561–570.

Lee, Z. P. (2006). (ed) remote sensing of Inherent Optical Properties: Fundamentals, tests of algorithms and applications. *Reports of the International Ocean Colour Coordinating Group*, 5:1–122.

Lefering, I., Bengil, F., Trees, C., Röttgers, R., Bowers, D., Nimmo-Smith, A., Schwarz, J., and McKee, D. (2016). Optical closure in marine waters from in situ inherent optical property measurements. *Optics Express*, 24:14036–14052.

Matsuoka, A., Huot, Y., Shimada, K., Saitoh, S.-I., and Babin, M. (2007). Bio-optical characteristics of the western Arctic Ocean: implications for ocean color algorithms. *Canadian Journal of Remote Sensing*, 33(6):503–518.

Matthews, M. W. and Bernard, S. (2013). Using a two-layered sphere model to investigate the impact of gas vacuoles on the inherent optical properties of M. aeruginosa. *Biogeosciences*, 10:8139–8157.

Matthews, M. W., Bernard, S., and Robertson, L. (2012). An algorithm for detecting trophic status (chlorophyll-a), cyanobacterial-dominance, surface scums and

floating vegetation in inland and coastal waters. *Remote Sensing of Environment*, 124:637–652.

McClain, C. R. (2009). A decade of satellite ocean color observations. *Annual Review of Marine Science*, 1:19–42.

McKee, D. and Cunningham, A. (2005). Evidence for wavelength dependence of the scattering phase function and its implication for modeling radiance transfer in shelf seas. *Applied Optics*, 44(1):126–135.

Mélin, F., Sclep, G., Jackson, T., and Sathyendranath, S. (2016). Uncertainty estimates of remote sensing reflectance derived from comparison of ocean color satellite data sets. *Remote Sensing of Environment*, 177:107 – 124.

Mélin, F., Zibordi, G., and Berthon, J.-F. (2007). Assessment of satellite ocean color products at a coastal site. *Remote Sensing of Environment*, 110(2):192–215.

Mishchenko, M. I., Travis, L. D., and Lacis, A. A. (2002). *Scattering, absorption, and emission of light by small particles*. Cambridge university press.

Mobley, C. D., Sundman, L. K., and Boss, E. (2002). Phase function effects on oceanic light fields. *Applied Optics*, 41:1035–1050.

Morel, A. (1997). Consequences of a synechococcus bloom upon the optical properties of oceanic (case 1) waters. *Limnology and Oceanography*, 42(8):1746–1754.

Morel, A., Ahn, Y.-H., Partensky, F., Vaulot, D., and Claustre, H. (1993). Prochlorococcus and Synechococcus: a comparative study of their optical properties in relation to their size and pigmentation. *Journal of Marine Research*, 51(3):617–649.

Morel, A. and Bricaud, A. (1986). Inherent optical properties of algal cells, including picoplankton: theoretical and experimental results. *Canadian Journal of Fisheries and Aquatic Sciences*, 214:521–559.

Morel, A. and Maritorena, S. (2001). Bio-optical properties of oceanic waters: A reappraisal. *Journal of Geophysical Research*, 106:7163–7180.

Morel, A. and Prieur, L. (1977). Analysis of variations in ocean color. *Limnology and Oceanography*, 22(4):709–722.

Moutier, W., Duforet-Gaurier, L., Thyssen, M., Loisel, H., Meriaux, X., L.Courcot, Dessailly, D., Reve, A.-H., Gregori, G., Alvain, S., Barani, A., Brutier, L., and Dugenne, M. (in press, 2017). Evolution of the scattering properties of phytoplankton cells from flow cytometry measurements.

Mtshali, T. N. (2016). Sanae 55 cruise report.

Nair, A., Sathyendranath, S., Platt, T., Morales, J., Stuart, V., Forget, M.-H., Devred, E., and Bouman, H. (2008). Remote sensing of phytoplankton functional types. *Remote Sensing of Environment*, 112(8):3366 – 3375. Earth Observations for Marine and Coastal Biodiversity and Ecosystems Special Issue.

Olson, R., Zettler, E., and Anderson, O. (1989). Discrimination of eukaryotic phytoplankton cell types from light scatter and autofluorescence properties measured by flow cytometry. *Cytometry Part A*, 10(5):636–643.

O'Reilly, J. E., Maritorena, S., Mitchell, B. G., Siegel, D. A., Carder, K. L., Garver, S. A., Kahru, M., and McClain, C. (1998). Ocean color chlorophyll algorithms for SeaWiFS. *Journal of Geophysical Research*, 103:24937–24953.

Organelli, E., Nuccio, C., Lazzara, L., Uitz, J., Bricaud, A., and Massi, L. (2017). On the discrimination of multiple phytoplankton groups from light absorption spectra of assemblages with mixed taxonomic composition and variable light conditions. *Applied Optics*, 56(14):3952.

Ostrowska, M., Woźniak, B., and Dera, J. (2012). Modelled quantum yields and energy efficiency of fluorescence photosynthesis and heat production by phytoplankton in the World Ocean. *Oceanologia*, 54:565–610.

Probyn, T. A., Bernard, S., Pitcher, G. C., and Pienaar, R. N. (2010). Ecophysiological studies on Aureococcus anophagefferens blooms in Saldanha Bay, South Africa. *Harmful Algae*, 9(2):123–133.

Quirantes, A. and Bernard, S. (2006). Light-scattering methods for modelling algal particles as a collection of coated and/or nonspherical scatterers. *Journal of Quantitative Spectroscopy and Radiative Transfer*, 100(1):315–324.

Reynolds, R., Stramski, D., and Mitchell, B. (2001). A chlorophyll-dependent semi-analytical reflectance model derived from field measurements of absorption and backscattering coefficients within the Southern Ocean. *Journal of Geophysical Research: Oceans*, 106(C4):7125–7138.

Roesler, C. S. and Perry, M. J. (1995). In situ phytoplankton absorption, fluorescence emission, and particulate backscattering spectra determined from reflectance. *Journal of Geophysical Research*, 100:13279–13294.

Roesler, C. S., Perry, M. J., and Carder, K. L. (1989). Modeling in situ phytoplankton absorption from total absorption spectra in productive inland marine waters. *Limnology and Oceanography*, 34:1510–1523.

Ryan-Keogh, T. J., Thomalla, S. J., Mtshali, T. N., and Little, H. (in press, 2017). Modelled estimates of spatial variability of iron stress in the Atlantic sector of the Southern Ocean.

Sathyendranath, S., Aiken, J., Alvain, S., Barlow, R., Bouman, H., Bracher, A., Brewin, R., Bricaud, A., Brown, C. W., Ciotti, A. M., Clementson, L. A., Craig, S. E., Devred, E., Hardman-Mountford, N., Hirata, T., Hu, C., Kostadinov, T. S., Lavender, S., Loisel, H., Moore, T. S., Morales, J., Mouw, C. B., Nair, A., Raitsos, D., Roesler, C., Shutler, J. D., Sosik, H. M., Soto, I., Stuart, V., Subramaniam, A., and Uitz, J. (2014). Phytoplankton functional types from space. In Sathyendranath, S. and Stuart, V., editors, *Reports of the International Ocean-Colour Coordinating Group (IOCCG),*, pages 1098–6030. ISSN.

Sathyendranath, S., Watts, L., Devred, E., Platt, T., Caverhill, C., and Maass, H. (2004). Discrimination of diatoms from other phytoplankton using ocean-colour data. *Marine ecology progress series*, 272:59–68.

Sauer, M. J., Roesler, C., Werdell, P., and Barnard, A. (2012). Under the hood of satellite empirical chlorophyll a algorithms: revealing the dependencies of

maximum band ratio algorithms on inherent optical properties. *Optics Express*, 20(19):20920–20933.

Simis, S. G. H., Peters, S. W. M., and Gons, H. J. (2005). Remote sensing of the cyanobacterial pigment phycocyanin in turbid inland water. *Limnology and Oceanography*, 50:237–245.

Stramski, D., Boss, E., Bogucki, D., and Voss, K. (2004). The role of seawater constituents in light backscattering in the ocean. *Progress in Oceanography*, 61(1):27–56.

Swart, S., Chang, N., Fauchereau, N., Joubert, W., Lucas, M., Mtshali, T., Roychoudhury, A., Tagliabue, A., Thomalla, S., Waldron, H., et al. (2012). Southern Ocean Seasonal Cycle Experiment 2012: Seasonal scale climate and carbon cycle links. *South African Journal of Science*, 108(3-4):11–13.

Tan, H., Doerffer, R., Oishi, T., and Tanaka, A. (2013). A new approach to measure the volume scattering function. *Optics Express*, 21:18697–18711.

Tan, H., Oishi, T., Tanaka, A., and Doerffer, R. (2015). Accurate estimation of the backscattering coefficient by light scattering at two backward angles. *Applied optics*, 54(25):7718–7733.

Thomalla, S., Fauchereau, N., Swart, S., and Monteiro, P. (2011). Regional scale characteristics of the seasonal cycle of chlorophyll in the Southern Ocean. *Biogeosciences*, 8(10):2849.

Tuchow, N., Broughton, J., and Kudela, R. (2016). Sensitivity analysis of volume scattering functions. *Optics Express*, 24:18559–18568.

Twardowski, M. S., Boss, E., Macdonald, J. B., Pegau, W. S., Barnard, A. H., and J. R. V. Zaneveld, A. (2001). Model for estimating bulk refractive index from the optical backscattering ratio and the implications for understanding particle composition in case i and case ii waters. *Journal of Geophysical Res*, 106:14129–14142.

Vaillancourt, R. D. (2004). Light backscattering properties of marine phytoplankton: relationships to cell size, chemical composition and taxonomy. *Journal of Plankton Research*, 26:191–212.

Vance, T., Schumacher, J., Stabeno, P., Baier, C., Wyllie-Echeverria, T., Tynan, C., Brodeur, R., Napp, J., Coyle, K., Decker, M., et al. (1998). Aquamarine waters recorded for first time in eastern Bering Sea. *EOS, Transactions American Geophysical Union*, 79(10):121–126.

Volten, A. H., Haan, J. F. D., Hovenier, J. W., Schreurs, R., Vassen, W., Dekker, A. G., Hoogenboom, J., Charlton, F., and Wouts, R. (1998). Laboratory measurements of angular distributions of light scattered by phytoplankton and silt. *Limnology and Oceanography*, 43:1180–1197.

Whitmire, A., Boss, E., Cowles, T., and Pegau, S. W. S. (2007). Spectral variability of the particulate backscattering ratio. *Optics Express*, 15:7019–7031.

Whitmire, A. L., Pegau, W. S., Karp-Boss, L., Boss, E., and Cowles, T. J. (2010). Spectral backscattering properties of marine phytoplankton cultures. *Optics Express*, 18:1680–1690.

Zaneveld, J. R. V. (1995). A theoretical derivation of the dependence of the remotely-sensed reflectance of the ocean on the inherent optical properties. *Journal of Geophysical Research*, 100(C7):13135 – 13142.

Zhou, W., Wang, G., Sun, Z., Cao, W., Xu, Z., Hu, S., and Zhao, J. (2012). Variations in the optical scattering properties of phytoplankton cultures. *Optics Express*, 20:11189–11206.

Appendix A

Processing and Calculations

A.1 EAP model components

A.1.1 EAP size distributions

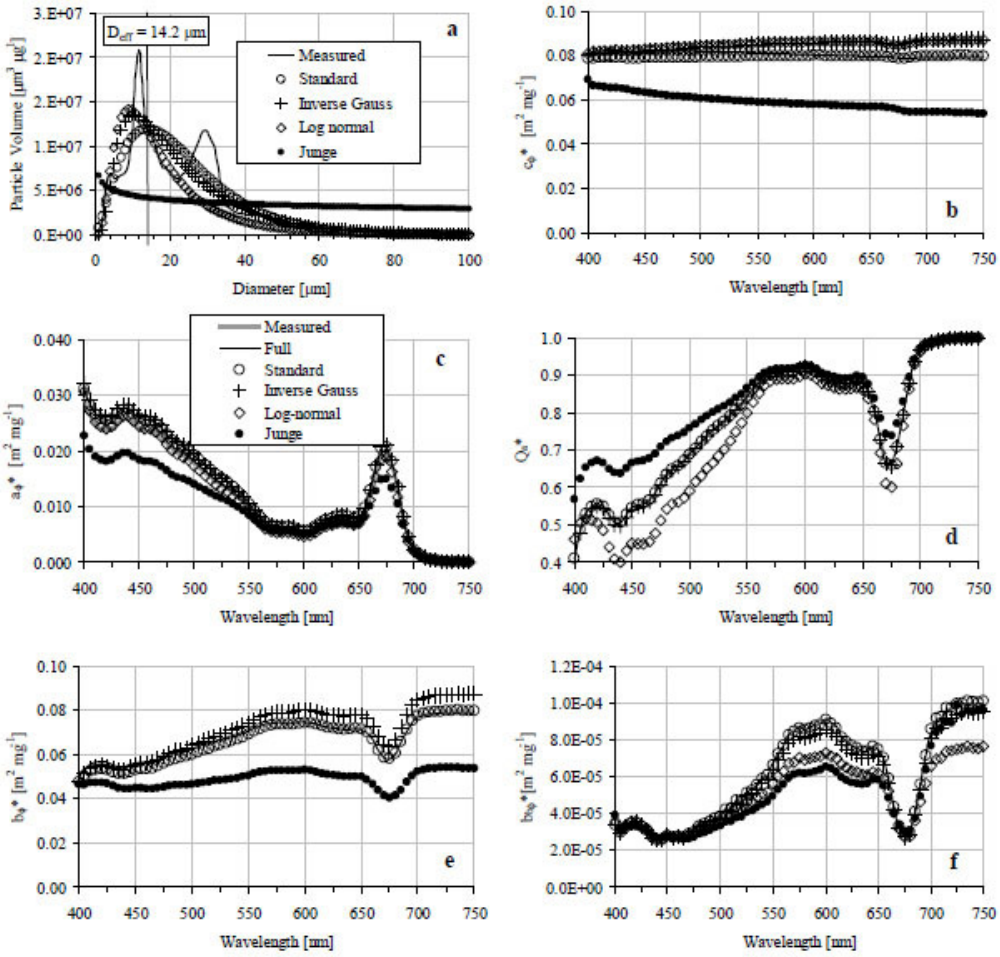

Figure A.1: Measured bimodal eukaryote (dinoflagellate/diatom) size distribution presented with modelled distributions and corresponding EAP IOPs, from Bernard et al. (2007).

A.1.2 EAP Phytoplankton IOPs

Phytoplankton-specific IOPs are presented in Figs. A2 and A3 for generalised diatom/dinoflagellate assemblages and for phycoerythrin-containing assemblages respectively.

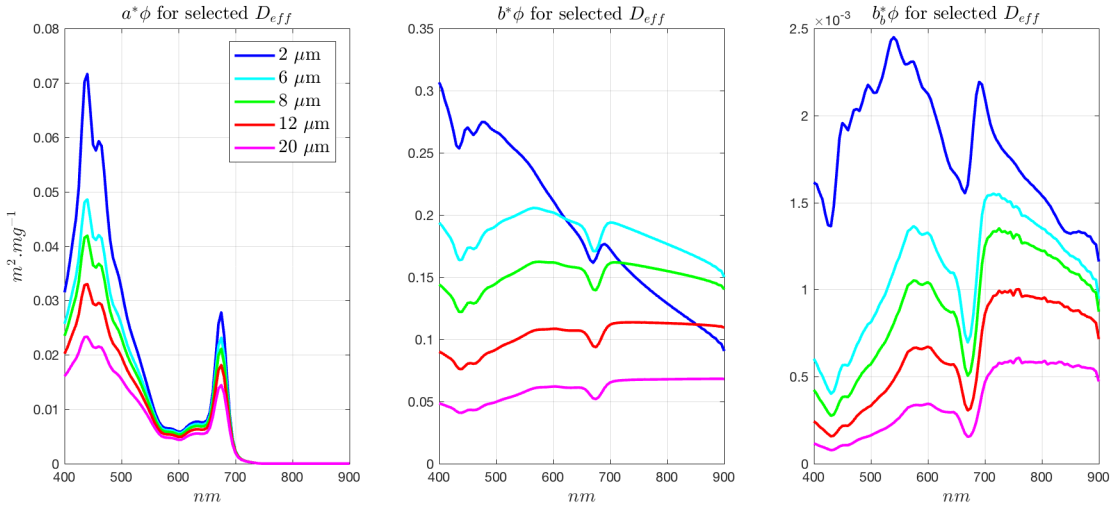

Figure A.2: EAP Eukaryote (dinoflagellate/diatom) IOPs

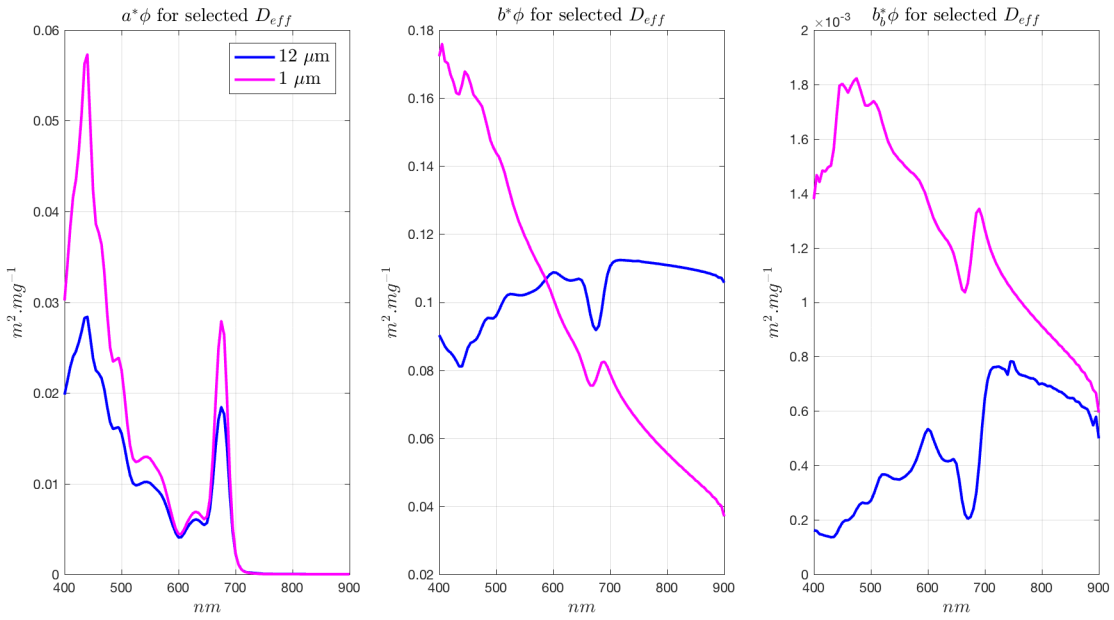

Figure A.3: EAP Phycoerythrin-containing IOPs (based on *Myrionecta Rubra*), used for cryptophyte-dominated assemblages in the Benguela, and *Synechococcus sp.* in the Southern Ocean

A.1.3 EAP $a_{gd}(\lambda)$ parameterisation

A simple exponential combined gelbstoff and detrital absorption term $a_{gd}(\lambda)$ (Bricaud et al., 1981; Roesler et al., 1989) is used as representative of commonly occurring conditions in the Benguela:

$$a_{gd}(\lambda) = a_{gd}(400)\exp[-S(\lambda - 400)] \tag{A.1.1}$$

The exponential slope factor S is given a constant value of 0.012 (Bernard et al., 1998). This value, derived for the Benguela system, is not adjusted for the $a_{gd}(\lambda)$ term used in the Southern Ocean Case Studies. This is acknowledged as a source of uncertainty but supporting literature suggests that values in the range 0.0140 $\pm$ 0.0032 nm^{-1} cater adequately for a variety of water types (Bricaud et al., 1981).

An observed relationship of

$$a_{gd}(400) = 0.0904\log[Chl_a] + 0.1287 \tag{A.1.2}$$

from measurements in the Benguela is used to scale the gelbstof/detrital exponential term, and $a_{gd}(750)$ onwards is assumed to be zero. This parameterisation was derived for high biomass environments. At very low biomass (< 1 $mg.m^{-3}$), the $\log[Chl_a]$ term becomes negative, and so for the Southern Ocean case studies, this parameterisation was amended to

$$a_{gd}(400) = 0.07 * [Chl_a]^{0.75} \tag{A.1.3}$$

following Alvain et al. (2005), noting that the referenced parameterisation is for 440 nm and not 400, but also that the a_{gd} term is used as an approximate measure of total signal sensitivity, and so in this sense an absolutely accurate term is not a requirement.

A.1.4 EAP $b_{bnap}(\lambda)$ parameterisation

Non-algal backscattering is modelled after Roesler and Perry (1995) who describe a small particle backscattering term represented by a power law relationship (their b_{bs},

referred to as b_{bnap} in the EAP model). It has a constant spectral shape dependent only on wavelength, but variable in magnitude.

$$b_{bnap}(\lambda) = \lambda^{-1.2} \tag{A.1.4}$$

This is then adjusted to a selected value of $b_{bnap}(550)$, as detailed in the text.

Keeping the non-phytoplankton backscattering constant with Chl a results in a dependent but non-linear relationship, resulting in an overall $\tilde{b}_b$ that decreases as Chl a increases.

Small particle (non-algal) scatter b_{nap} is approximated as 50 times the b_{bnap} in the Benguela examples and as 100 times the b_{bnap} in the Southern Ocean examples. This yields a non-algal particulate backscattering probability ($\tilde{b}_{bnap}$) of 0.02 (2%) and 0.01 (1%) respectively. This is assumed to be reasonable given that it has been shown that the total particulate backscattering probability $\tilde{b}_b$ varies in the range 1.2 to 3.2 % in coastal waters dominated by non-algal particles (i.e. Case 2) (Chami et al., 2006b), and that generally accepted values for $\tilde{b}_b$ in Case 1 waters is around 1% (Twardowski et al., 2001).

A.2 TSRB processing

In situ radiometric measurements were made using a Tethered Satlantic Radiometer Buoy with two 256 channel spectrographs that are linked to a downward facing 8.5° field of view radiance sensor (measuring L_u at 0.66 m below the sea surface), and an upward looking cosine corrected irradiance sensor, measuring E_d just above the surface. L_u is measured in μW cm^{-2} nm^{-1} sr^{-1}, and E_d in μW cm^{-2} nm^{-1}. Both measurements span 400 to 800 nm at a sampling distance of 3.3 nm to an accuracy of 0.3 nm. They measure continually over a burst of approximately 3 minutes. The raw data is processed using Prosoft 6.3d (Satlantic: Halifax, Canada), and median L_u and E_d measurements are extracted. As the Benguela measurements were made in very high biomass conditions (up to Chl a of more than 300 mg.m^{-3}), it was a challenge to find an appropriate K_{L_u} with which to extrapolate the L_u measurement at 0.66 m to the surface, in order to calculate the resulting R_{rs}, as the tabulated

Mobley K_{L_u} values are not appropriate in massively attentuating waters. Ecolight-S is therefore used to invert the measured L_u and extract a modelled K_{L_u}, which is then used with the measured L_u and E_d data, together with time and location data, to generate surface reflectance R_{rs}. This method gives consistent results and being able to numerically asses the match of the modelled and measured L_u is a good measure of confidence.

The result of using partly measured and partly modelled terms in the final calculation does, however, have the unwanted effect of generating noise in the blue and red regions of the spectrum, where measurement stability is not 100%. The measurements themselves do not appear overly noisy but when multiplied by an exponential K_{L_u} factor, small features in the measurement are magnified.

A.3 Chl *a*

Chl *a* measurements are made using a Turner 10-AU Fluorometer, following Holm-Hansen et al. (1965).

A.4 Model Parameters used for Hydrolight-Ecolight

For most of the experiments, Ecolight's 2-component IOP model was used to generate $R_{rs}(\lambda)$. The "clearest natural water" IOPs were selected for Component 1 (water). IOPs for component 2 (everything else) were precomputed in Matlab from the EAP phytoplankton IOPs and additional $a_{gd}(\lambda)$ and $b_{bnap}(\lambda)$ contributions as required.

For the phase function study (Chapter 3) the 4-component model was selected in order to be able to choose different phase functions for the algal and non-algal components, and compare the differences in terms of the resulting bulk R_{rs}. EAP phase functions were discretised for varying D_{eff} at each wavelength to be able to compute the $R_{rs}\phi$ in Chapter 3 with entirely EAP IOPs including the phase functions. As this is currently only possible as a standard option in Hydrolight for one wavelength at a time, these examples were run at individual wavelengths

and collated afterwards to show the full spectral results. This meant that inelastic scattering, most importantly fluorescence, could not be included in these examples.

In experiments not explicitly pertaining to the choice of phase functions, the best available phase function option was selected, that is, a Fournier Forand phase function chosen for each wavelength, according to the combined backscatter fraction $\tilde{b}_b$.

For Fig. 4. 22 (Uncertainties on measured and modelled R_{rs}), a Fortran routine was developed to enable Hydrolight to select the appropriate discretised EAP phase function automatically for the appropriate D_{eff} and wavelength, and so for the first time fluorescence was included in these examples.

Where a combined Fournier Forand phase function was used in the 2-component model, fluorescence was included (unless otherwise stated for phase function comparison purposes).

Fluorescence quantum efficiency ϕ was approximated by Chl a concentration:

$$< 10 \text{ mg.m}^{-3} = 1\%$$
$$\text{10-50 mg.m}^{-3} = 0.6\%$$
$$\text{50-100 mg.m}^{-3} = 0.2\%$$
$$> 100 \text{ mg.m}^{-3} = 0.1\%$$

These values are based on MODIS ϕ_{sat} climatologies (Behrenfeld et al., 2009), and measurements (Ostrowska et al., 2012) to characterise the reduction in ϕ as eutrophication increases.

A constant set of generalised atmospheric conditions was selected for all experiments. An annual average for solar irradiance and a solar zenith of 30° was used in lieu of time and location.

A.5 Uncertainties

Uncertainties in satellite radiometry were given in Section 4.2.3, and model error in terms of uncertainty/variability in the phase function are described in Chapter 3. There are many additional sources of uncertainty in the model (non-sphericity of phytoplankton, approximations in size distribution, Chlorophyll a density, to name

a few), and they are difficult to quantify. For demonstrative purposes here, given that any retrieval of size properties would be performed with the model itself, the model uncertainty is constrained to just that of the phase function variability, as this has a size implication in itself, as shown in Chapter 3.

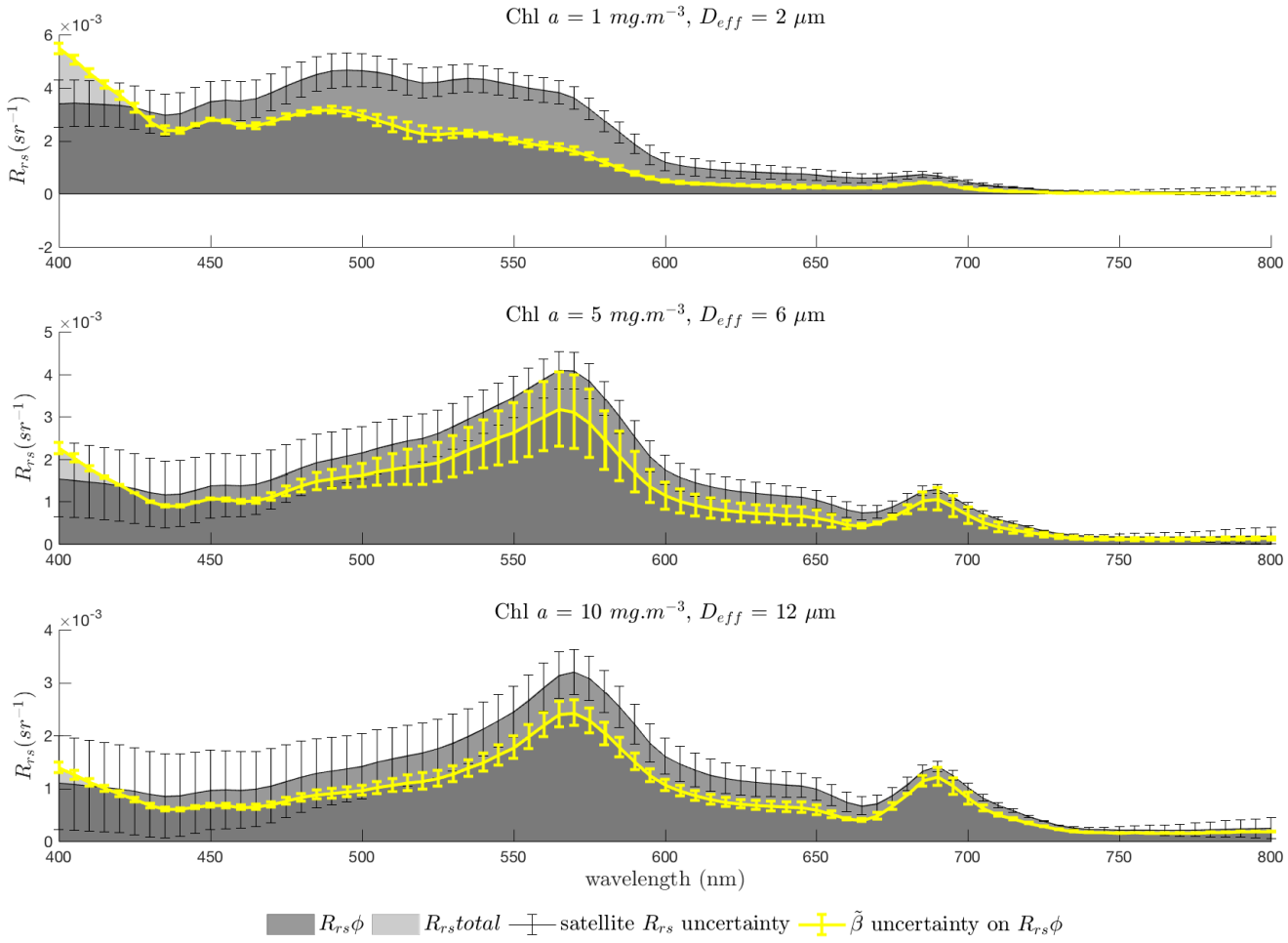

Figure A.4: Total R_{rs} with satellite measurement uncertainties in the blue and red bands from (Mélin et al., 2007) and linearly interpolated between them. An indication of model uncertainty on the $R_{rs}\phi$ is calculated by the spectral differences resulting from the use of a combined $b_{bp}(\lambda)$-specific Fournier Forand phase function independent of wavelength, vs. wavelength- and $b_{b\phi}(\lambda)$-dependent EAP phase functions.

In Fig. 4.22 the model uncertainty is shown for $R_{rs}\phi$ against a background of total R_{rs} with nominal additional $a_{gd}(\lambda)$ and $b_{nap}(\lambda)$, together with the satellite R_{rs} measurement uncertainty. Despite the small model uncertainty on the phytoplanton signal in the blue, the huge impact of additional $a_{gd}(\lambda)$ and the large satellite radiometric uncertainty clearly show the large degree of ambiguity and potential error in the retrieval of the phytoplankton component, even if the $a_{gd}(\lambda)$ is exactly known. Satellite-derived $a_{gd}(\lambda)$ (and CDOM) products have large uncertainties: r^2 of less than 0.25 for 3 different $a_{gd}(\lambda)$ algorithms against *in situ* data (Mélin et al., 2007) - noting that dependence on the atmospheric correction means that a significant level of error is propagated through the algorithms from this source, particularly in the blue.

The most significant spectral regions of Fig. 4.22 in the context of this study are those where the uncertainty on $R_{rs}\phi$ overlap with the bulk measurement uncertainty in each example. These are the spectral regions where the phytoplankton-specific signal dominates the bulk signal to the point that they are arguably indistinguishable, so these regions are particularly promising in terms of PFT detection from the bulk R_{rs}. It is encouraging, too, to note that the regions of maximum δD_{eff} previously identified fall within these regions, meaning that particularly close to 570 nm, the bulk signal not only closely reflects the causal phytoplankton signal, but is also not very sensitive to reasonable variability in $a_{gd}(\lambda)$ and $b_{nap}(\lambda)$. However, it is an important consideration that these are also regions of large uncertainty in the size signal.

At low biomass, the phytoplankton signal falls well outside of the bulk measurement uncertainty, but the question of whether IOPs could be retrieved from the bulk depends on the resulting proportional contribution to the total. With reduced $b_{b\phi}/a\phi$, even small variability in the non-algal contribution to b_b/a results in signal ambiguity.

It can also be observed in Fig. 4.22 that the magnitude of model uncertainty is less, and the proportional contribution of phytoplankton to the bulk IOPs is greater, at wavelengths slightly shorter than those of the maximum δD_{eff} in the case studies. So the spectral location of the largest observable δD_{eff} signal may not

necessarily be the most revealing of PFT discrimination in terms of the associated uncertainties. A sophisticated uncertainty model would be necessary to calculate the respective advantages of reduced contribution uncertainties on a smaller signal, vs. slightly larger uncertainties on a larger workable signal. It is also worth considering that even where the bulk and $R_{rs}\phi$ signals are distinct, there are spectral regions where they are parallel i.e. maintain the same shape. It can be concluded that the phytoplankton contribution determines the spectral shape in these regions. This information could also be exploited to investigate PFT signal from the bulk R_{rs}.

Further work on incorporating EAP phase functions into Hydrolight has enabled the $R_{rs}\phi$ presented here to include the fluorescence term, and this is also a spectral region of large proportional phytoplankton contribution together with small model uncertainty as calculated by the difference in approach to scattering phase functions. This region (around 685 nm) appears in the maximum δR_{rs} plots from the case studies, but has not been discussed as confidence in modelling this spectral region accurately needs to be improved with respect to natural variability in fluorescence quantum yield and phytoplankton response to the light environment. But it is known that this region holds further useful information on phytoplankton health (Greene et al., 1992) as well as size.

Overall, the uncertainties in both measured and modelled quantities should be considered in terms of the proportional contribution by phytoplankton. The highest proportional phytoplankton contribution to the bulk optics, and therefore most promising signal for PFTs, occurs where elevated scatter due to biomass is complemented by the elevated scatter of small phytoplankton cells. Approaches to modelling the phase functions result in an inherent ambiguity of about 4 μm at very high biomass, but this drops with biomass and as D_{eff} increases.